Rare-earth based Chemoresistive CO_2 Sensors

Dissertation

der Mathematisch-Naturwissenschaftlichen Fakultät
der Eberhard Karls Universität Tübingen
zur Erlangung des Grades eines
Doktors der Naturwissenschaften
(Dr. rer. nat.)

vorgelegt von
Takuya Suzuki
aus Kanagawa / Japan

Tübingen
2020

Gedruckt mit Genehmigung der Mathematisch-Naturwissenschaftlichen Fakultät der Eberhard Karls Universität Tübingen.

Tag der mündlichen Qualifikation:	28.02.2020
Dekan:	Prof. Dr. Wolfgang Rosenstiel
1. Berichterstatter:	Prof. Dr. Udo Weimar
2. Berichterstatter:	Prof. Dr. Dieter Kölle

Abstract

CO_2 sensing is of paramount importance for monitoring the state of the atmosphere, controlling indoor air quality, and cultivating crops in greenhouses or plant factories. Obtaining low cost, simple and good performance chemoresistive CO_2 gas sensors has the potential to be a game changer. Rare-earth oxycarbonates $Ln_2O_2CO_3$ have been proposed as promising chemoresistive materials for CO_2 sensors. The already published results indicate monoclinic $La_2O_2CO_3$ as the most suitable material. On the other hand, there are no reports about the sensing properties of more stable hexagonal $La_2O_2CO_3$ and the other rare-earth oxycarbonates than La and Nd.

In my master study, I have succeeded for the first time in synthesizing monoclinic $La_2O_2CO_3$ and hexagonal $La_2O_2CO_3$ separately by heat treatment of La oxalate hydrate and showing that hexagonal $La_2O_2CO_3$ possesses better properties as a CO_2 sensing material. Here, the heat treatment conditions have been optimized for stabilizing the synthesis and sensing properties of $La_2O_2CO_3$.

In order to obtain the other rare-earth oxycarbonates, heat treatments of the rare-earth organic acid salts hydrate were implemented. Rare-earth oxycarbonates $Ln_2O_2CO_3$ (Ln = La, Nd, and Sm) and rare-earth oxides Ln_2O_3 (Ln = Nd, Sm, Gd, Dy, Er, and Yb) and LnO_2 (Ln = Ce) have been studied. All the materials, except for CeO_2 and Nd_2O_3, were sensitive to CO_2. This is a remarkable new finding that rare-earth oxides Ln_2O_3 (Ln = Sm, Gd, Dy, Er, and Yb), that crystalize in cubic structures, also exhibited a chemoresistive effect for CO_2. All the CO_2 sensitive materials, except for $Nd_2O_2CO_3$, showed sufficient performance for practical use in terms of the stability, influence of humidity, selectivity, and the linearity of sensor signal up to 10,000 ppm. Hexagonal $La_2O_2CO_3$ was the best among them.

For basic understanding of the sensing mechanism, operando characterization including AC impedance spectroscopy, work function, X-ray Diffraction (XRD), and diffuse reflectance infrared Fourier transform spectroscopy (DRIFTS) has been conducted mainly on the best performing hexagonal $La_2O_2CO_3$ based sensor. From the results, it seems reasonable to conclude that the competitive adsorption between carbonates and hydroxyl groups on the surface of rare-earth based CO_2 sensitive material is responsible for the sensor effect.

Contents

Abbreviations

AC	alternating current
CAGR	compound annual growth rate
CPD	contact potential difference
CPE	constant phase element
DC	direct current
DRIFTS	diffuse reflectance infrared Fourier transform spectroscopy
NDIR	non-dispersive infrared
r.h.	relative humidity
SEM	scanning electron microscope
XRD	X-ray diffraction

1 Introduction

1.1 Background

1.1.1 Social demands

Demands for CO_2 sensing are increasing in a wide range of fields recently. The most important applications are for monitoring the state of the atmosphere, controlling indoor air quality, and cultivating crops in greenhouses or plant factories.

The monthly average concentration of atmospheric CO_2 gas in January at Mauna Loa observatory has increased from 316 ppm in 1960 to 411 ppm in 2019 [1]. It is thought that the increase of CO_2 can cause the global warming since CO_2 has a greenhouse effect [2][3]. To control the indoor air quality, the value of 1000 ppm is widely accepted as an upper CO_2 concentration limit for an adequate ventilation for our health [4][5]. On the other hand, CO_2 enrichment has been commonly used to increase yields of cultivated crops in greenhouses [6][7], and it was reported that a CO_2 concentration between 1000 ppm and 3000 ppm increases the yield of crops while a CO_2 concentration more than 3000 ppm decreases the yield [8].

According to [9], over the next five years the CO_2 sensors market will register a 9.5% CAGR (Compound Annual Growth Rate) in terms of revenue, the global market size will reach US$ 910 million by 2024, from US$ 580 million in 2019.

1.1.2 Current technology

Two types of sensors are commercially available; solid state electrolyte and non-dispersive infrared (NDIR). The solid state electrolyte sensors [10][11], which are

basically composed of two different kinds of ionic conductors and heated at around 500°C, indicate the output voltage depending on the CO_2 gas concentration. In the case of NDIR sensors [12][13], the main components are an infrared source, a sample cell (or light tube), wavelength filters, and a detector. The concentration of CO_2 gas is measured electro-optically by its absorption of a specific wavelength in the infrared range. The standard current technology for practical use is mainly based on NDIR sensors, which are expensive, bulky, hard to install, and high maintenance.

1.1.3 Chemoresistive material

Obtaining low cost, simple and good performance chemoresistive CO_2 gas sensors has the potential to be a game changer. The term “chemoresistive” stands for a property that electrical resistance changes with chemical environments such as a gas concentration. Chemoresistive sensors are basically composed of only a chemoresistive material, electrodes and a heater, therefore, they can be simple and compact.

Several types of chemoresistive CO_2 gas sensors have been proposed (Table 1.1). Among them, rare-earth oxycarbonates $Ln_2O_2CO_3$ (Ln = La and Nd) indicate the highest sensor signal at a relatively low operating temperature. A lower operating temperature is favorable because it leads to a lower power consumption of the sensor.

The already published results [14][15][16][17][18] indicate monoclinic $La_2O_2CO_3$ as the most suitable material for CO_2 sensors among this family of materials. However, the monoclinic structure is metastable and could be transformed into the hexagonal structure. On the other hand, there are no reports about the sensing properties of more stable hexagonal $La_2O_2CO_3$ and the other rare-earth oxycarbonates than La and Nd. In my master thesis [19], I have succeeded for the first time in synthesizing monoclinic

$La_2O_2CO_3$ and hexagonal $La_2O_2CO_3$ separately by heat treatment of La oxalate hydrate and showing that La oxalate hydrate is a better precursor for reproducibly synthesizing $La_2O_2CO_3$ compared to La hydroxide which has been used in many of previous works, and hexagonal $La_2O_2CO_3$ possesses better properties as a CO_2 sensing material in terms of the sensitivity and thermal stability than the monoclinic one. However, the optimization of the heat treatment was not completed yet.

Table 1.1 Operating temperature and sensor signal of chemoresistive CO_2 gas sensors from the literature.

Material	Operating temperature	Sensor signal* at 1000ppm	Reference
SnO_2–La_2O_3	400 °C	1.4	[20]
SnO_2–LaOCl	425 °C	1.3	[21]
$BaTiO_3$–CuO-$LaCl_3$	550 °C	2.0	[22]
LaOCl	260 °C	3.0	[23]
$Ln_2O_2CO_3$ (Ln=La,Nd)	250~400 °C	7.0~15.0	[14][15]

* Sensor signal is defined as R_g / R_{air} where R_g and R_{air} are the sensor resistance in air with gas and the sensor resistance in air without gas respectively.

1.2 Scope of the work

From the background above, the scope of this work is as follows.

1) Stabilizing the synthesis and sensing properties of $La_2O_2CO_3$

2) Material exploration for rare-earth based chemoresistive CO_2 sensors

3) Basic understanding of the sensing mechanism

Regarding 1), I have reviewed my preliminary study [19][24][25] about the synthesis of $La_2O_2CO_3$ and optimized the heat treatment conditions for stabilizing the synthesis and sensing properties of $La_2O_2CO_3$.

Regarding 2), I have made a material exploration for rare-earth based chemoresistive CO_2 sensors by trying to synthesize other rare-earth oxycarbonates than La and Nd using the synthesis method studied in 1), and evaluating the sensors based on the materials in terms of practical use.

Regarding 3), I have conducted operando-investigations, such as, AC (alternating current) impedance spectroscopy, work function, XRD, and diffuse reflectance infrared Fourier transform spectroscopy (DRIFTS) mainly on the best performing sensor for basic understanding of the sensing mechanism.

2 Experimental tools and setups

2.1 Sample preparation

2.1.1 Material synthesis

Starting materials were rare-earth oxalate hydrates or acetate hydrates, which are all commercially available powders [19]. Heat treatments were performed as shown in Figure 2.1. Each powder was put in an alumina boat and heated at 450~550°C for 2~72 hours using a furnace, Nabertherm GmbH R50/250/13. Ambient air, approximately 50% r.h. (relative humidity) @20°C with 400 ppm CO_2, was always sent into the furnace by a pump.

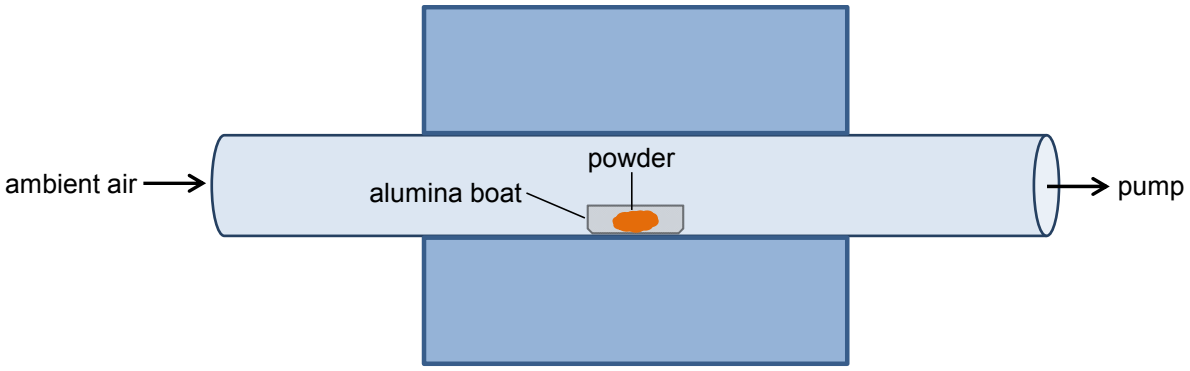

Figure 2.1 Schematic of heat treatment setup [19].

2.1.2 Sensor fabrication

The powders after the heat treatment were mixed with propane-1,2-diol using a vibrating mill (30 Hz) for 30 minutes. The resulting pastes were screen printed onto alumina substrates provided with Pt interdigitated electrodes and Pt heaters as shown in

Figure 2.2. After the deposition of the sensing layer, the substrates were dried in air at 80°C for more than 12 hours using an oven and then heated for 10 minutes using the same furnace and the conditions as for the initial heat treatment of the powders.

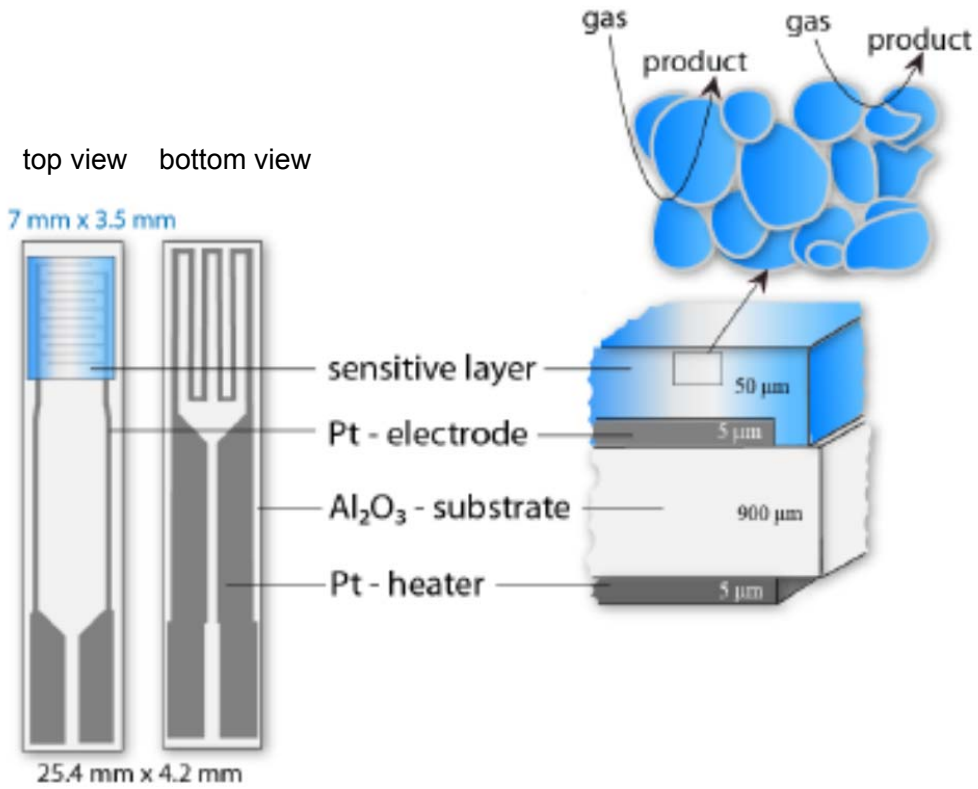

Figure 2.2 Schematic of the sensor substrate [19].

2.1.3 Characterization

XRD, PANalytical X'Pert Pro MRD, was applied to characterize the crystal structure of the powders after the heat treatment and sensors after the DC resistance measurements. The samples were scanned from 10° to 60° (2θ) by the X-ray with

1.5405980 Å wavelengths (Cu-$K\alpha_1$ radiation). Data was evaluated by the PANalytical Highscore software.

A SEM, JOEL JSM-6500F, was utilized to observe the morphology of the sensors. The surface of samples was coated with Au thin film to prevent the occurrence of charge-up. The thickness of the Au coating was about 10 nm. The accelerating voltage of the SEM was 20 kV.

2.2 Sensor evaluation

2.2.1 DC resistance measurement

Figure 2.3 shows a schematic of the DC resistance measurement setup [19]. A constant DC voltage was applyed to the heater backside by a power supply, Hewlett Packard E3611A and Manson NSP-3630, so as to maintain the sensor temperature at 250°C, 300°C, or 350°C. According to the previous works [14][15][26][27], the sensor signal to CO_2 is maximum between 250°C and 350°C. Below 250°C, the sensor resistance is too high to be accurately measured. Above 350°C, the sensing material is not stable. Therefore, those three Operating temperature conditions are enough to compare the properties of different materials.

The heater voltage was calibrated in advance with a contactless thermometer. Figure.2.4 shows the schematic of the heater calibration measurement setup and the obtained calibration curve as an example. The surface temperature was measured using an infrared (IR) contactless thermometer and by varying the applied voltage of the heater. A linear correlation between the applied voltage and the temperature was obtained.

The DC resistance of sensor was measured every 10 seconds using an electrometer, Agilent 34970A, with varying humidity and CO_2 concentration as shown in Figure 2.5 by a flow controller and a H_2O bubbler. The test program described in Figure.2.5 is a standard procedure used in the industry. The sensors were driven in humid air (50% r.h. at 20°C) with 300ppm CO_2 for 12 hours to stabilize the properties before starting the measurements of sensor responses. Figure.2.6 shows an example of the time variation of the sensor resistance indicating that the sensor resistance was stable within 1 hour after the change of CO_2 concentration. The time period of 10 seconds is good enough to follow the time variation of the sensor resistance. Resistance for each condition was obtained by averaging the last 10 points.

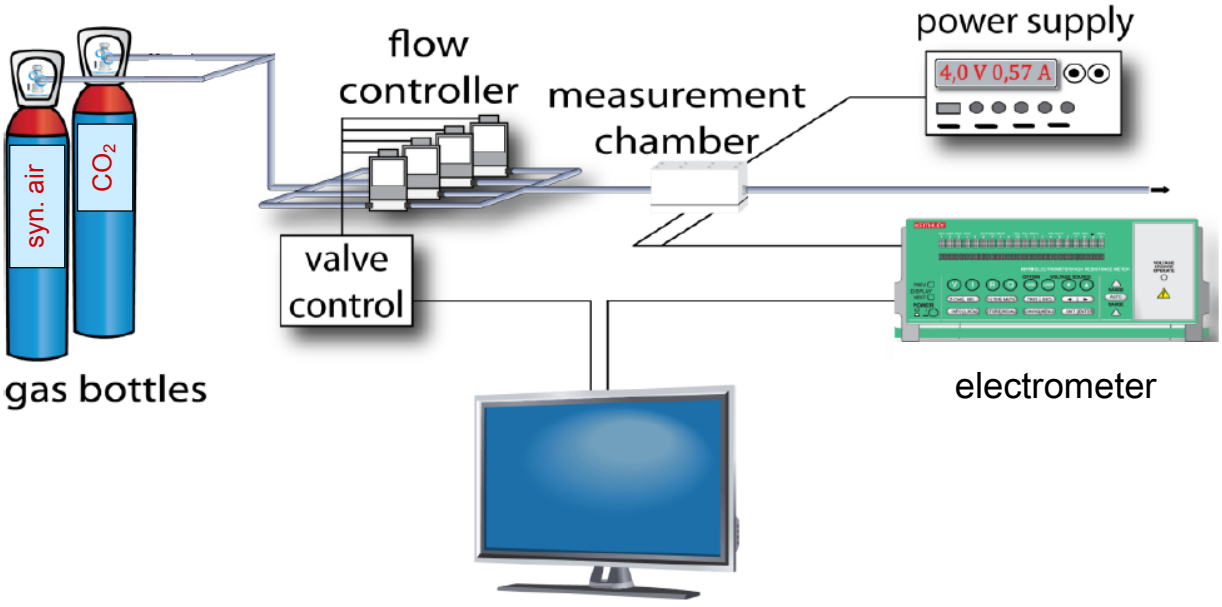

Figure 2.3 Schematic of DC resistance measurement setup [19].

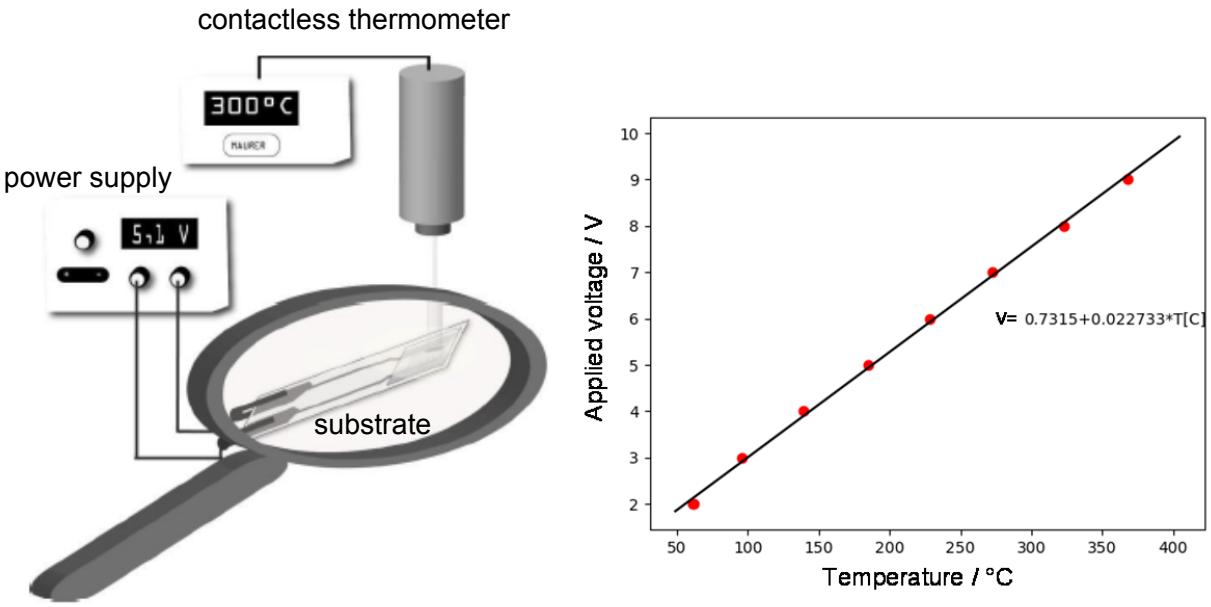

(a) Measurement setup (b) Obtained calibration curve as an example

Figure 2.4 Schematic of the heater calibration [19].

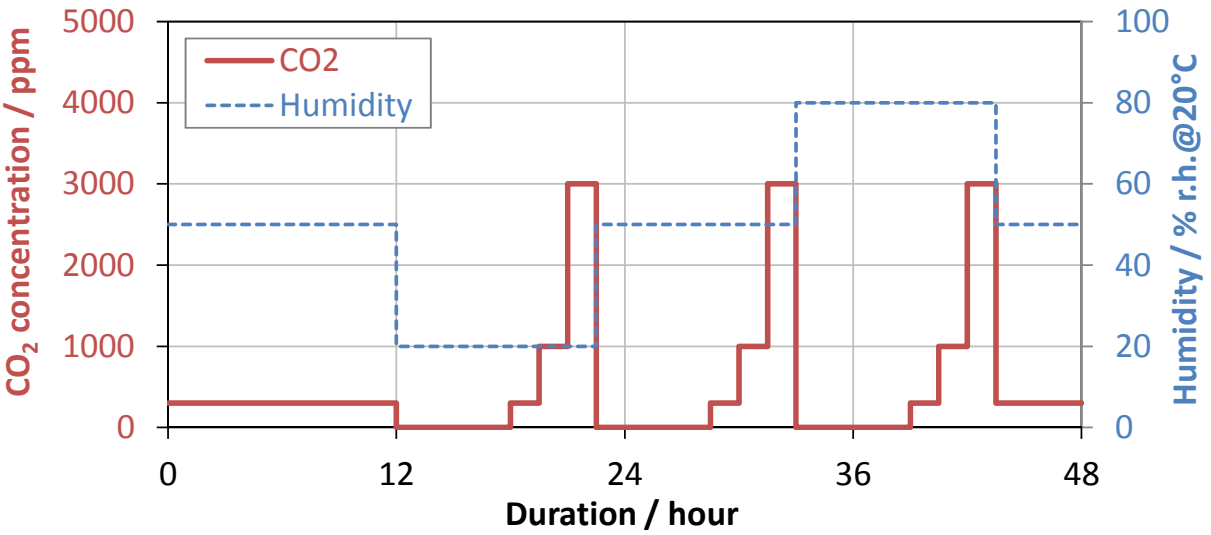

Figure 2.5 Time variation of humidity and CO_2 concentration during DC resistance measurements for one operating temperature [19].

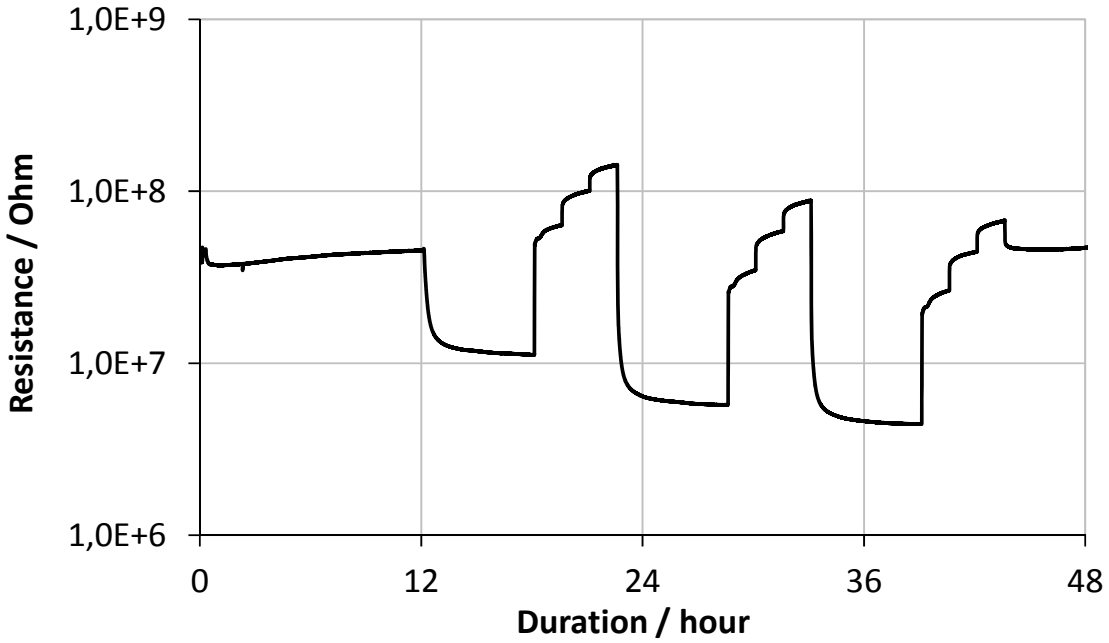

Figure 2.6 Time variation of sensor resistance (as a typical example) [19].

2.2.2 Sensor signal to CO_2

The sensor signal was defined as (2.1)

$$\text{Senor signal} = R_{gas} / R_0 \qquad (2.1)$$

where R_{gas} and R_0 were the sensor DC resistance at a certain concentration of a target gas in air and at 0 ppm of the gas in air, respectively, which were measure in the manner described in the preceding section.

2.2.3 Selectivity and Sensitivity up to 10,000 ppm CO_2

Selectivity and sensitivity up to 10,000 ppm CO_2 of the CO_2 sensitive materials were evaluated in humid air at an optimal operating temperature using the apparatus shown

in Figure 2.3. To evaluate the selectivity, sensor signals to ethanol, CO, and H_2 up to 200ppm were measured in humid air at the optimal operating temperature. In the targeted applications, it is thought that CO_2 concentration is ranging from 400 ppm to 10,000 ppm, and 200 ppm of ethanol, CO, and H_2 are more than the maximum values. Figure.2.7 shows the time variation of gas flow during the measurement.

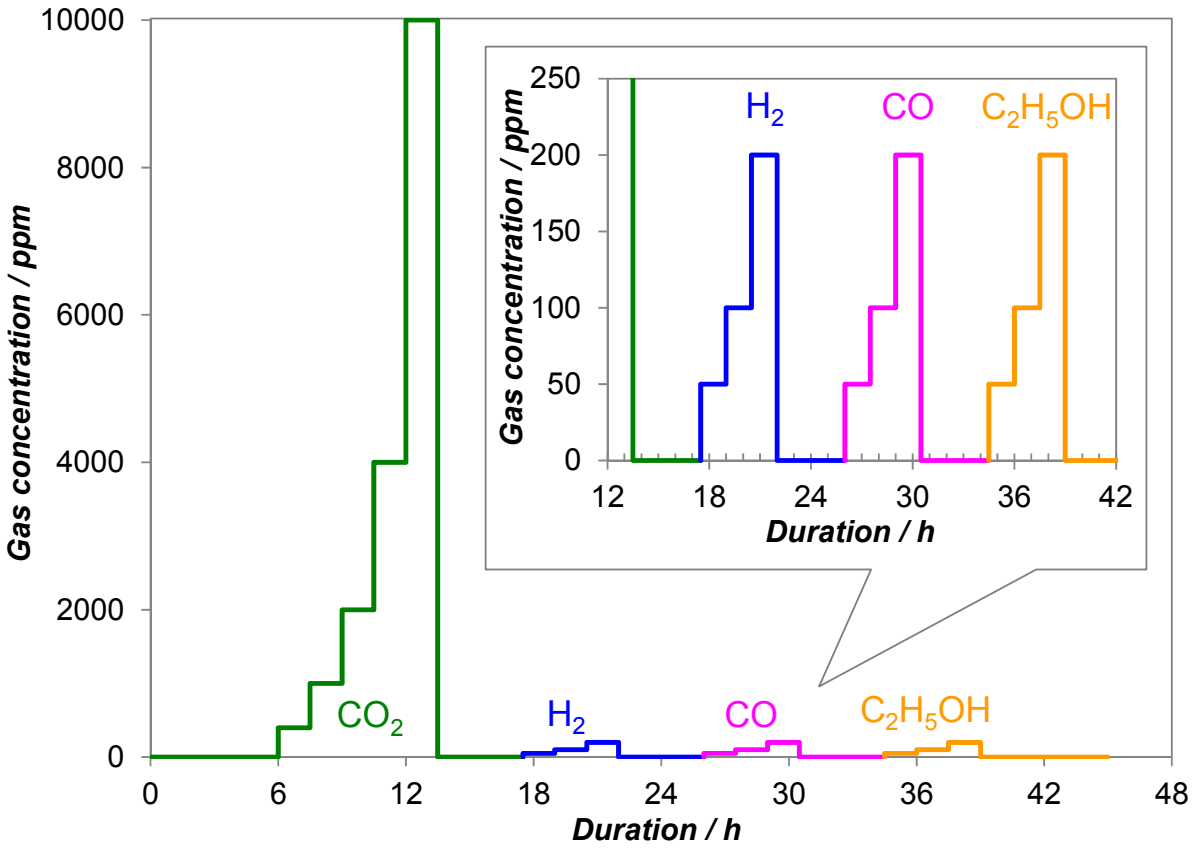

Figure 2.7 Time variation of gas flow during the sensitivity and selectivity evaluation.

2.2.4 Stability

In order to test the stability of the CO_2 sensitive materials, a standard three day long ageing process was performed in a high humidity and high CO_2 concentration in air (80

% r.h. @20°C and 3000ppm CO_2) at an operating temperature of 350°C using the apparatus shown in Figure 2.3 [19]. The standard sensor signal measurements were performed before and after the ageing process.

2.3 Operando characterization

For basic understanding of the chemoresistive effect for CO_2, “Operando characterization” including XRD, AC impedance spectroscopy, Work function measurement, and DRIFTS has been performed (Figure 2.8) [28][29]. The operando stands for actual gas sensing conditions, for example, at an operating temperature of 300 °C, with or without gas exposure, in humid or dry air.

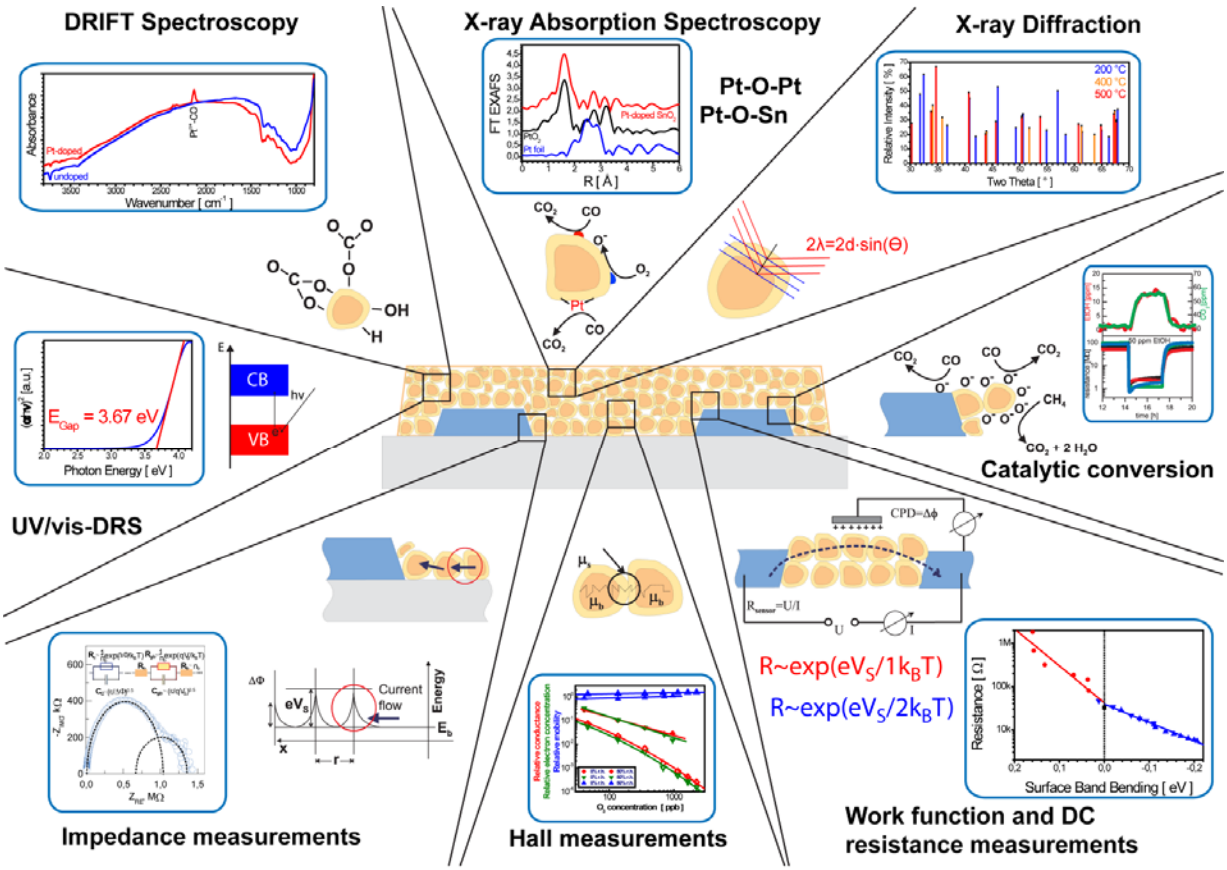

Figure 2.8 Overview of operando characterization.

2.3.1 Operando XRD

XRD and DC resistance under the operating conditions are measured simultaneously using the operando XRD apparatus, Bruker AXS GmbH D8 Discover 2D-Microdiffractometer, as shown in Figure 2.9. The X-ray beam with 1.790300 Å wavelengths (Co-Kα radiation) focused to less than 1 mm in diameter was irradiating the sensing layer through the X-ray optics and the transparent window of the sensor chamber. Then the diffracted beam reached the X-ray detector, which measured the X-ray intensity from the angle (2θ) between 20° and 60° at once. The sensor electrodes and the heater electrodes were electrically connected to an electrometer and a power supply through the sensor holder, which was put in the sensor chamber connected to a gas flow controller as in Figure 2.3.

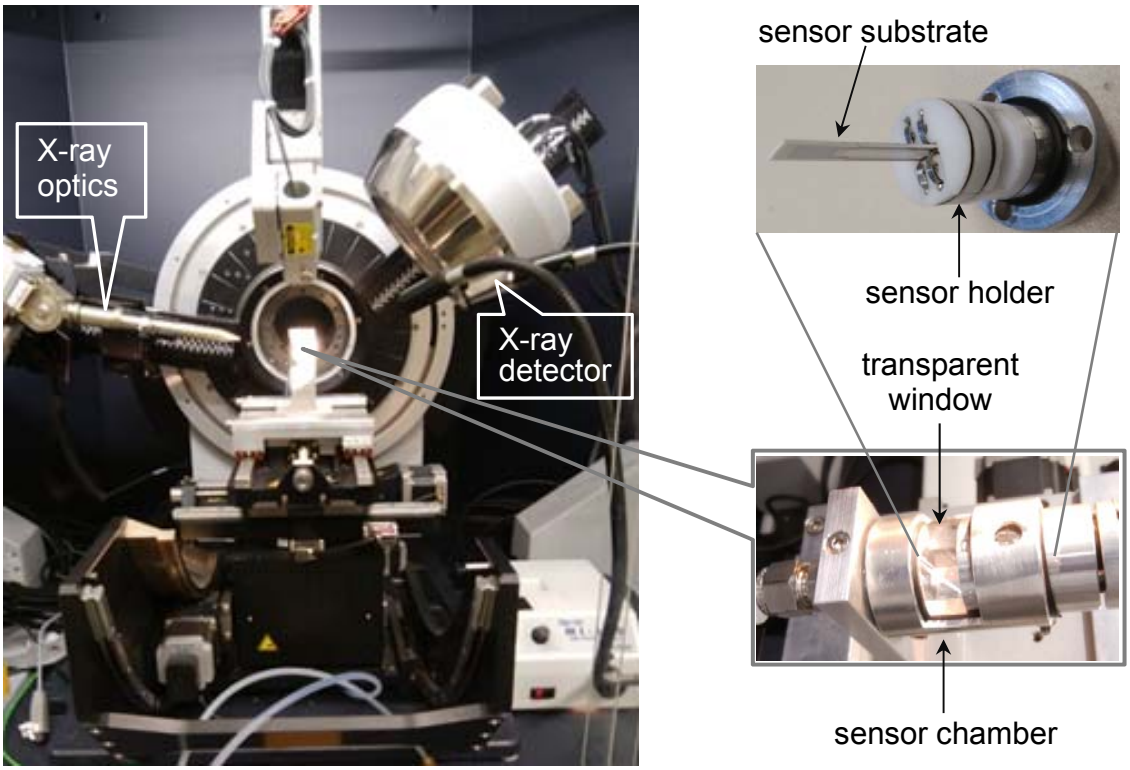

Figure 2.9 Picture of the operando XRD setup.

2.3.2 Operando AC impedance spectroscopy

To reveal the conduction mechanism of the sensor, operando AC impedance spectroscopy was used. From the AC impedance spectroscopy data, one can identify the different contributions to the conduction process through the sensing layer such as: the nature of the charge carriers (ionic or electronic); the presence of space charge regions associated to surface depletion / enrichment or material – electrode contacts; the dominant contributors to the conduction.

Figure 2.10 illustrates a general conduction model and the equivalent circuit for a semi-conductive polycrystalline material. Grain-grain boundaries or grain-electrode boundaries can form Schottky barriers and space charge regions, therefore, the total impedance is composed of grain bulk resistors (R_b), parallel combinations of resistor and capacitor at grain-grain boundaries (R_{gb} ▪ C_{gb}) and grain-electrode boundaries (R_c ▪ C_c). When an AC voltage is applied to the equivalent circuit with varying frequency ω, the impedances *Z* is represented in (2.2),

$$Z = R_b + \frac{R_{gb}}{1+j\omega R_{gb}C_{gb}} + \frac{R_c}{1+j\omega R_c C_c} \qquad (2.2)$$

and can be plotted in a complex plane as shown in Figure 2.11. In this Cole-Cole plot, the straight line corresponds to a resistor and the half-circle corresponds to a parallel combination of resistor and capacitor.

According to [29][30], R_{gb} ▪ C_{gb} and R_c ▪ C_c are related to the band bending V_s at the grain boundary and the difference between the Fermi levels of the electrode and of the sensing layer material $\Delta\Phi$ as described in (2.3) and (2.4),

$$R_{gb} \propto \exp(eV_s/kT), \quad C_{gb} \propto (\varepsilon/eV_s)^{0.5} \qquad (2.3)$$

$$R_c \propto \exp(\Delta\Phi / kT), \quad C_c \propto (\varepsilon/\Delta\Phi)^{0.5} \qquad (2.4)$$

where e is elementary electric charge, k is Boltzmann constant, T is absolute temperature, ε is dielectric constant.

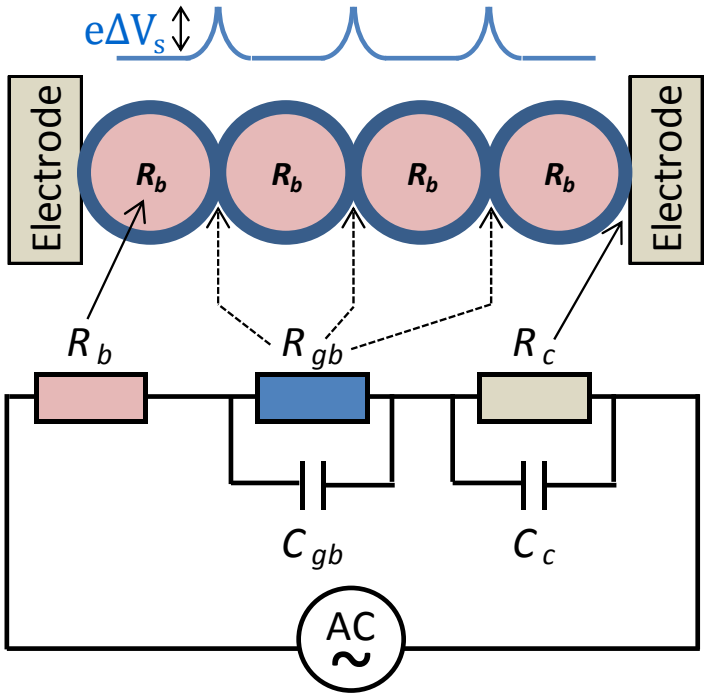

Figure 2.10 General conduction model and the equivalent circuit for semi-conductive polycrystalline material.

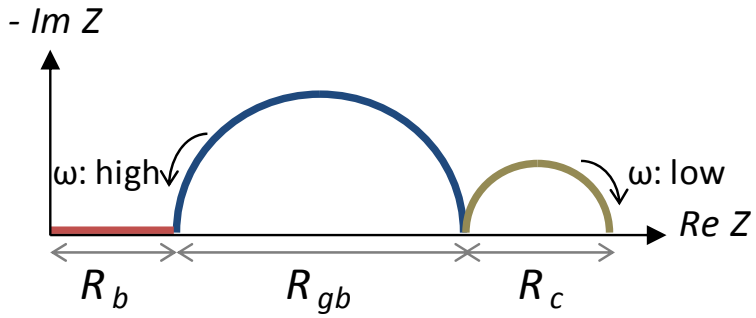

Figure 2.11 Cole-Cole plot in a complex plane.

In real cases, in order to take into account the non-ideality of the various components, the equivalent circuit and the formula of impedance *Z* should be modified as Figure 2.12 and (2.5).

$$Z = R_b + \frac{R_{gb}}{1+(j\omega)^p R_{gb} C_{gb}} + \frac{R_c}{1+(j\omega)^p R_c C_c} \qquad (2.5)$$

In formula (2.5), the two capacitors are replaced by CPE (Constant Phase Element) where jω in *Z* is replaced by (jω) to the power of p, and a capacitor from the substrate is added. The p value is a factor corresponding to how depressed the half-circle is. If p=1, the equation is identical to that of a capacitor, and the shape is perfect half circle. If p<1, the circle is depressed because of the non-homogeneity in the system.

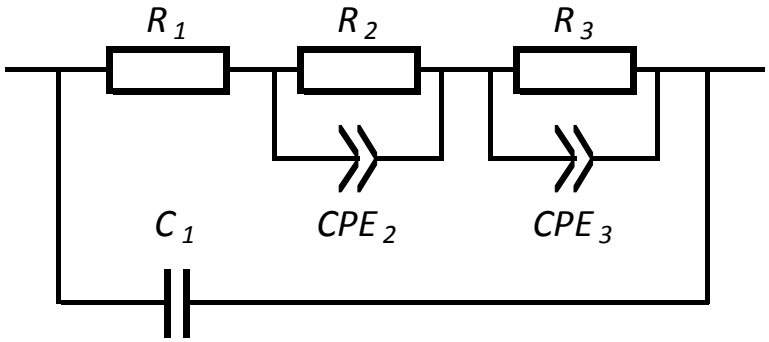

Figure 2.12 Modified equivalent circuit for semi-conductive polycrystalline material.

AC impedance under operating conditions was measured using the setup shown in Figure 2.13. The measuring system was basically the same as the DC resistance measurement in Figure 2.3 except for the electrochemical impedance spectroscopy analyzer, AMETEK Scientific Instruments PARSTAT4000, instead of normal electrometer. Experimental results were fitted by Scribner Associates, Inc. ZView

software using the equivalent circuit shown in Figure 2.12, which leads to the conduction model.

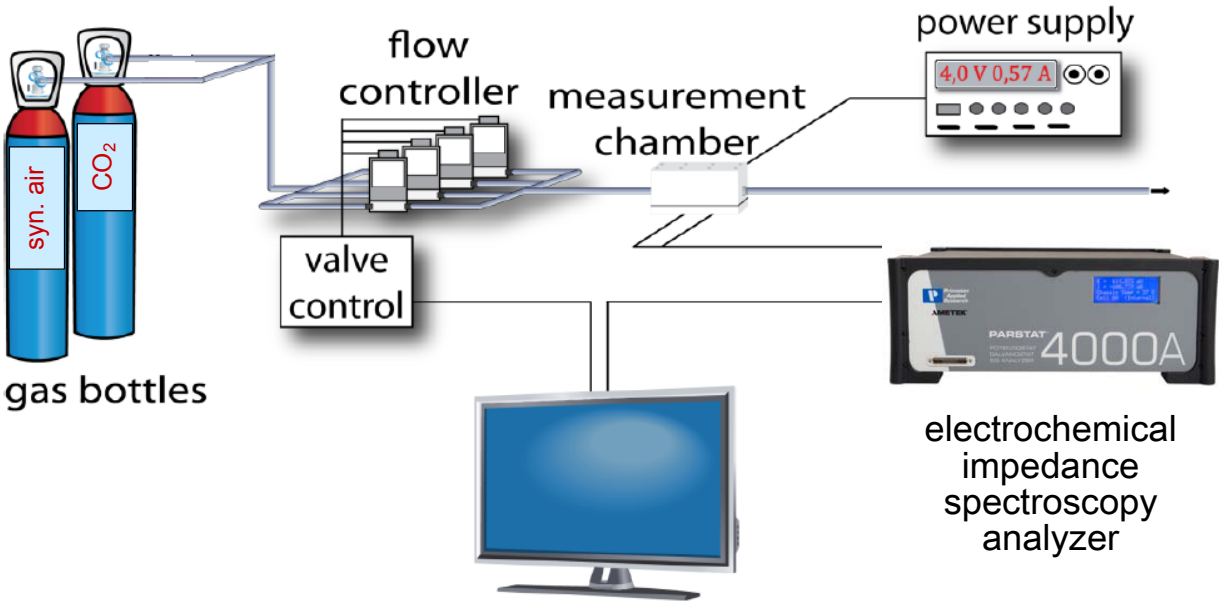

Figure 2.13 Schematic of operando AC impedance spectroscopy setup.

2.3.3 Operando Work function measurement

Contact Potential Difference, CPD and DC resistance under operating conditions were measured simultaneously using the Kelvin probe method as shown in Figure 2.14. There is a relation between CPD, work function change $\Delta\Phi$, and electric charge e represented as (2.6) [31].

$$\Delta CPD = \frac{\Delta\Phi}{-e} \qquad (2.6)$$

Work function change $\Delta\Phi$ is composed of band bending change $e\Delta Vs$ and electron affinity change $\Delta\chi$ as shown in (2.7).

$$\Delta\Phi = e\Delta V_s + \Delta\chi \qquad (2.7)$$

The band bending change $e\Delta Vs$ is related to the changes in the surface charge that are the reason of the appearance of space charge layers mentioned in the previous section, while electron the affinity change $\Delta\chi$ is related to the changes in the concentration of the dipoles (that carry 0 charge), both because of reactions between gases and the surface of the sensing material.

For the case in which the conduction process is controlled by back to back Schottky barriers, combining resistance and work function changes measurements, it is possible to determine the changes of electronic affinity. This is because the resistance change R_{air}/R_{gas} owing to the band bending is linked to the changes in band bending, see (2.3) as (2.8),

$$\frac{R_{air}}{R_{gas}} = exp\left(-\frac{e\Delta V_s}{kT}\right) \qquad (2.8)$$

Accordingly, the band bending $e\Delta Vs$ is derived from (2.8) as (2.9)

$$e\Delta V_s = kT\ ln\frac{R_{gas}}{R_{air}} \qquad (2.9)$$

Electron affinity change $\Delta\chi$ can be derived from (2.6) and (2.7) as (2.10).

$$\Delta\chi = \Delta\Phi - e\Delta V_s = -e\Delta CPD - e\Delta V_s \qquad (2.10)$$

With the help of (2.9) and (2.10), band bending $e\Delta Vs$ and electron affinity change $\Delta\chi$ can be obtained from the experimental results for CPD and DC resistance.

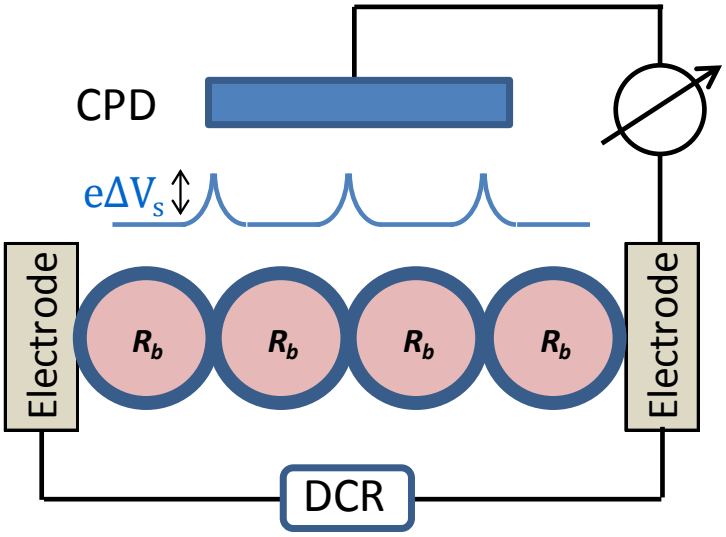

Figure 2.14 Schematic of operando Work function measurement principle.

2.3.4 Operando DRIFTS

To understand how the gases such as CO_2 and H_2O produce chemical reactions and form surface adsorbates, which can be responsible for both the change of surface charge and of the concentration of dipoles, DRITFS (Diffuse Reflectance Infrared Fourier Transform spectroscopy) and DC resistance were simultaneously measured using the setup shown in Figure 2.15.

For the DRIFTS measurements, an evacuated FT-IR spectrometer (Bruker Vertex 80v) which was equipped with a Harrick cell ("Praying Mantis") was used. A sensor was put in a special chamber mounted in the cell. The spectrometer consists of an interferometer, KBr window (beam splitter) and the infrared light was recorded with a LN-MCT-Narrow detector (Liquid Nitrogen cooled - Mercury cadmium telluride), a photo detector. The spectrum was measured every 15 minutes continuously with a resolution of 4 cm^{-1} and 1024 sample scans. The absorbance spectrum was derived from (2.11).

$$Absorbance = -\log\left(\frac{SC_{\,test\,gas}}{SC_{\,reference}}\right) \qquad (2.11)$$

where SC was obtained single channel spectrum.

For the DC resistance, the measuring system was basically the same as the DC resistance measurement in Figure 2.3.

2.3.5 Short summary of operando characterization

Operando XRD can show the correlation between resistance change and bulk crystal structure. Operando AC impedance spectroscopy allows us to identify the conduction mechanism regarding the current carrier and the contributions such as grain bulk, grain-electrode boundaries, or grain-grain boundaries which can form band bending and space charge regions. If the dominant current carrier is electronic and it is mainly controlled by the band bending at grain-grain boundaries depending on the atmosphere, one can derive the band bending $e\Delta Vs$ and electron affinity change $\Delta\chi$ separately from operando Work function measurement. Operando DRIFTS clarifies the surface adsorbate species associated with electron affinity change $\Delta\chi$. This operando characterization can reveal the sensing mechanism.

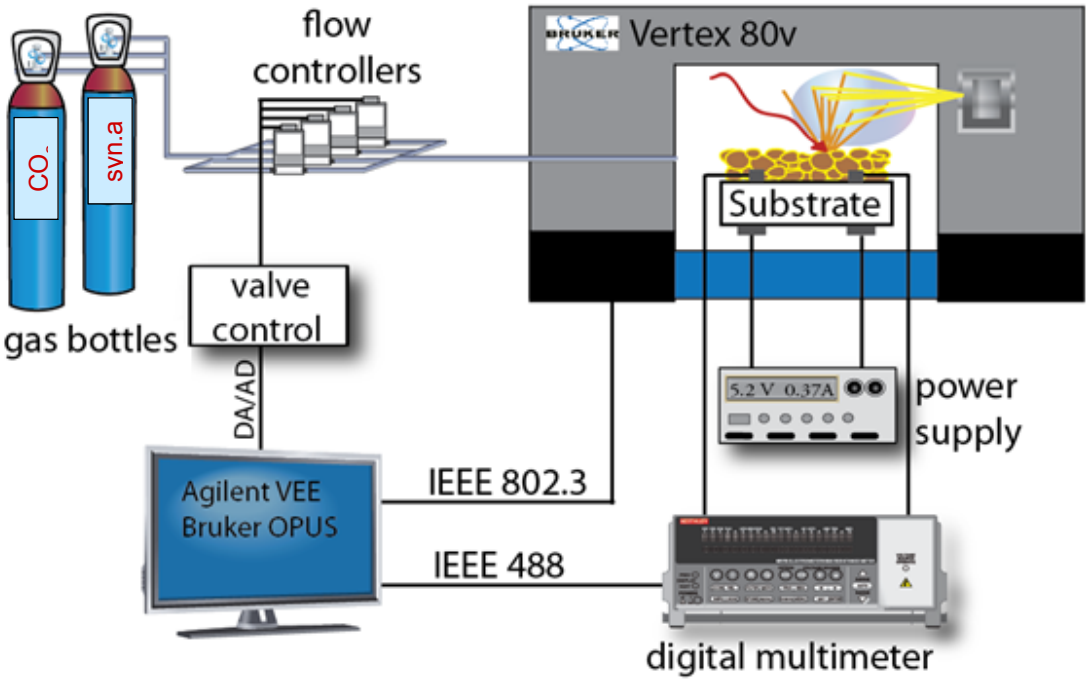

Figure 2.15 Schematic of operando DRIFTS setup.

3 Stabilizing the synthesis and sensing properties of $La_2O_2CO_3$

3.1 Background research

In many of the previous works [14][15][16][17][32][33], rare-earth oxycarbonates are formed by heat treatment of the hydroxides. However the hydroxides tend to produce the oxides, which are thermally stable, during the heat treatment.

In my preliminary study [19][24][25], the synthesis of La oxycarbonates has been investigated through two different routes shown in Figure 3.1. One was from La hydroxide (Route#1) and the other was from La oxalate hydrate (Route#2). In Figure 3.1, “H” and “C” on the axes indicate the number of hydrogen and carbon atom in each compound, respectively.

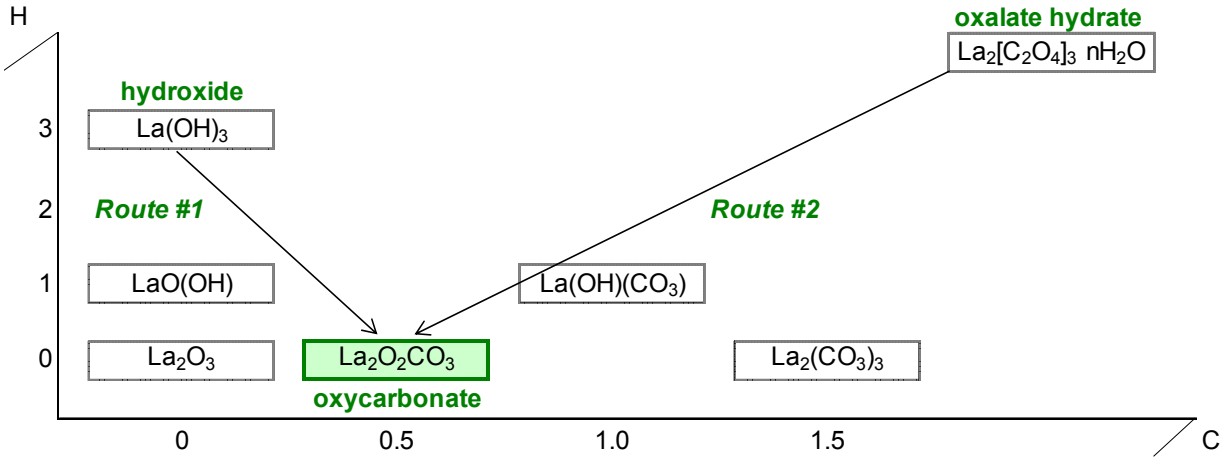

Figure 3.1 Synthetic routes of rare-earth oxycarbonates and relevant compounds [19].

It was difficult to form La oxycarbonates from La hydroxide (route #1) because of the tendency to form the oxide. Only the heat treatment of La hydroxide at 450°C for 18 hours provided La oxycarbonate but not reproducibly. In stark contrast to La hydroxide,

every heat treatment of La oxalate hydrate (route #2) provided La oxycarbonate with a good reproducibility. These results indicate that La oxalate hydrate is much better than La hydroxide as a starting material. Table 3.1 presents the different heat treatments I previously used for the synthesis of the hexagonal phase using the oxalate hydrate as a precursor [19].

Table 3.1 Heat treatment conditions and obtained materials [19].
(Starting material : La oxalate hydrate)

Time \ Temperature	450°C	500°C	550°C
2h	**m** + c		
6h	**m** + c	**m** + c	
18h	**m** + c	**m**	**m** + **h**
72h		**h**	

h = hexagonal $La_2O_2CO_3$, **m** = monoclinic $La_2O_2CO_3$, c = carbon residue

As one can observe, not all conditions were explored. It was however important to gain additional knowledge about what happens at 450°C and 550°C in the case of longer heat treatments. The additional heat treatments were necessary in order to:

- Check if a longer treatment at a lower temperature results in a complete phase transformation from monoclinic to hexagonal. This could allow for the optimization of the synthesis procedure;
- Check the effects of a prolonged thermal treatment at the highest temperature. This could give a good idea about the stability of the material in the case of long term operation.

3.2 Material synthesis and characterization

From the background above, two additional heat treatments: 1) 450°C for 72 hours and 2) 550°C for 72 hours, were implemented for La oxalate hydrate in the same manner as [19] and described in section 2.1.1. Figure 3.2 shows the XRD patterns after the heat treatments of La oxalate hydrate for the six conditions including the results from [19]. Table 3.2 summarizes the heat treatment conditions and obtained materials identified by the XRD. The 450°C for 72 hours and 550°C for 72 hours provided monoclinic $La_2O_2CO_3$ and hexagonal $La_2O_2CO_3$, respectively. It is important to note that in the case of the lower temperature even a significant increase of the duration of the thermal treatment did not result in the phase transformation from monoclinic to hexagonal. For the case of the highest temperature, I found that the material did not change from the oxycarbonate to the oxide, which is a good indication for its long term stability. The framed conditions in Table 3.2 were chosen to fabricate sensors for evaluation shown in next section.

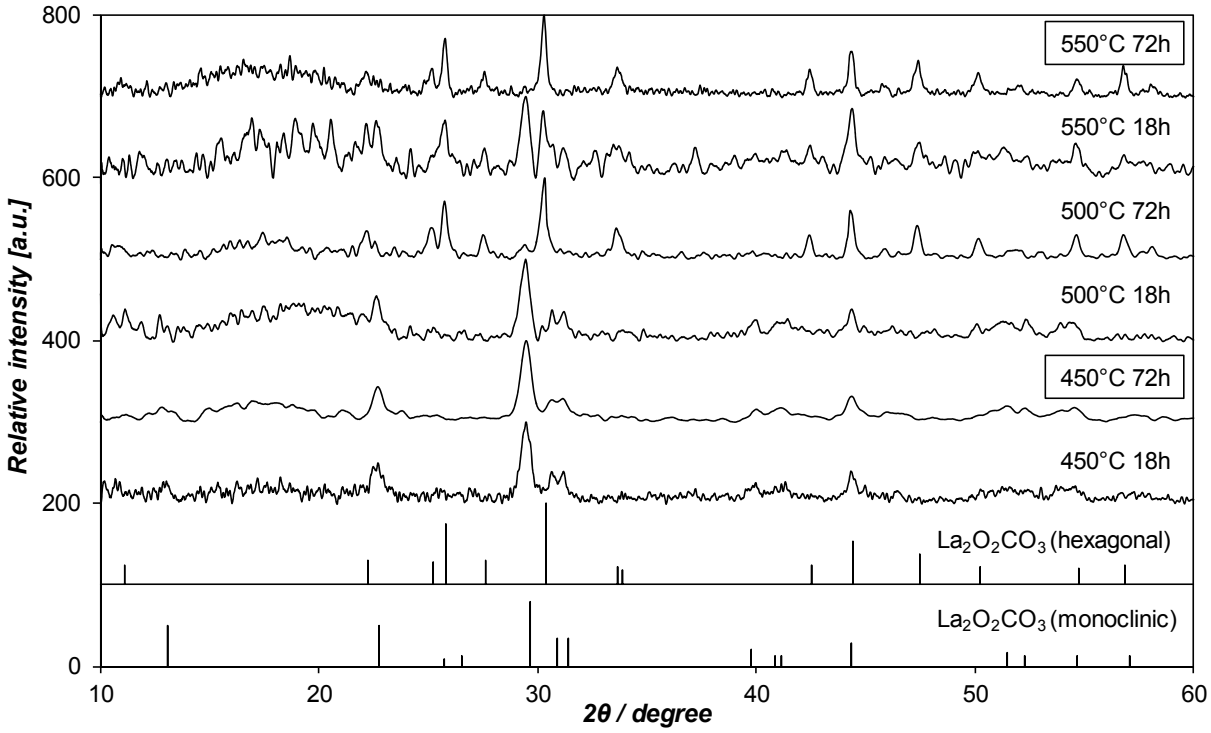

Figure 3.2 XRD patterns after the heat treatments of La oxalate hydrate for six heat treatment conditions.

Table 3.2 Summary of heat treatment conditions and obtained materials. (Starting material : La oxalate hydrate)

Time \ Temperature	450°C	500°C	550°C
2h	m + c		
6h	m + c	m + c	
18h	m + c	m	m + h
72h	m	h	h

h = hexagonal $La_2O_2CO_3$, **m** = monoclinic $La_2O_2CO_3$, c = carbon residue

3.3 Sensor evaluation

Six preparation conditions for sensor evaluation are summarized in Table 3.3. Three of them were hexagonal $La_2O_2CO_3$ from La hydroxide (No.1) and La oxalate hydrate (No.5 and No.6). The other three of them were monoclinic $La_2O_2CO_3$ from La oxalate hydrate (No.2, No.3, and No.4). Three or two sensors for each material were fabricated in the manner described in section 2.1.2 and their DC resistance was measured as shown in section 2.1.3 to compare the sensing properties among the 6 types of material using three sensors in total for each material; for No. 1, 2, 4 and 5 one sample was obtained in a previous synthesis, performed during the master thesis, and 2 samples were produced especially for the current study. All three sensors for No. 3 and 6 were newly produced.

Table 3.3 Preparation conditions for sensor evaluation.

No.	Starting material	Conditions of heat treatment	XRD results after heat treatment	Number of sensors	
				from [19]	total
1	La hydroxide	450°C 18 hours	La oxycarbonate (hexagonal)	1	3
2	La oxalate hydrate	450°C 18 hours	La oxycarbonate (monoclinic)	1	3
3	La oxalate hydrate	450°C 72 hours	La oxycarbonate (monoclinic)		3
4	La oxalate hydrate	500°C 18 hours	La oxycarbonate (monoclinic)	1	3
5	La oxalate hydrate	500°C 72 hours	La oxycarbonate (hexagonal)	1	3
6	La oxalate hydrate	550°C 72 hours	La oxycarbonate (hexagonal)		3

Figure 3.3 shows the variations of sensor signal at 1,000ppm CO_2 with the operating temperature for the six types of sensors when they were operated in humid air at 50% r.h.@20°C. The average value of three sensors was used for each displayed sensor signal. The sensor signal was the highest when they were operated at 300°C for every sensor except for No.6. In the case of No.6, the sensor signal at 250°C was marginally higher than at 300°C. From these results, it was confirmed that 300°C is suitable as the standard operating temperature. This was consistent with the results from my preliminary study [19].

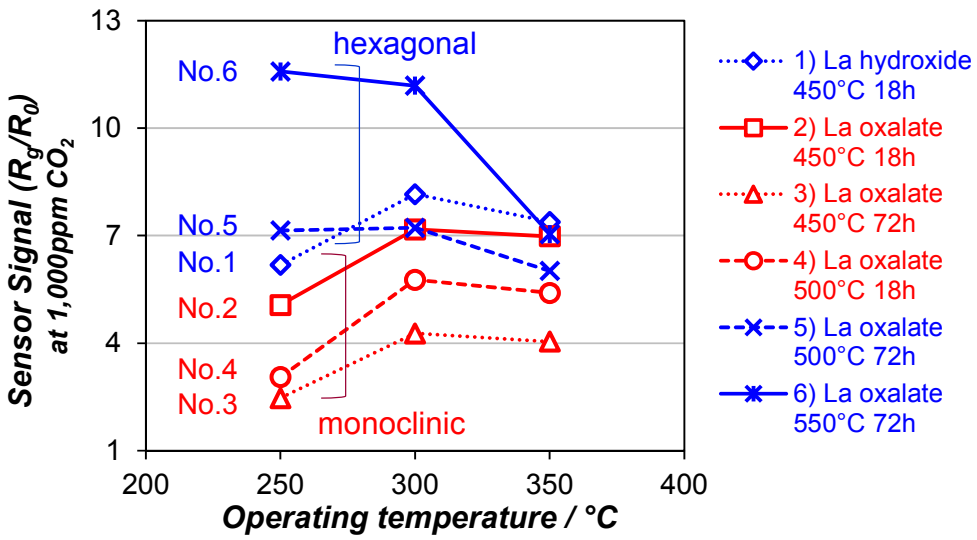

Figure 3.3 Sensor signal at 1,000ppm CO_2 vs. Operating temperature for six types of material. (Humidity = 50% r.h.@20°C)

Figure 3.4 shows the variations of sensor signal with CO_2 concentration at the standard operating temperature of 300°C for the six types of material. The best one of the three sensors is shown for each material. Every material exhibited a linear relationship between the sensor signal and the CO_2 concentration in a double

logarithmic scale. This indicates a power law dependence, which allows for a fit the calibration curve with:

$$Sensor\ signal = \beta\ [CO_2\ concentration]^{\alpha} \qquad (3.1)$$

The α corresponds to the slope of the calibration curve in a double logarithmic scale.

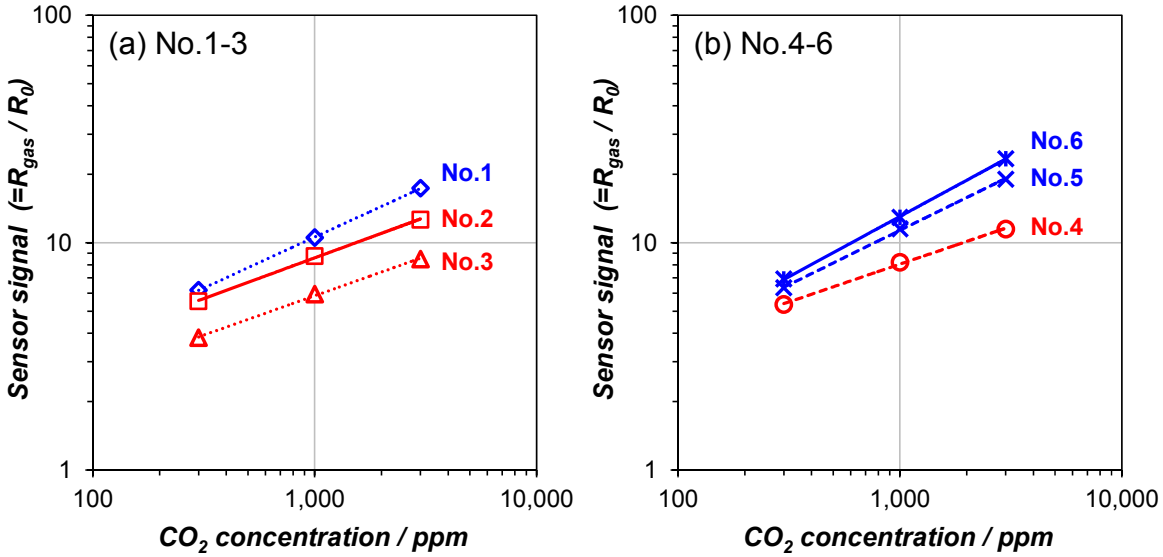

Figure 3.4 Sensor signal vs. CO_2 concentration for six types of material. (Operating temperature = 300°C, Humidity = 50% r.h.@20°C)

Figure 3.5 (a) and (b) summarize the results from DC resistance measurements. The average sensor signal at 1,000ppm CO_2 and the slope α of No.1, 5, and 6 (corresponding to hexagonal structure) were higher than those of No.2, 3, and 4 (corresponding to monoclinic structure), even though the dispersion in sensor signal of No.1 and No.5 were large. The condition No.6 was the best in terms of the sensor signal, the slope α, and their dispersions.

In order to test the stability, the three day long ageing process was performed in the same manner as [19] and described in section 2.2.4, and the results are summarized in

Figure 3.5 (c). The resistance changes after the ageing process (corresponding to the stability) of No.2, 3, and 4 were around three, meaning that the sensor resistance of No.2, 3, and 4 increased by about three times after the ageing process, while those of No.1, 5, and 6 were almost one, meaning that the sensor resistance of No.1, 5, and 6 were stable.

These results elucidate that the hexagonal structure possesses a higher sensitivity and stability than the monoclinic structure and No.6 is the best among six conditions.

Figure 3.6 shows the SEM images of the sensing layer surface for No.6 comparing with No.5 from [19]. The particles of No.6 were relatively uniform in size compared to No.5, which can lead to the difference in the dispersion of the sensor signal.

Regarding the heat treatment conditions, it was found that No.6 (550°C for 72 hours) shows the best performance. Accordingly this type of sensor was used as a representative for La in the subsequent studies.

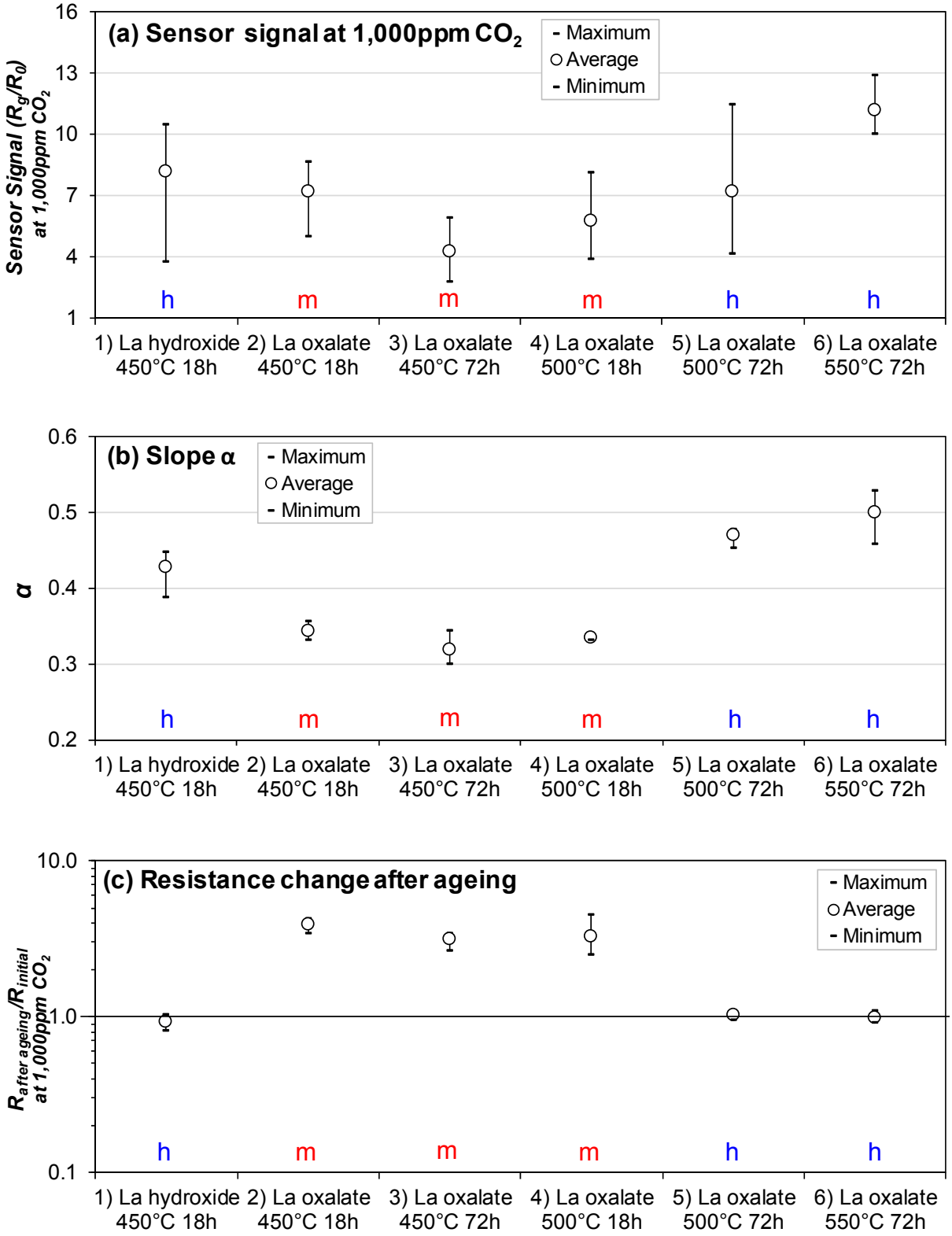

Figure 3.5 Summary of DC resistance measurements. The "m" and "h" stand for monoclinic and hexagonal structure, respectively.
(Operating temperature = 300°C, Humidity = 50% r.h.@20°C)

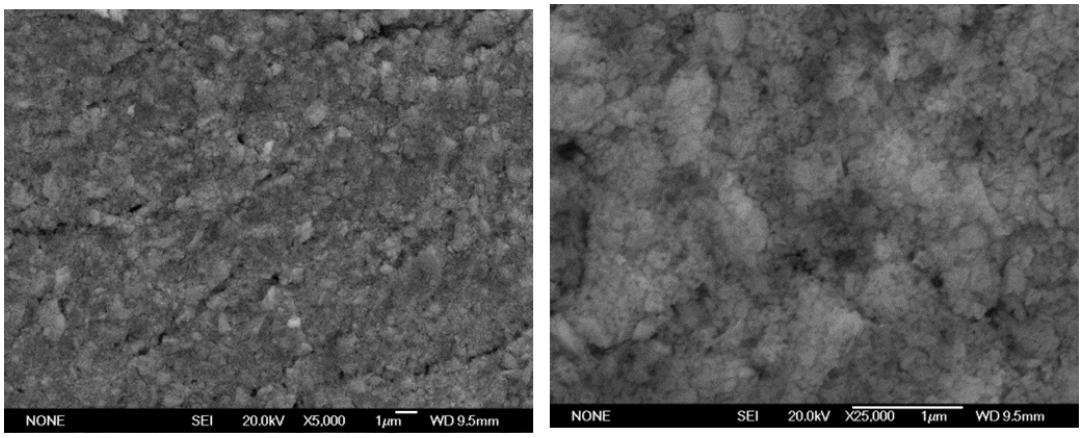

(a) No.6 ×5,000 ×25,000

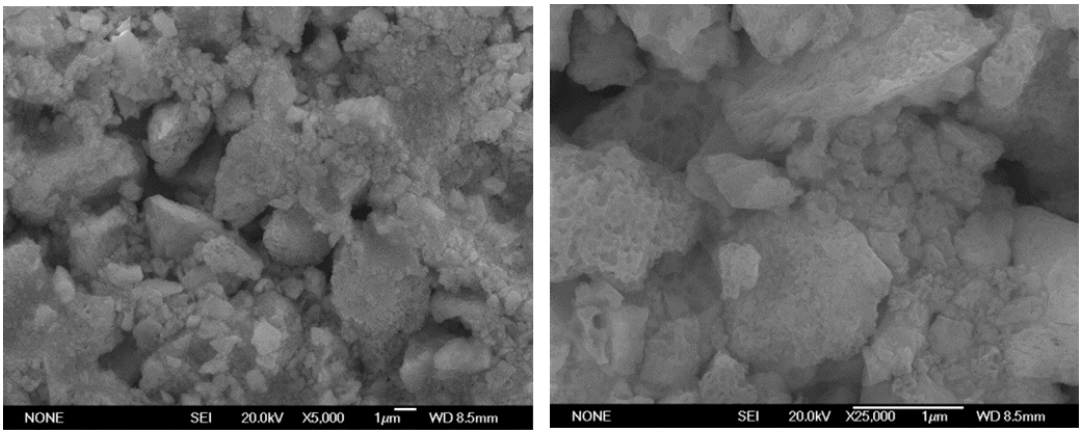

(b) No.5 ×5,000 ×25,000

Figure 3.6 SEM images of the sensing layer surface for No.6 comparing with No.5 from [19].

3.4 Operando XRD

To understand the mechanism of change in sensor resistance during the ageing process for the sensors based on monoclinic $La_2O_2CO_3$, I demonstrated that the resistance increased in direct correlation to the degree of the transformation from the

monoclinic structure into the hexagonal structure qualitatively by using operando XRD in my master thesis [19].

For a quantitative analysis of the results from operando XRD, one would need to obtain some kind of quantitative relationship between the electrical changes and the composition – percentage of hexagonal phase – of the material. To be able to quantify the latter, three different compositions of mixed powder of hexagonal $La_2O_2CO_3$ and monoclinic $La_2O_2CO_3$ were prepared and their XRD patterns were measured. The results shown in Figure 3.7 exhibit a good linear correlation between the composition ratio and the peak height ratio which was derived from (3.2)

$$\text{Peak height ratio: } P = I_{hexagonal\ (103)} / (I_{hexagonal\ (103)} + I_{monoclinic\ (031)}) \qquad (3.2)$$

where $I_{hexagonal\ (103)}$ was the peak height of hexagonal (103) and $I_{monoclinic\ (031)}$ was the peak height of monoclinic (031).

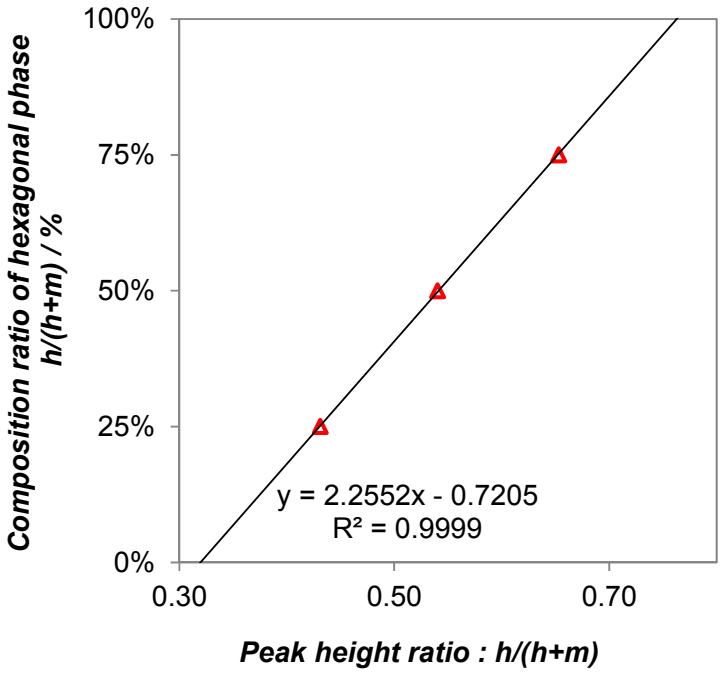

Figure 3.7 Composition ratio vs. Peak height ratio of hexagonal phase

The fitted correlation line was represented as (3.3)

Composition ratio of the hexagonal phase: $C = 2.2552 * P - 0.7205$ (3.3)

For the sensor based on monoclinic $La_2O_2CO_3$ prepared by the condition No.4 in Table 3.3, Figure 3.8 shows the time variation of the sensor resistance from the initial value and the transformation ratio : h / (h+m), which was calculated by using the findings presented in Figure 3.7 and the corresponding equation (3.3).

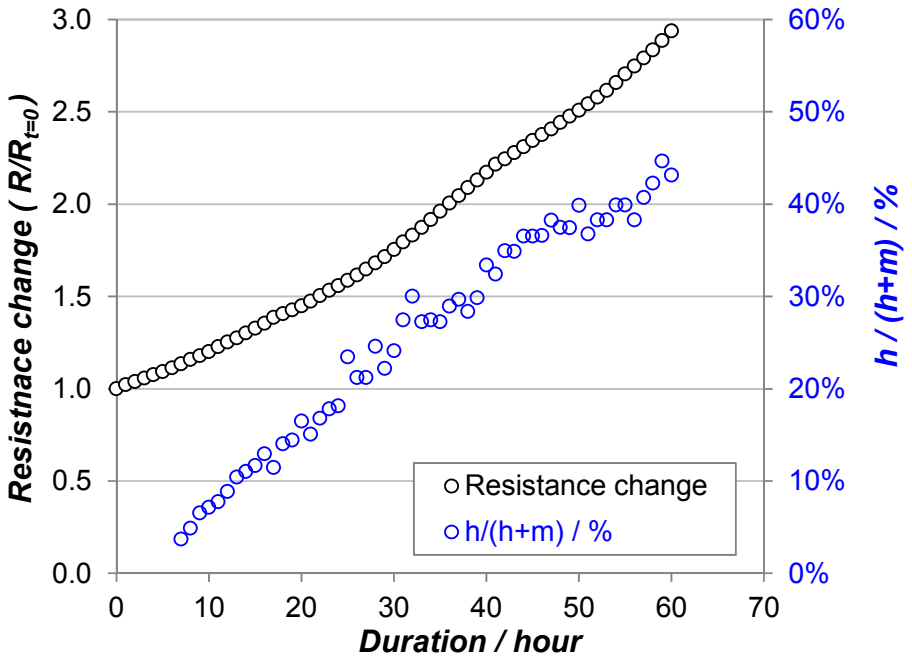

Figure 3.8 Time variation of sensor resistance from the initial value and the transformation ratio: *h / (h+m)*.

The extrapolated resistance change at 100 % in Figure 3.9 is approximately ten, which is consistent with the results from [19] about the difference in resistance between monoclinic $La_2O_2CO_3$ and hexagonal $La_2O_2CO_3$.

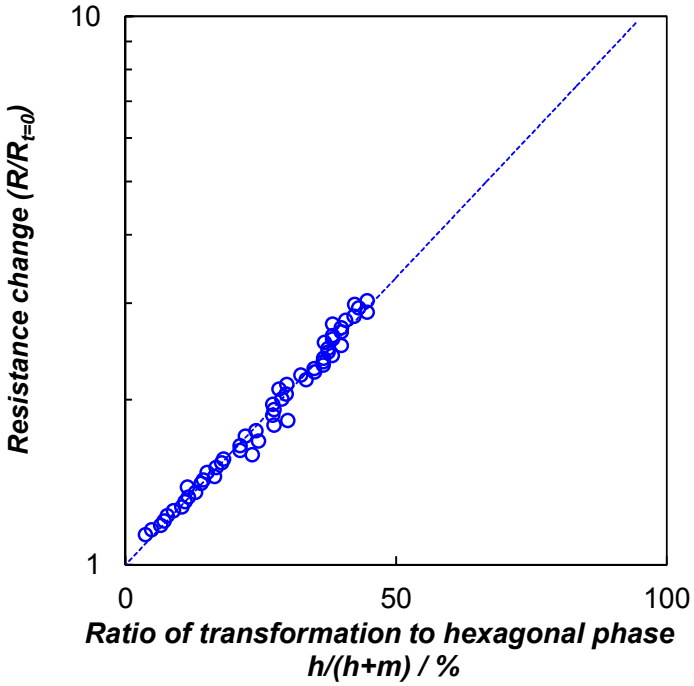

Figure 3.9 Resistance change vs. Ratio of transformation to hexagonal phase.

3.5 Summary and discussion on stabilizing the synthesis and sensing properties of $La_2O_2CO_3$

I have reviewed my preliminary study indicating that La oxalate hydrate is a better precursor for reproducibly synthesizing $La_2O_2CO_3$ compared to La hydroxide which has been used in many of previous works; in order to confirm that I explored additional synthesis conditions and enlarged the statistical basis of my study.

The two additional heat treatments (450°C for 72 hours and 550°C for 72 hours) have been implemented and the sensors based on six types of material from the six different heat treatments have been prepared and evaluated. Three of them were hexagonal $La_2O_2CO_3$ from La hydroxide and La oxalate hydrate. The other three of them were monoclinic $La_2O_2CO_3$ from La oxalate hydrate.

The sensor signals to CO_2 were basically the highest at an operating temperature of 300°C. From these results, it was confirmed that 300°C was suitable for the standard operating temperature. This was consistent with the results from my preliminary study.

Every material exhibited a linear relationship between the sensor signal and the CO_2 concentration in a double logarithmic scale. This indicates a power law dependence, which allows for a fit the calibration curve with:

$$\textit{Sensor signal} = \beta\,[CO_2\ \textit{concentration}]^{\alpha} \qquad (3.1)$$

The α corresponds to the slope of the calibration curve in a double logarithmic scale. The average sensor signals at 1,000ppm CO_2 and the slope α of the sensors corresponding to hexagonal structure were higher than those of monoclinic structure, and the condition No.6 (Starting material = La oxalate hydrate, Heat treatment conditions = 550°C for 72 hours) was the best in terms of the sensor signal, the slope α, and their dispersions.

In order to test the stability, the three day long ageing process was performed. The resistance of sensors based on monoclinic $La_2O_2CO_3$ increased by about three times after the ageing process, while those of hexagonal $La_2O_2CO_3$ were stable.

From the SEM images, the particles of No.6 were relatively uniform in size compared to the condition No.5 (Starting material = La oxalate hydrate, Heat treatment conditions = 500°C for 72 hours), which can lead to the difference in the dispersion of the sensor signal.

Regarding the heat treatment conditions, it was found that the condition No.6 (Starting material = La oxalate hydrate, Heat treatment conditions = 550°C for 72 hours) shows the best performance. Accordingly this type of sensor was used as a representative for La in the subsequent studies.

4 Material exploration for rare-earth based chemoresistive CO_2 sensors

4.1 Material synthesis

According to the previous chapter, the heat treatment of La oxalate hydrate in ambient air (approximately 20°C 50% r.h. with 400 ppm CO_2) is a reproducible method for synthesizing La oxycarbonate. In order to obtain the other rare-earth oxycarbonates, heat treatments of the rare-earth organic acid salts hydrate such as the oxalate hydrate or acetate hydrate were implemented in the same manner as section 2.1.1.

Table 4.1 shows the heat treatment conditions and the obtained materials identified by XRD. “h”, ”m”, and “c” stand for hexagonal, monoclinic, and cubic structure respectively. Precursors were the oxalate hydrate or the acetate hydrate depending on the availability. The XRD patterns of powders highlighted yellow in Table 4.1 are shown in Figure 4.1-4.3 with the references [34][35][36][37][38].

La formed hexagonal oxycarbonate, monoclinic oxycarbonate, or the mixture of the two phases. Nd formed monoclinic oxycarbonate under the conditions of 450°C 18h or 500°C 18h. Sm formed monoclinic oxycarbonate only under the conditions of 450°C 18h. In all other cases, oxides were produced.

Ten types of materials highlighted yellow in Table 4.1 were chosen for the sensor characterizations. The ten types of sensors were fabricated in the manner described in section 2.1.2.

Table 4.1 Heat treatment conditions and obtained materials identified by XRD.

atomic number→	**La** 57	**Ce** 58	**Nd** 60	**Sm** 62	**Gd** 64	**Dy** 66	**Er** 68	**Yb** 70
Precursor / Condition	oxalate hydrate	oxalate hydrate	acetate hydrate	acetate hydrate	oxalate hydrate	acetate hydrate	oxalate hydrate	acetate hydrate
550°C 72h	$La_2O_2CO_3$(h)	CeO_2(c)	Nd_2O_3(c+h)	Sm_2O_3(c)	Gd_2O_3(c)	Dy_2O_3(c)	Er_2O_3(c)	Yb_2O_3(c)
550°C 18h	$La_2O_2CO_3$(m+h)	CeO_2(c)	Nd_2O_3(c+h)					
500°C 72h	$La_2O_2CO_3$(h)		Nd_2O_3(c+h)					
500°C 18h	$La_2O_2CO_3$(m)		$Nd_2O_2CO_3$(m)	Sm_2O_3(c)	Gd_2O_3(c)	Dy_2O_3(c)		
450°C 72h	$La_2O_2CO_3$(m)			Sm_2O_3(c)				
450°C 18h	$La_2O_2CO_3$(m)	CeO_2(c)	$Nd_2O_2CO_3$(m)	$Sm_2O_2CO_3$(m)	Gd_2O_3(c)	Dy_2O_3(c)		Yb_2O_3(c)

h=hexagonal, m=monoclinic, c=cubic

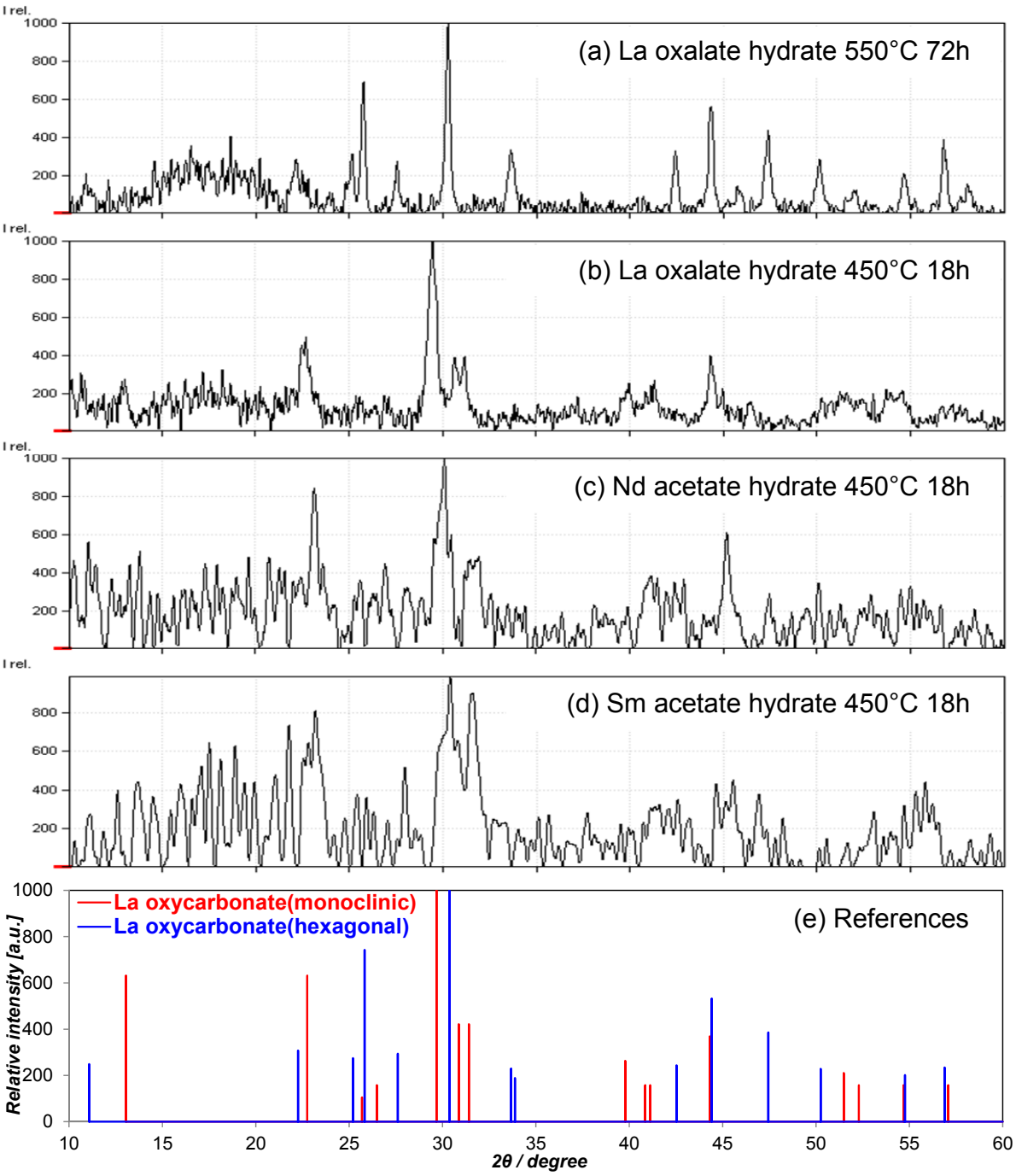

Figure 4.1 XRD patterns of powders after heat treatment.
(starting material : La oxalate hydrate, Nd acetate hydrate, Sm acetate hydrate)

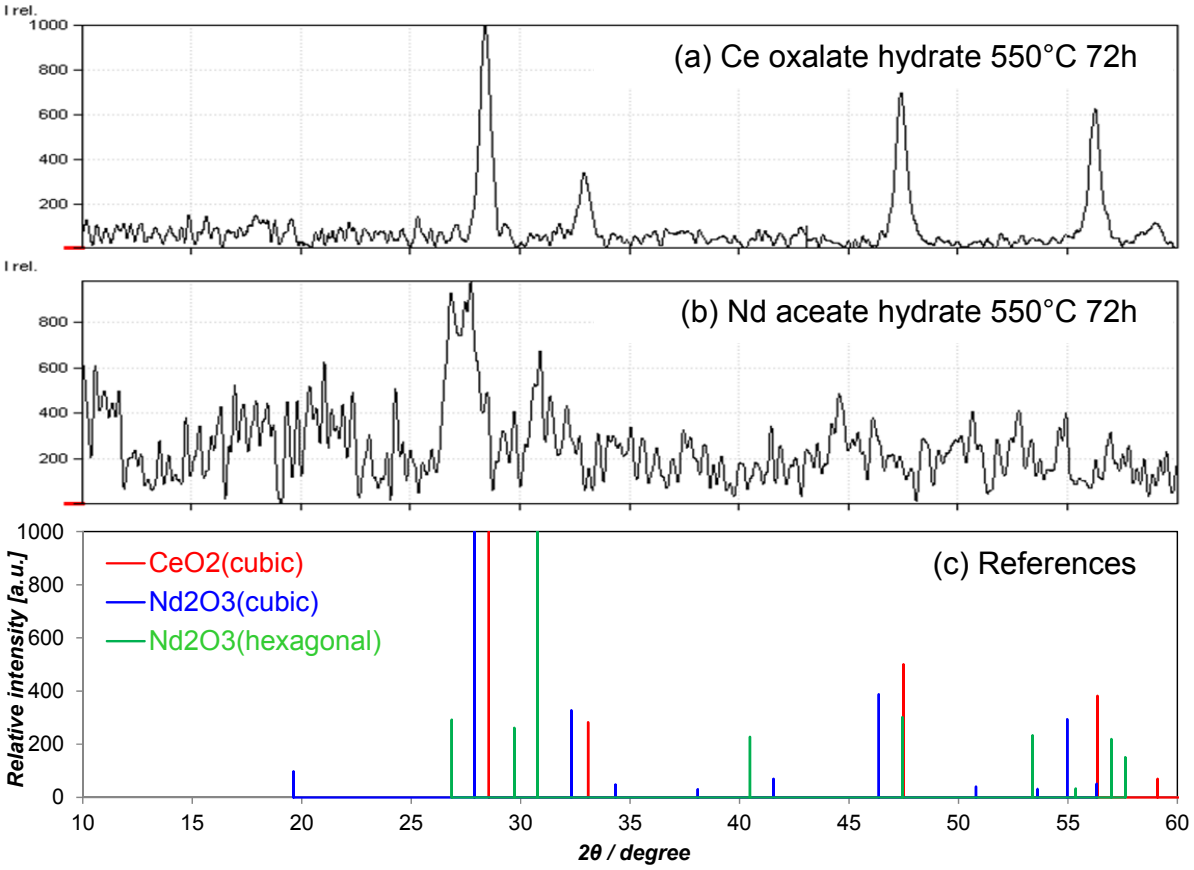

Figure 4.2 XRD patterns of powders after heat treatment.
(starting material: Ce oxalate hydrate, Nd acetate hydrate)

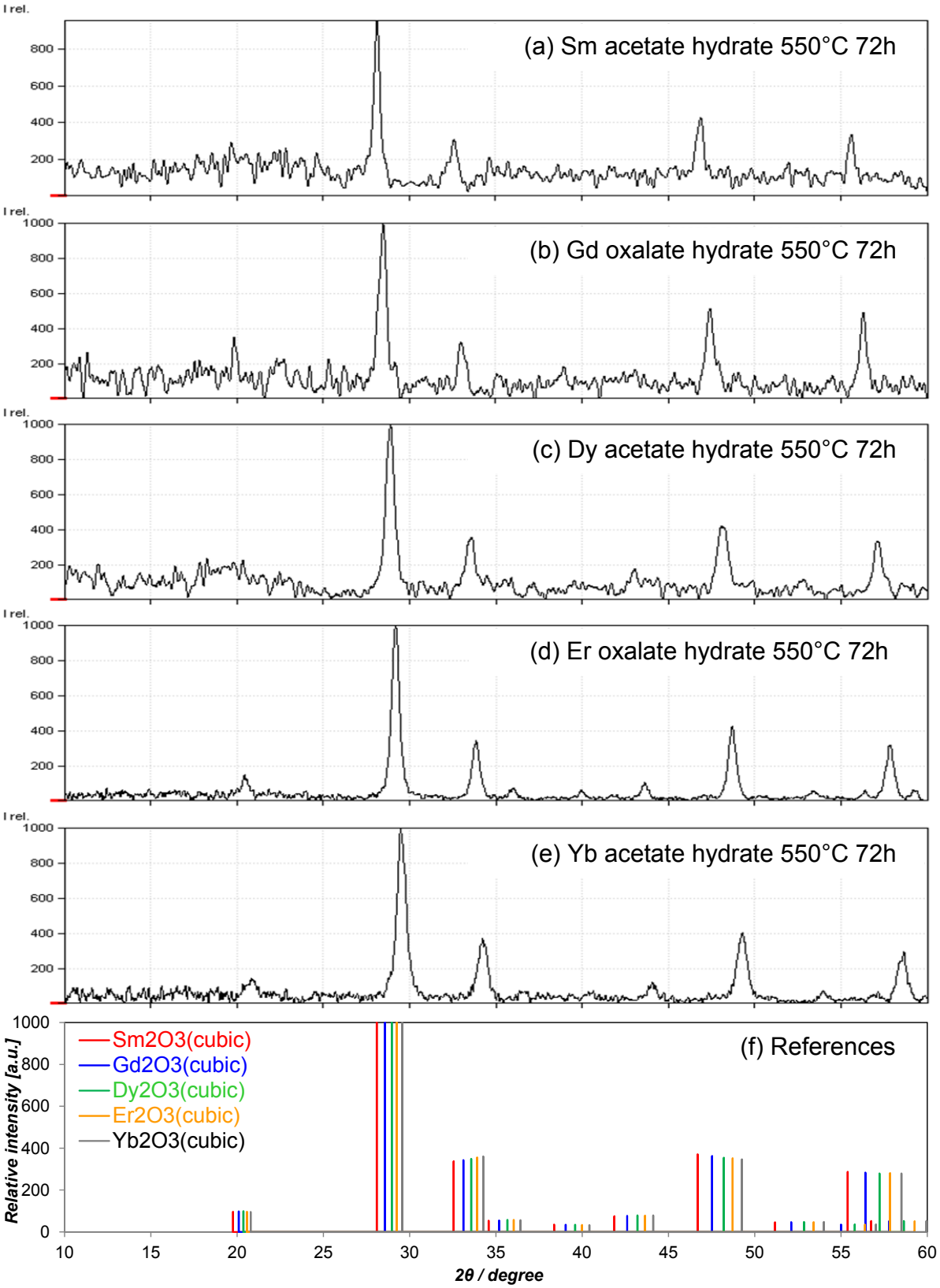

Figure 4.3 XRD patterns of powders after heat treatment.
(starting material: Sm, Dy and Yb acetate hydrate, Gd and Er oxalate hydrate)

4.2 Sensor signal to CO_2

Figure 4.4 and Figure 4.5 show the variations of sensor signals with CO_2 concentration and the sensor signals at 1,000ppm CO_2, respectively, for the 10 types of materials. The measuring conditions were 20°C 50% r.h. at an operating temperature of 300°C.

All materials, except for CeO_2 and Nd_2O_3, were sensitive to CO_2. Among the oxycarbonates, the sensor signal of La was the highest. One can remark that the sensor signal at 1,000ppm CO_2 of the oxycarbonates decreases with the increase of the atomic number, and the sensor signal of the oxides increases until Gd and then decreases with the increase of the atomic number. In the case of the two elements which formed both oxycarbonates and oxides, Nd oxycarbonate was much better than Nd oxide, but Sm oxycarbonate and Sm oxide were approximately the same. CeO_2 and Nd_2O_3 were eliminated from the subsequent studies because of their poor sensor signal.

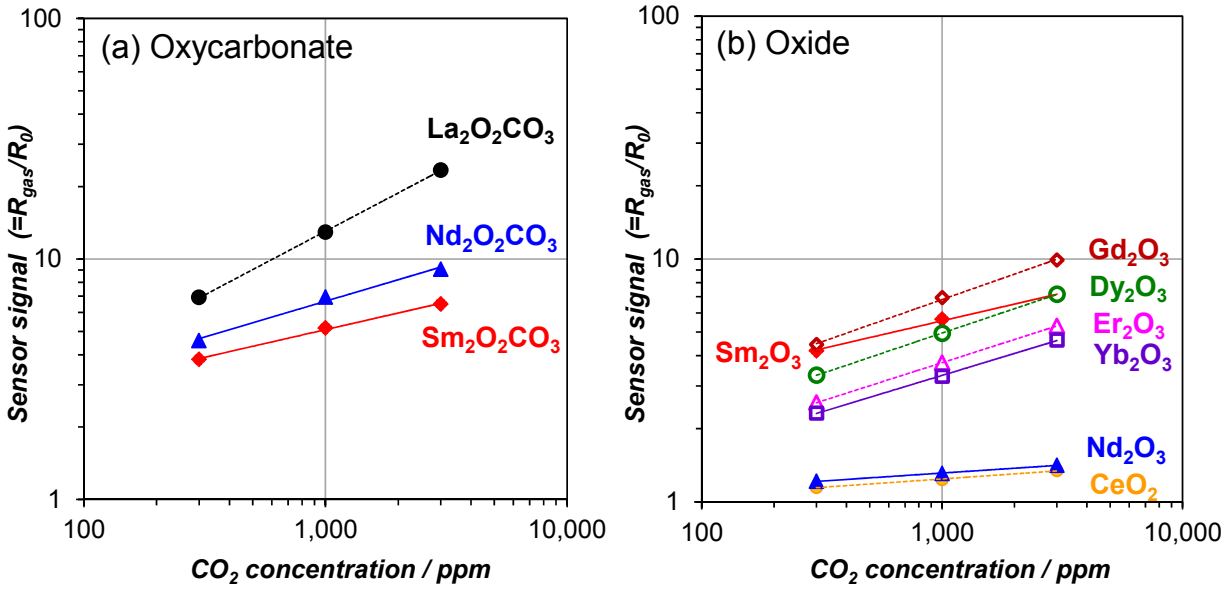

Figure 4.4 Sensor signal vs. CO_2 concentration [39].
(20°C 50% r.h., operating temperature =300°C)

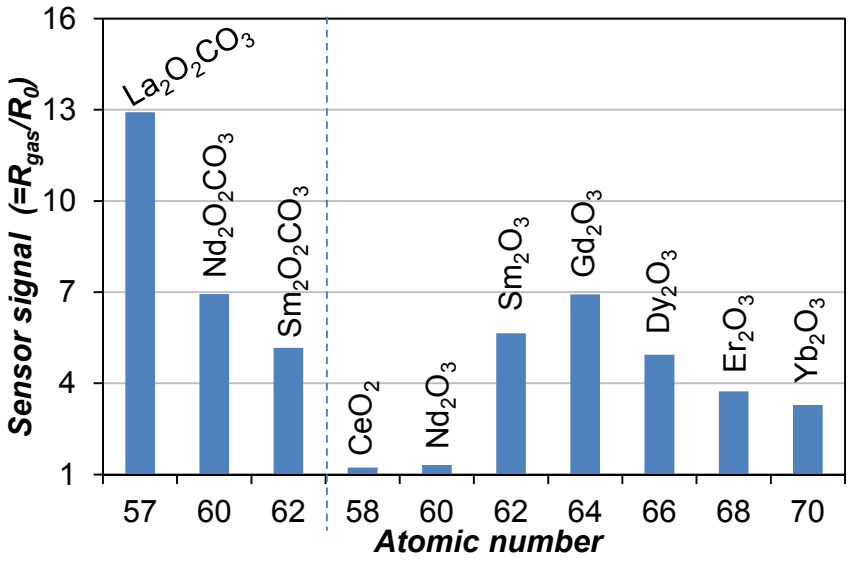

Figure 4.5 Sensor signals at 1,000 ppm CO_2 in order of the atomic number [39][40]. (20°C 50% r.h., operating temperature =300°C)

4.3 Stability

In order to test the stability of the CO_2 sensitive materials, the standard ageing process was performed in the same manner as shown in section 3.2.2. Figure 4.6 shows the relative change of CO_2 sensing properties after the ageing process.

All sensors, except for monoclinic Nd oxycarbonate, were stable during the ageing process. The sensor resistance and sensor signal of Nd oxycarbonate decreased significantly indicating that Nd oxycarbonate is not stable and can be transformed into the oxide. Accordingly Nd oxycarbonate was eliminated from the further evaluations.

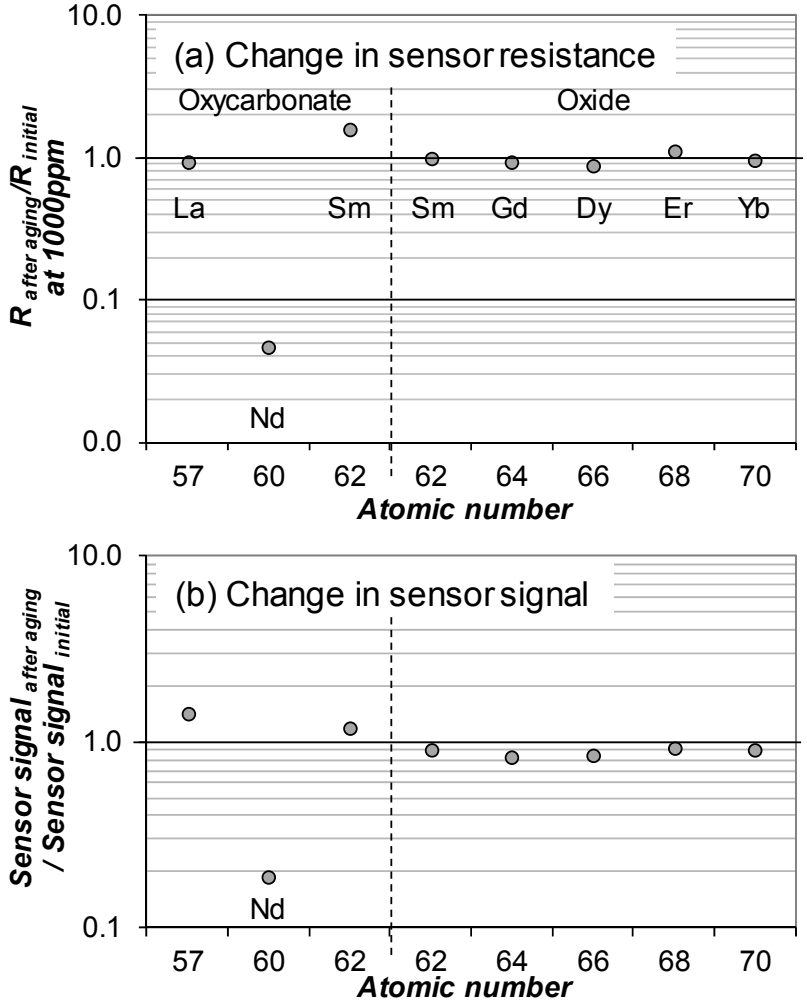

Figure 4.6 Change of CO_2 sensing properties after ageing process, (a) Change in sensor resistance at 1,000ppm CO_2, (b) Change in sensor signal at 1,000ppm CO_2

4.4 Influence of humidity

The variations of sensor resistance with CO_2 concentration for three humidity conditions were measured. Figure 4.7 shows the results for (a) $La_2O_2CO_3$, (b) $Sm_2O_2CO_3$, (c) Sm_2O_3, (d) Gd_2O_3, (e) Dy_2O_3 and (f) Yb2O3. In all cases, the sensor resistance at a certain CO_2 concentration decreased with the increase of humidity. However, the slopes were almost the same among the three humidity conditions indicating that the influence of humidity on the sensitivity to CO_2 is small.

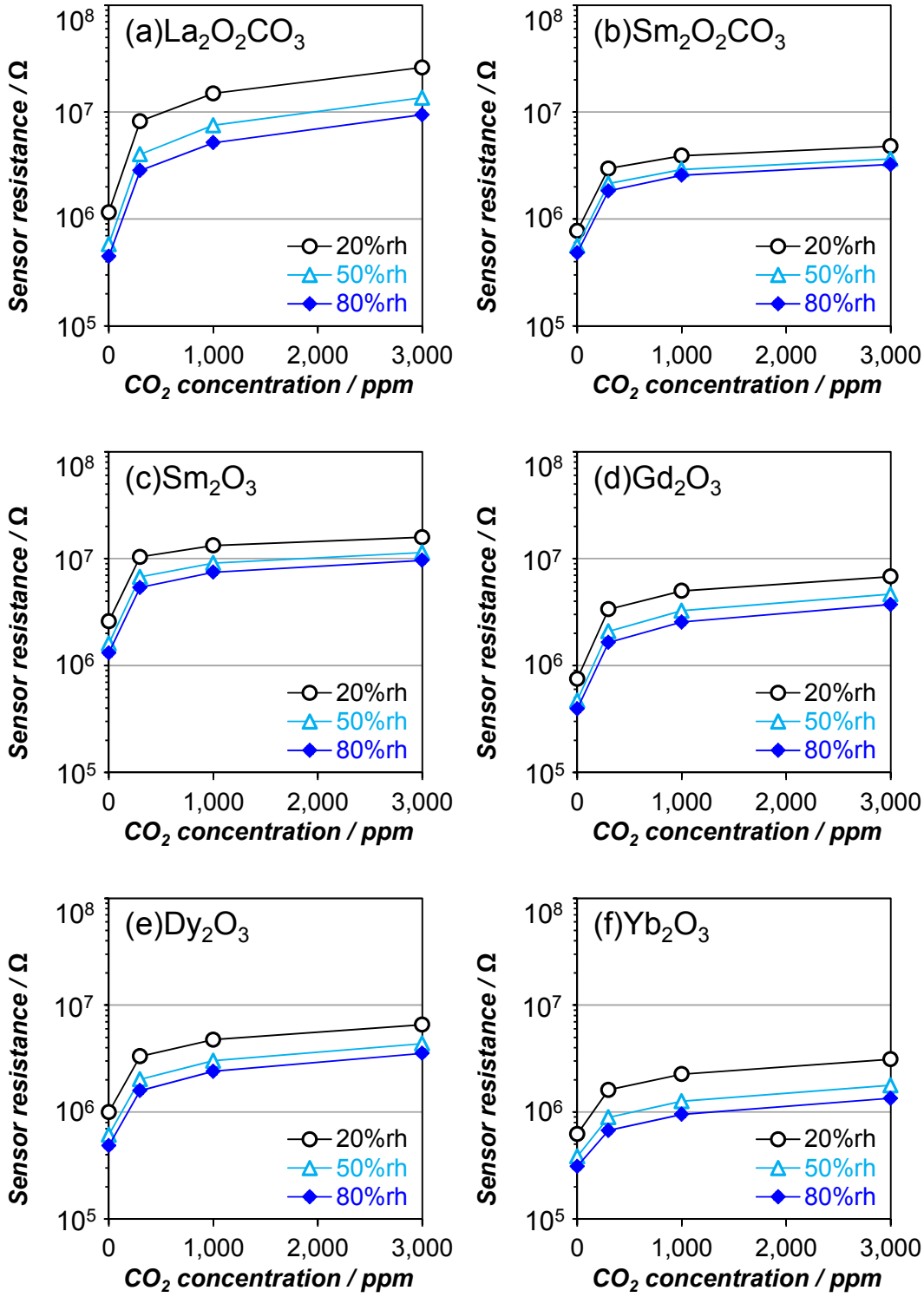

Figure 4.7 Sensor resistance vs. CO_2 concentration for three humidity conditions. (20°C 20-80% r.h., operating temperature =300°C)

4.5 Selectivity and Sensitivity up to 10,000ppm CO_2

The selectivity and sensitivity up to 10,000ppm CO_2 were evaluated using all remaining sensors in the manner described as 2.2.1.3. Figure 4.8 shows the Sensor signals at 400ppm of CO_2, 100ppm of ethanol (EtOH), CO, and H_2. 400 ppm CO_2 is the minimum value in a normal atmosphere and 100ppm of ethanol, CO, and H_2 are more than the maximum values in the normal atmosphere. All materials were sensitive to ethanol and CO, but in all cases the sensor signals at 400ppm CO_2 were higher than the sensor signals at 100ppm of ethanol and CO. Moreover, none of the sensors were sensitive to H_2. These results indicate good selectivity.

Figure 4.9 shows the dependencies of the sensor signal on the concentrations of CO_2, ethanol, CO, and H_2 for (a) $La_2O_2CO_3$, (b) $Sm_2O_2CO_3$, (c) $Sm_2O_2CO_3$, (d) Gd_2O_3, (e) Dy_2O_3 and (f) Yb_2O_3. All of them exhibit good linearity up to 10,000 ppm of CO_2 on a double logarithmic scale and hexagonal La oxycarbonate was the best among them from the point view of selectivity and sensitivity corresponding to the slope.

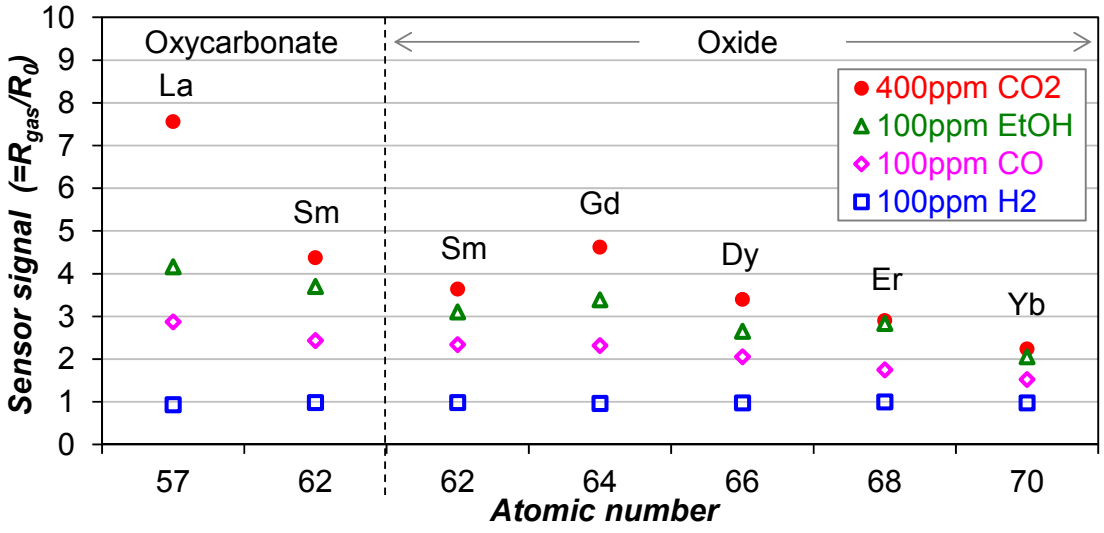

Figure 4.8 Sensor signals at 400ppm of CO_2, 100ppm of ethanol (EtOH), CO, and H_2 for $La_2O_2CO_3$, $Sm_2O_2CO_3$, Sm_2O_3, Gd_2O_3, Dy_2O_3, Er_2O_3, and Yb_2O_3 [39]. (20°C 50% r.h., operating temperature = 300°C)

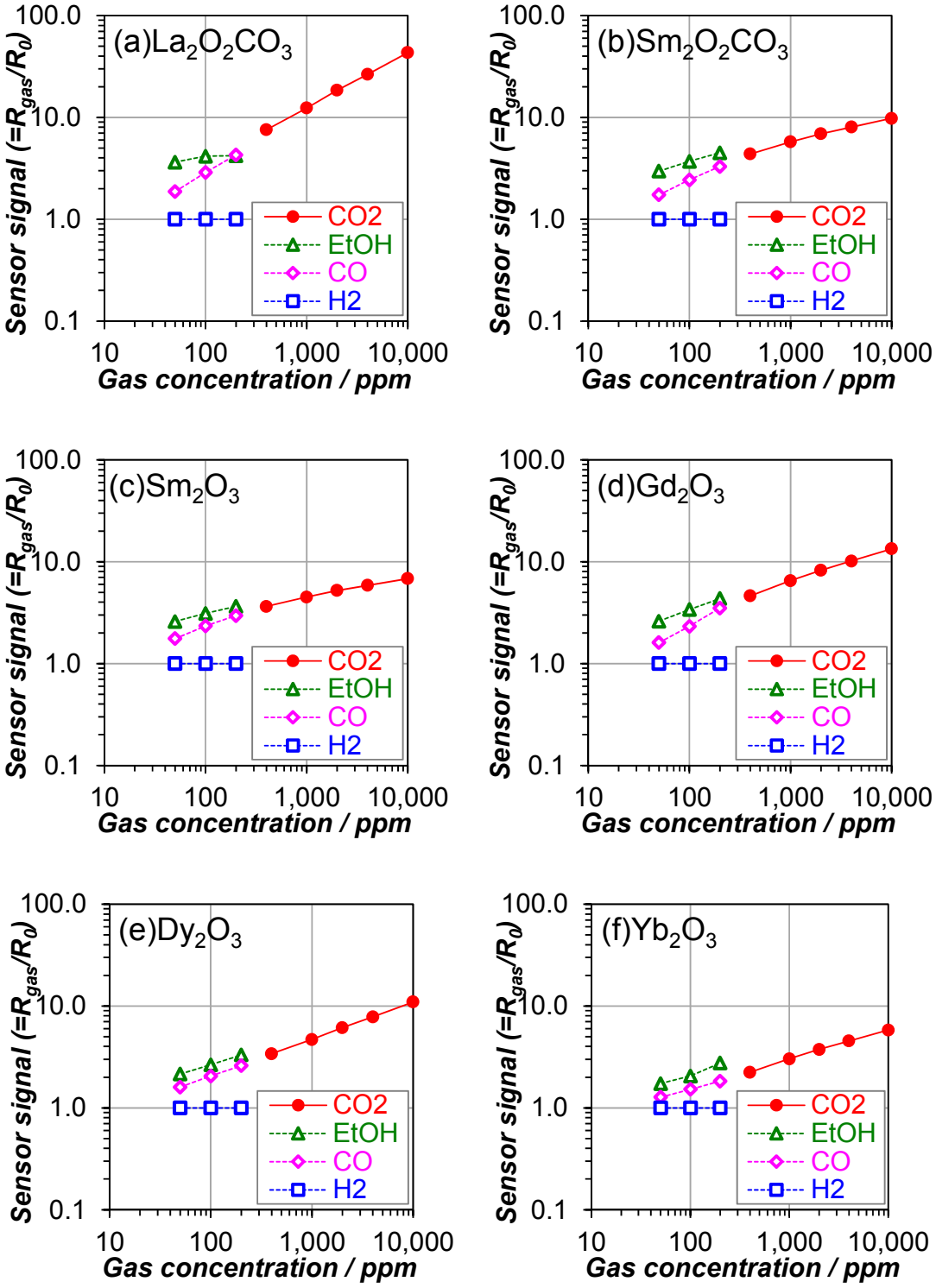

Figure 4.9 Sensor signal vs. gas concentration of CO_2, ethanol, CO, and H_2. (20°C 50% r.h., operating temperature = 300°C)

4.6 Summary and discussion on the material exploration for rare-earth based chemoresistive CO_2 sensors

I have tried to synthesize rare-earth oxycarbonates by heat treatment in ambient air (approximately 20°C 50% r.h. with 400 ppm CO_2) from the oxalate hydrate or the acetate hydrate. As a result, La, Nd and Sm formed oxycarbonates. In all other cases, oxides were produced. Among the oxides, Ce formed dioxide CeO_2, the other elements formed sesquioxides Ln_2O_3 (Ln = Nd, Sm, Gd, Dy, Er, and Yb). The crystal structure of Nd_2O_3 was a mixture of cubic and hexagonal, while the other oxides crystalized in cubic structure. These results are good accordance with the phase diagrams of the rare earth sesquioxide polymorphs in [41][42].

Ten types of materials, rare-earth oxycarbonate $Ln_2O_2CO_3$ (Ln = La, Nd, and Sm) and rare-earth oxides Ln_2O_3 (Ln = Nd, Sm, Gd, Dy, Er, and Yb) and LnO_2 (Ln = Ce), were chosen for the sensor evaluations.

All the materials, with the exception of CeO_2 and Nd_2O_3, were sensitive to CO_2. It is remarkable that rare-earth oxides Ln_2O_3 (Ln = Sm, Gd, Dy, Er, and Yb) crystalizing in cubic structure exhibited a chemoresistive effect for CO_2. These results are new findings exploding the indication in [15] that CO_2 sensing is linked to the formation of the oxycarbonate phase.

Among the CO_2 sensitive materials, only Nd oxycarbonate was not stable. It is thought that Nd oxycarbonate was transformed into the oxide. All others exhibited sufficient properties for practical use in terms of the stability, influence of humidity, selectivity, and the linearity of sensitivity up to 10,000ppm CO_2.

There was a trend that the sensor signal, sensitivity, and selectivity of the oxycarbonates decreased with increasing the atomic number of the rare-earth, and

those of the oxides increased until Gd and then decreased with increasing the atomic number. La oxycarbonate (hexagonal) was the best among all of them. Concerning the trend with atomic number of rare-earth elements, there are a lot of reports [43][44][45][46][47][48][49] investigating systematically the properties of rare-earth oxides in terms of the melting point, lattice parameter, band gap, dissociation enthalpies, first ionization potential, standard Gibbs energy of the formation, electrical conductivity, and so on. The trend of dissociation enthalpies of lanthanoid oxides and ions shown in [43] is similar to that of sensor signal at 1,000 ppm CO_2 shown in Figure 4.5, which can be a clue to clarify the cause of the difference in sensitivity depending on the rare-earth element, and to develop a better sensing material.

5 Basic understanding of the sensing mechanism

5.1 Overview

For basic understanding of the sensing mechanism, I have conducted comprehensive and systematic operando characterization. Specifically, the results from AC impedance spectroscopy, Work function, XRD, and DRIFTS have been obtained mainly for the best performing hexagonal La oxycarbonate ($La_2O_2CO_3$) under actual gas sensing conditions, leading to clarify the mechanism of the electrical conduction and the CO_2 sensing.

5.2 Operando AC impedance spectroscopy

5.2.1 Variation of Cole-Cole plot with CO_2 concentration

AC impedance spectroscopy of hexagonal $La_2O_2CO_3$ based sensor was measured in humid air with varying CO_2 concentration at the standard operating temperature of 300°C.

Figure 5.1 shows the Cole-Cole plots of the results in a complex plane. In Figure 5.1, the points show the experimental results for six CO_2 conditions and the lines are fitted results using the equivalent circuit, assuming a general semi-conductive polycrystalline material, where grain-grain boundaries or grain-electrode boundaries can form space charge regions as described in section 2.3.2. The data appeared well fit.

Figure 5.2 shows the CO_2 dependency of the fitted parameters corresponding to the results in Figure 5.1. Figure 5.3 shows the variation of R_2 with CO_2 concentration on a

double logarithmic scale. R_n (n=1-3), C_1, and CPE_m (m=1-2) represent the resistances, the capacitance and capacitances of Constant Phase Element in Figure 2.12. The p values of CPE_2 were around 0.8, and p values of CPE_3 were between 0.5 and 0.7. C_1 and R_1 were almost constant and much smaller than the others. R_2 was bigger than R_3 by almost one order of magnitude, and the CO_2 dependency followed the power law. This indicates that the parallel combination of R_2▪CPE_2 is the dominant contribution corresponding to electronic conduction depending on the band bending.

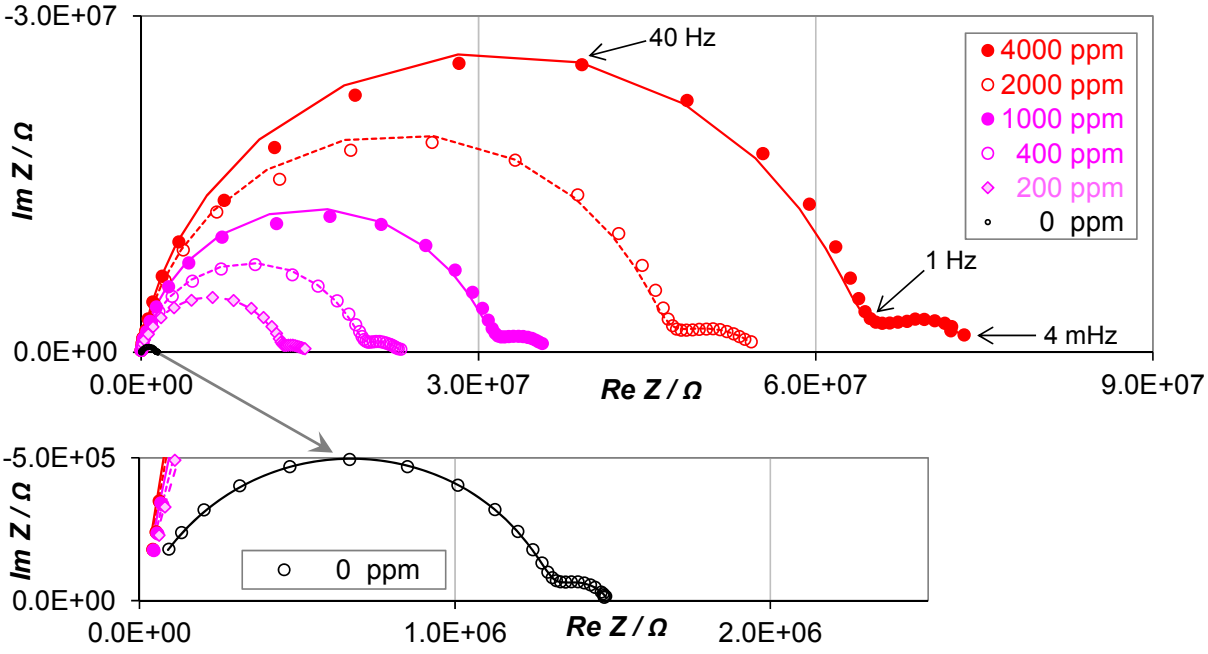

Figure 5.1 Variation of Cole-Cole plot with CO_2 concentration for hexagonal $La_2O_2CO_3$ based sensor.
(20 °C 50 % r.h., operating temperature = 300°C)

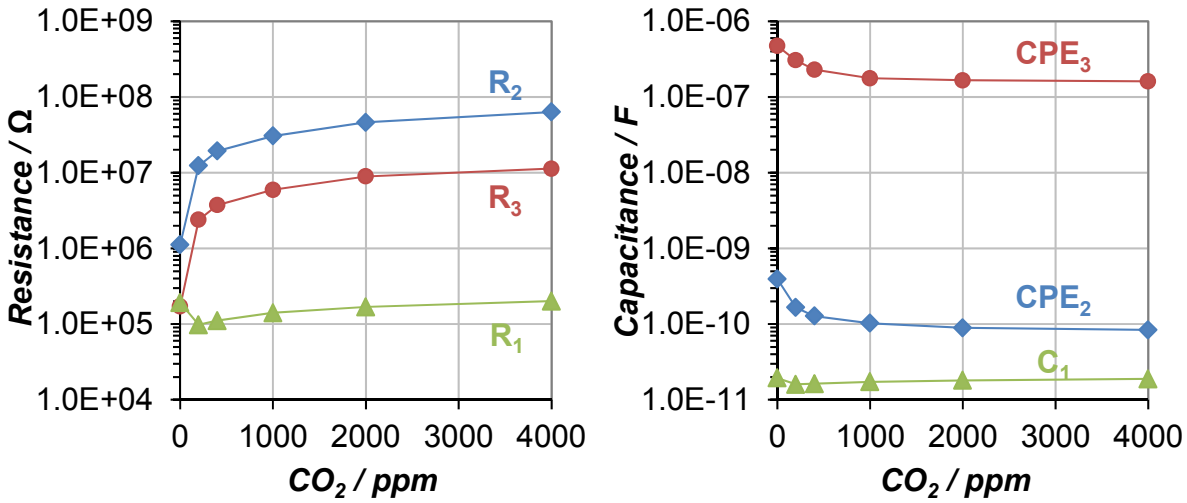

Figure 5.2 Fitted parameters of the equivalent circuit.

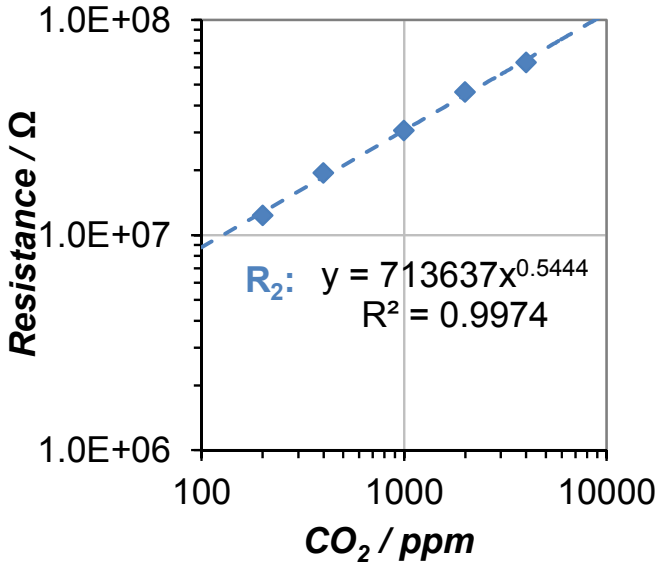

Figure 5.3 R_2 vs. CO_2 concentration in a double logarithmic scale.

5.2.2 Cole-Cole plots for three different types of electrodes

Figure 5.4 shows the Cole-Cole plots for hexagonal $La_2O_2CO_3$ based sensors using three different types of electrodes when they were operated at 300 °C with 400 ppm CO_2 exposure in humid air. The humidity condition was 20°C 50 % r.h.. The ***Z**** was relative impedance normalized by the maximum value of - ***Im Z*** of each electrode type. Each of electrodes possessed the similar interdigitated shape as shown in Figure 2.2 with a different dimension shown in Table 5.1. Electrode A is standard one in this work and the plots is identical to the corresponding plots in Figure 5.1. There were two half-circles in Figure 5.4, where the first one corresponding to the higher frequencies was larger than the depressed second one corresponding to the lower frequencies, and the portion of the second half-circle depended on the electrode dimension. This indicates that the second half-circle originates from grain-electrode boundaries and the first half-circle originates from grain-grain boundaries, which form space charge regions and band vending leading to the dominant contribution in resistance change.

From these results, the hypotheses that the dominant charge carriers are electronic in nature (electrons or holes) and that the conduction mechanism is controlled by the band bending at the grain-grain boundaries, which depends on the composition of the ambient atmosphere, seem to be valid.

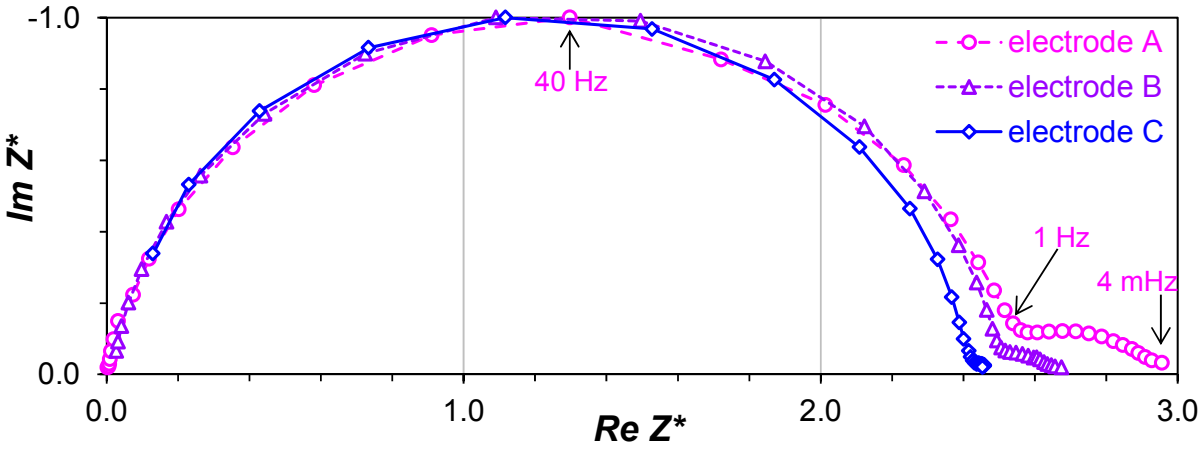

Figure 5.4 Cole-Cole plots for hexagonal $La_2O_2CO_3$ based sensors using three different types of electrodes.
(20 °C 50 % r.h. + 400 ppm CO_2, operating temperature = 300°C)

Table 5.1 Dimensions of the three types of electrodes.

No.	Type	Gap between fingers	Number of fingers
1	electrode A (standard)	10 μm	260
2	electrode B	30 μm	86
3	electrode C	100 μm	25

5.3 Operando Work function measurement

Contact Potential Difference (CPD) and DC resistance of hexagonal $La_2O_2CO_3$ based sensor were measured simultaneously under the operating conditions using the Kelvin probe method as described in section 2.3.3. The results from AC impedance spectroscopy allow us to adopt the procedure described in section 2.3.3 to derive the band bending $e\Delta Vs$ and electron affinity change $\Delta\chi$ separately.

5.3.1 Influence of H_2O exposure

Figure 5.5 shows the variations of CPD and DC resistance with humidity, which lead to the variations of $\Delta\Phi$, $e\Delta V_s$, and $\Delta\chi$ with humidity as shown in Figure 5.6.

The variation of $\Delta\chi$ with humidity at 1,000ppm CO_2 was much smaller than that at 0 ppm CO_2 and almost zero.

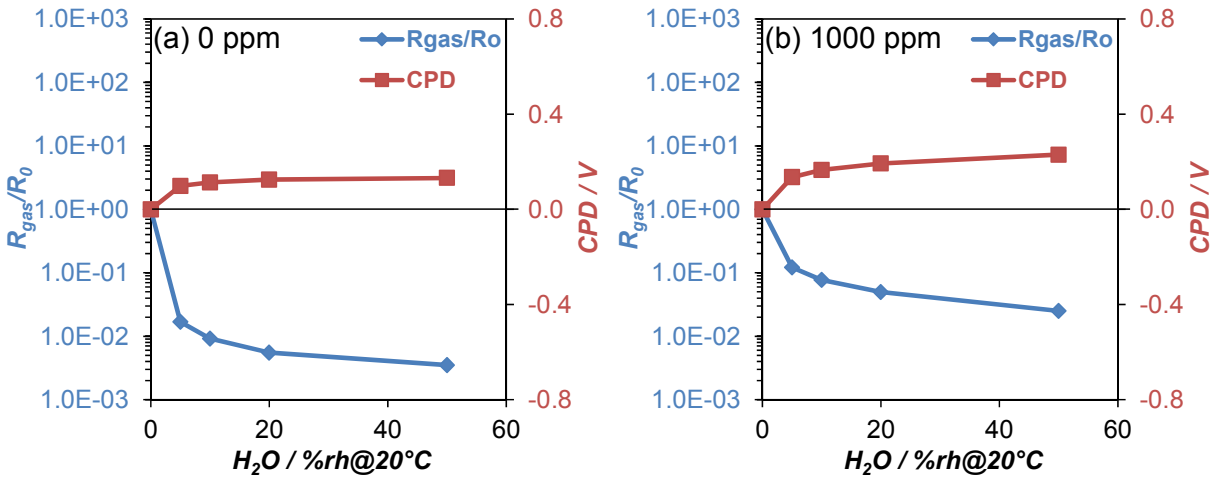

Figure 5.5 Variations of CPD and DC resistance with CO_2 concentration.

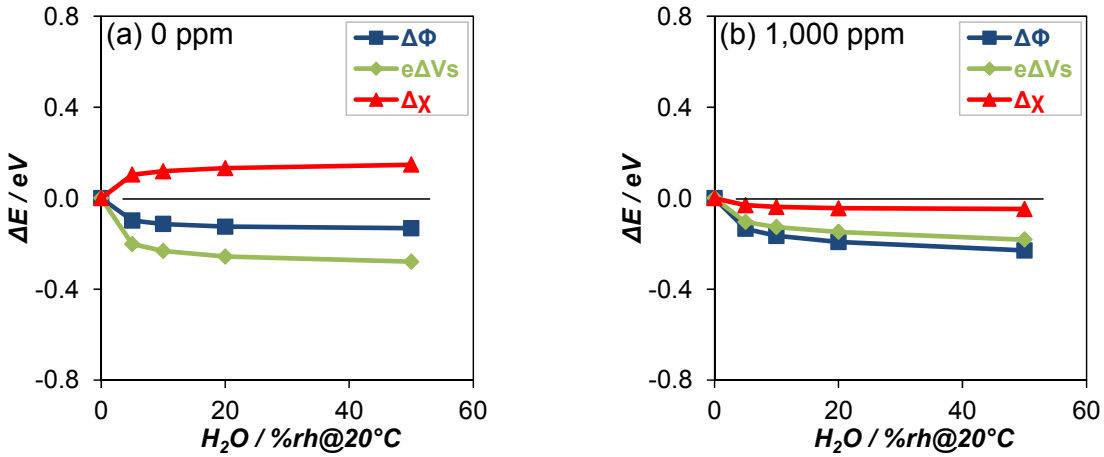

Figure 5.6 Variations of $\Delta\Phi$, $e\Delta V_s$, and $\Delta\chi$ with H_2O concentration.

5.3.2 Influence of CO_2 exposure

Figure 5.7 and Figure 5.8 show the variations of CPD and DC resistance with CO_2 concentration, and the variations of $\Delta\Phi$, $e\Delta V_s$, and $\Delta\chi$ with CO_2 concentration respectively.

The variation of DC resistance with CO_2 concentration at 0 % r.h. was smaller than those at other humidity conditions, and then CO_2 dependency of $\Delta\chi$ in dry condition was higher than that in wet condition. The variations of $\Delta\chi$ with CO_2 concentration in wet three conditions were almost the same.

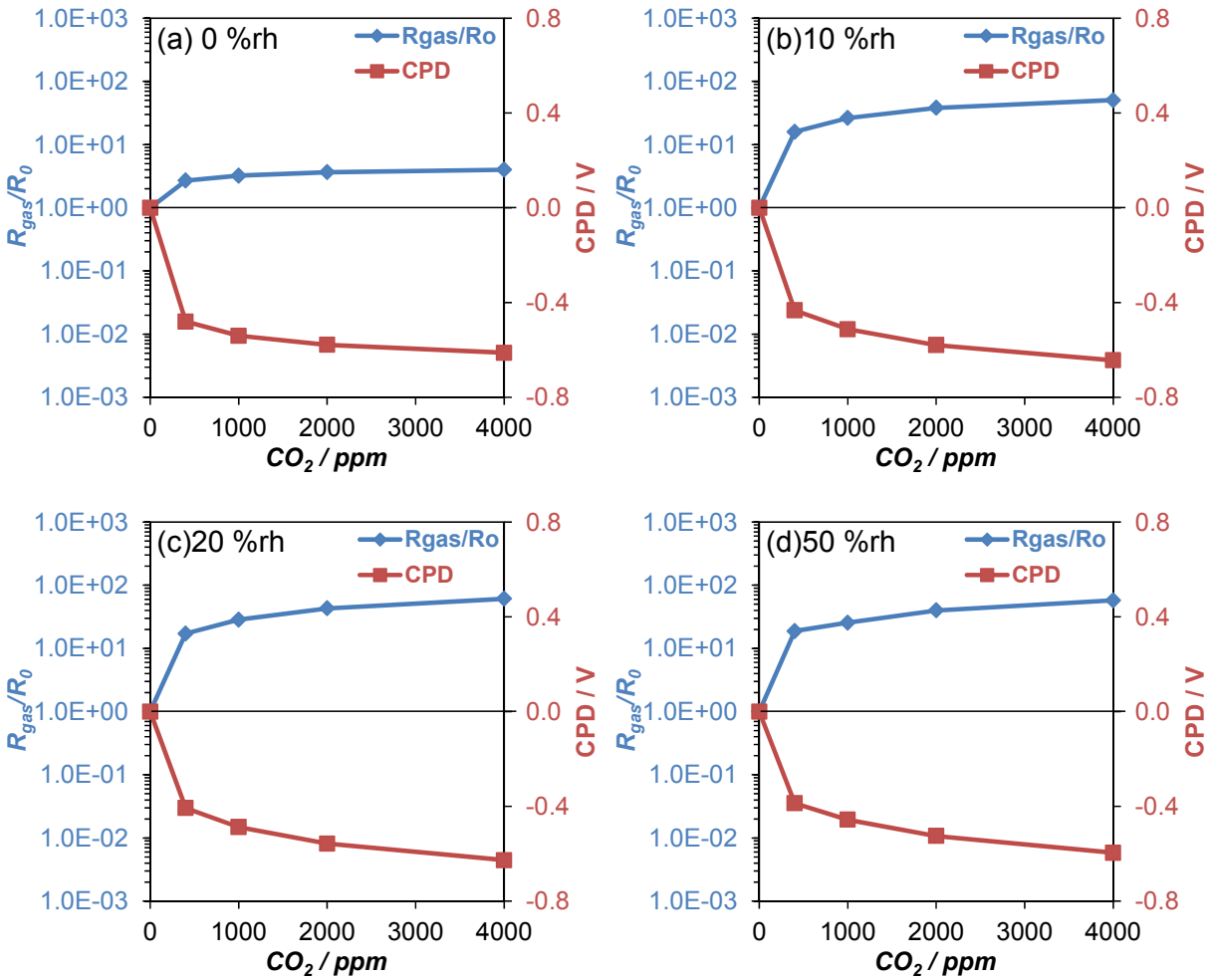

Figure 5.7 Variations of CPD and DC resistance with CO_2 concentration.

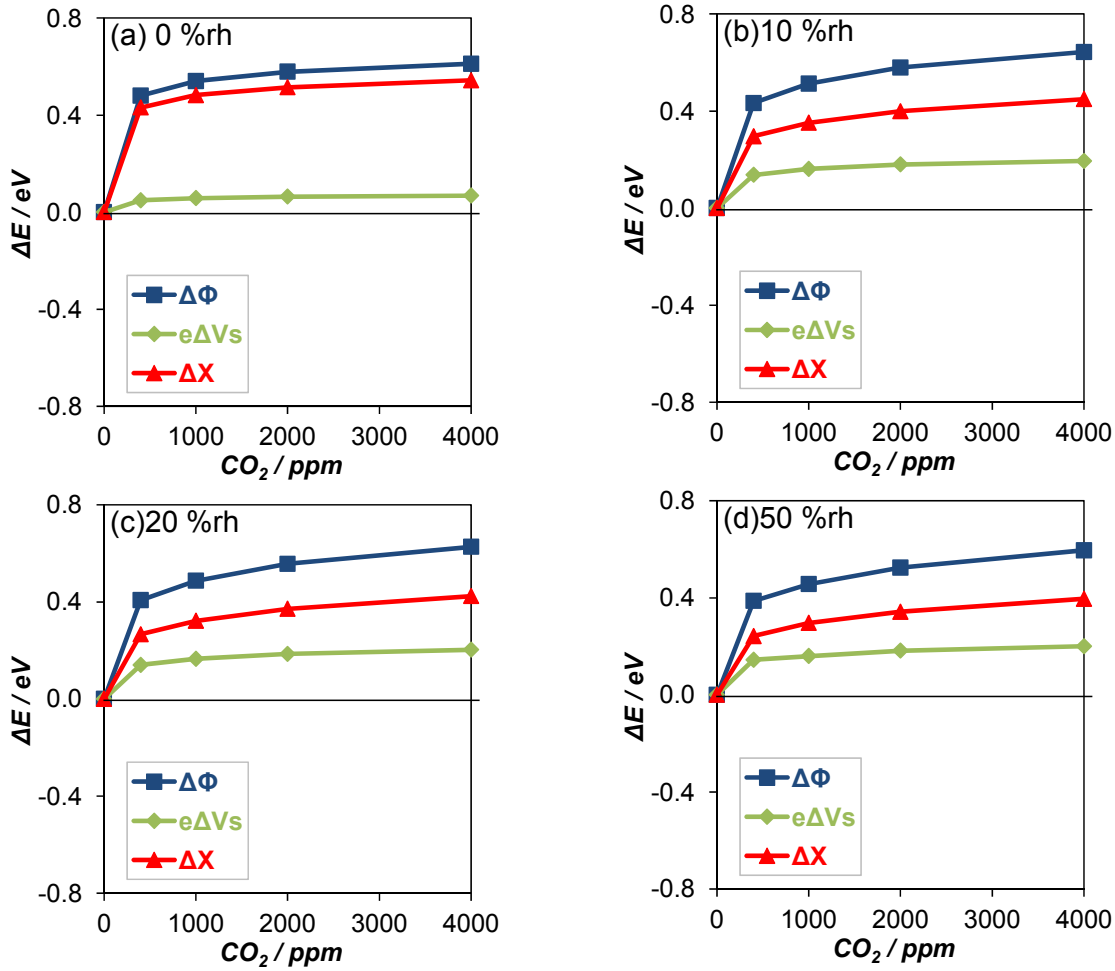

Figure 5.8 Variations of $\Delta\Phi$, $e\Delta V_s$, and $\Delta\chi$ with CO_2 concentration.

5.3.3 Comparison among the three gas exposure conditions

Influence of CO_2 exposure on $\Delta\chi$ is much larger than that of H_2O, and CO_2 dependency of $\Delta\chi$ in dry condition was higher than that in wet condition. The question is what causes the change in χ, depending on the atmospheric conditions. Electron affinity χ is basically related to the dipoles from surface adsorbate species, which will be identified in section 5.5.

5.4 Operando XRD

XRD and DC resistance of hexagonal $La_2O_2CO_3$ based sensor were measured simultaneously under the operating conditions as described in section 2.3.1. In addition, those of Gd_2O_3 based sensor, which was the most sensitive to CO_2 among the rare-earth oxides, were also measured in the same manner as hexagonal $La_2O_2CO_3$.

5.4.1 Time chart of gas flow and DC resistance

Figure 5.9 shows the time chart of gas flow and the corresponding DC resistance changes of the sensors. The DC resistance change was normalized by the resistance at time point 1.0 hour for each sensor. The carrier gas was clean dry air without CO_2 throughout the experiment, therefore there was a clean dry air flow between time point 0 and 1 hour. The resistances of both sensors decreased with increasing humidity, and increased with increasing CO_2 concentration. The change in resistance of hexagonal $La_2O_2CO_3$ was larger than that of Gd_2O_3.

5.4.2 XRD patterns

Figure 5.10 and Figure 5.11 show the XRD patterns for hexagonal $La_2O_2CO_3$ and Gd_2O_3 based sensors respectively. The patterns in Figure 5.10 and Figure 5.11 were assignable to $La_2O_2CO_3$ (hexagonal), Gd_2O_3 (cubic), and Al_2O_3 (corundum) owing to the substrate, and exhibited no change in terms of formation of new peaks and the position shifts, indicating that there was no change in the grain bulk, such as the transformation and the change in lattice parameter.

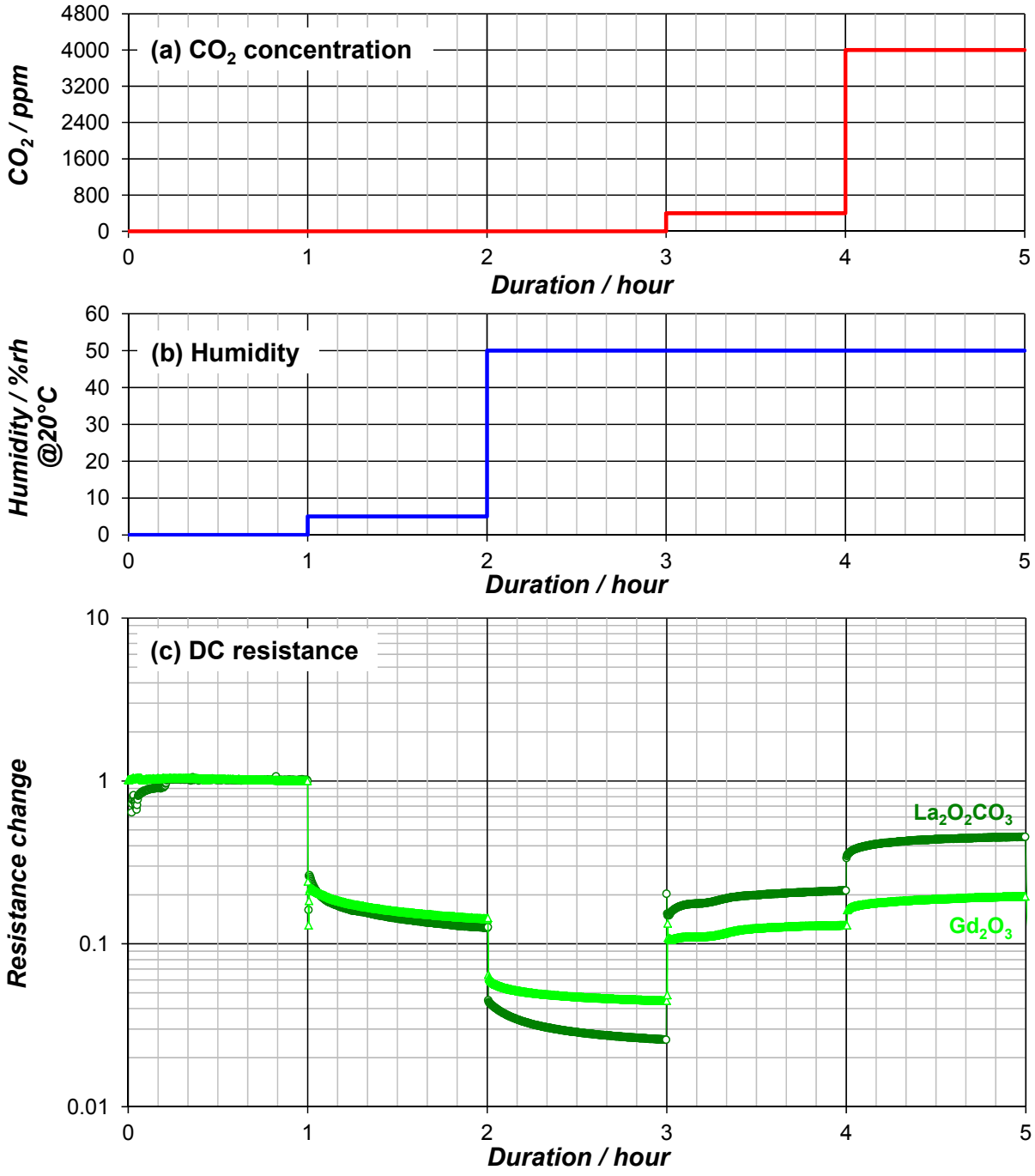

Figure 5.9 Time chart of gas flow and DC resistance.

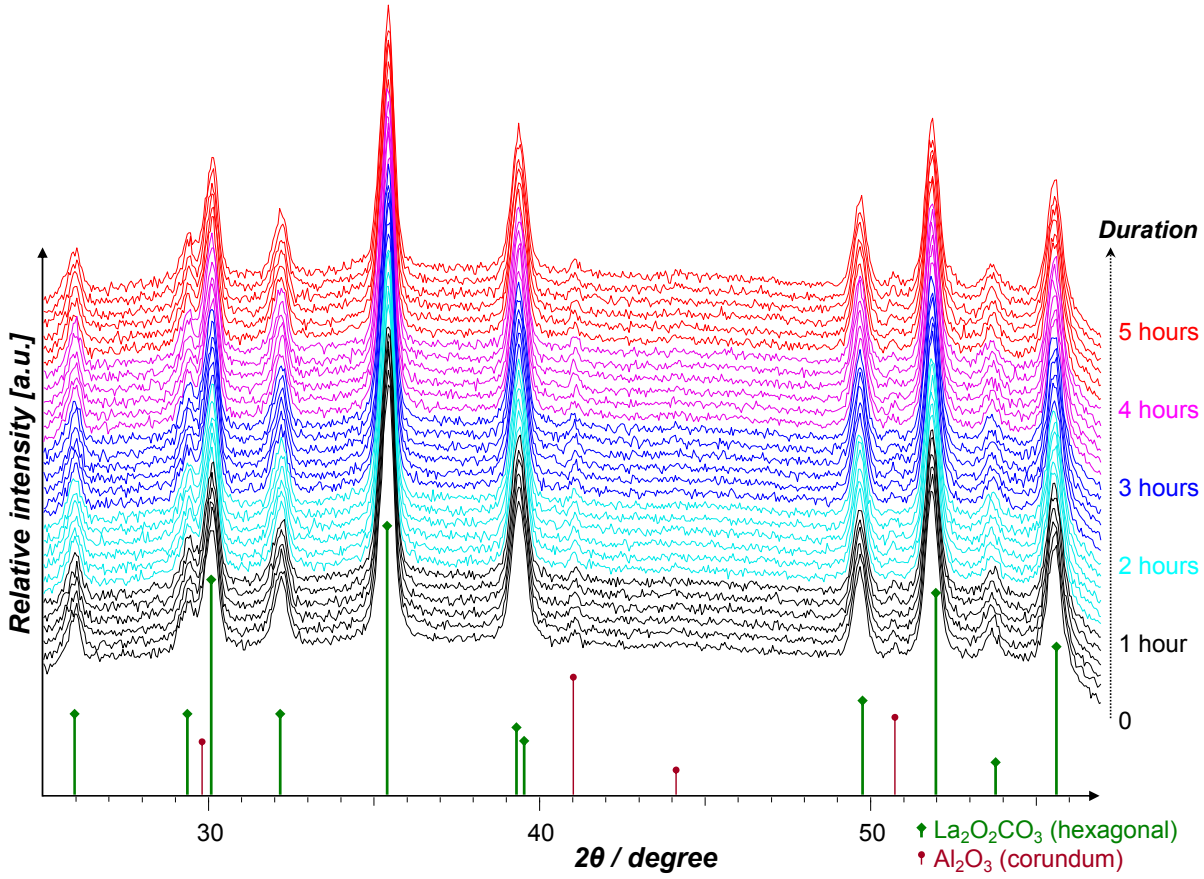

Figure 5.10 XRD patterns for hexagonal $La_2O_2CO_3$ based sensor.

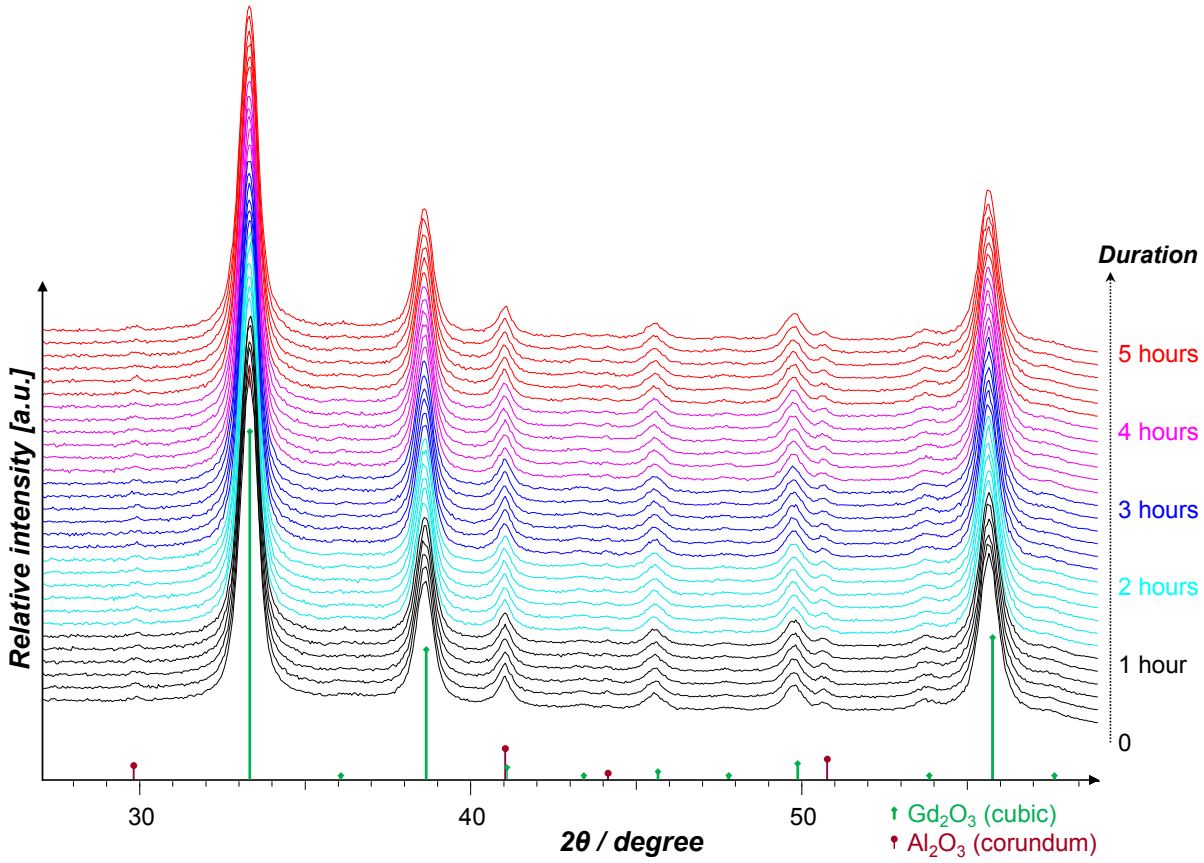

Figure 5.11 XRD patterns for Gd_2O_3 based sensor.

5.5 Operando DRIFTS

DRIFTS and DC resistance of hexagonal $La_2O_2CO_3$ based sensor and the rare-earth oxides (CeO_2, Nd_2O_3, Sm_2O_3, Gd_2O_3, Dy_2O_3, Er_2O_3, and Yb_2O_3) were measured simultaneously under the operating conditions as described in section 2.3.4.

5.5.1 Influence of CO_2 and H_2O exposure on hexagonal $La_2O_2CO_3$

Three kinds of experiments were performed using a hexagonal $La_2O_2CO_3$ based sensor at the operating temperature of 300 °C, in only humidity, only CO_2, and in both conditions. In the first experiment, humidity was changed stepwise from 0 to 2% and then, to 10% (Figure 5.12 (a)). In the second experiment, CO_2 concentration was changed stepwise from 0 to 400ppm, and then to 2000ppm (Figure 5.12 (b)). In the third experiment, humidity was maintained constant at 10%, and CO_2 concentration was changed stepwise from 0 to 400ppm and to 2000ppm (Figure 5.12 (c)).

5.5.1.1 Time variation of DC resistance and DRIFTS

Figure 5.12 shows the time variation of DC resistance. The sensor resistance decreased with increasing humidity, and increased with increasing CO_2 concentration.

Figure 5.13, Figure 5.15, Figure 5.17 show the single channel spectra for H_2O exposure, CO_2 exposure in dry condition, and CO_2 exposure in wet condition respectively. Figure 5.14, Figure 5.16, Figure 5.18 show the time variations of absorbance spectrum for H_2O exposure, CO_2 exposure in dry condition, and CO_2

exposure in wet condition respectively. Every reference spectrum was measured just before time point 0.

To compare between the time variation of DC resistance and those of absorbance spectra, these peaks or dips changed corresponding to the time variation of sensor resistance. The DC resistance in Figure 5.12 (a) decreased rapidly just after H_2O exposure and levelled off within 1 hour, while peak A, B, E, and H increased and dip D, F, G, and I in Figure 5.14 decreased rapidly just after H_2O exposure and levelled off within 1 hour. The correlation can also be seen in the case of CO_2 exposure in dry and wet conditions.

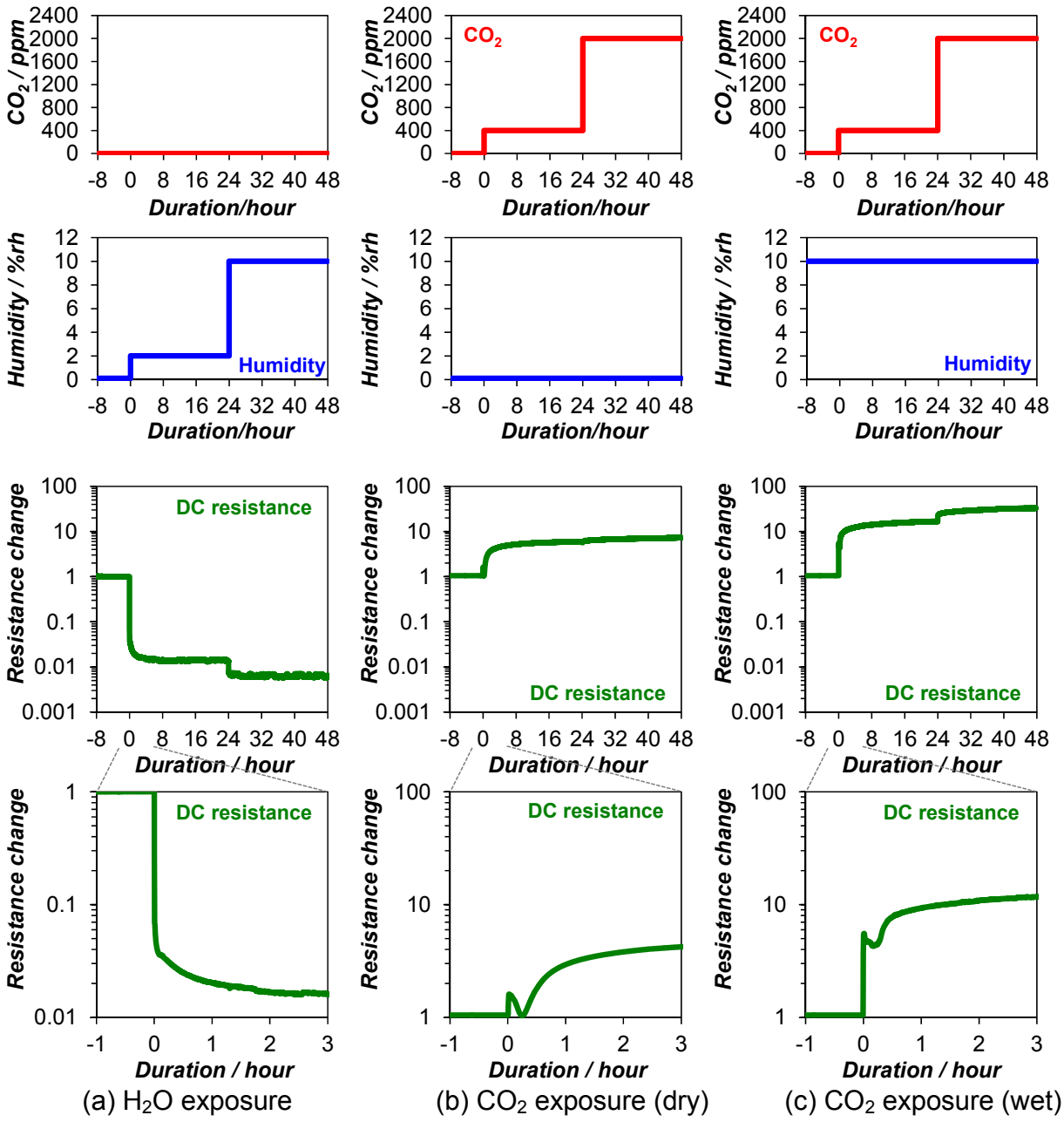

Figure 5.12 Time variations of gas flow and DC resistance.

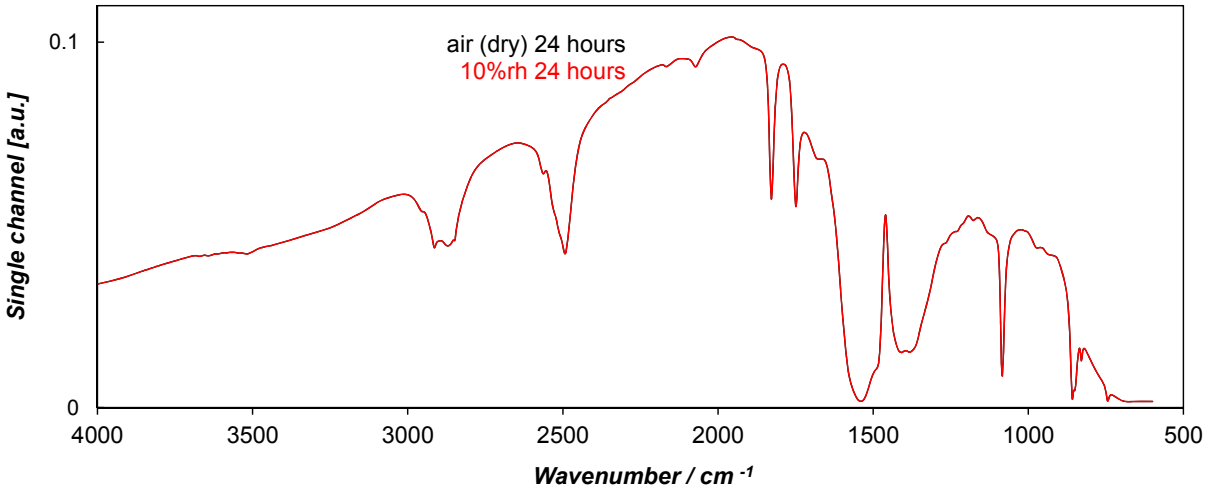

Figure 5.13 Single channel spectra in dry and humid air.
[H_2O exposure]

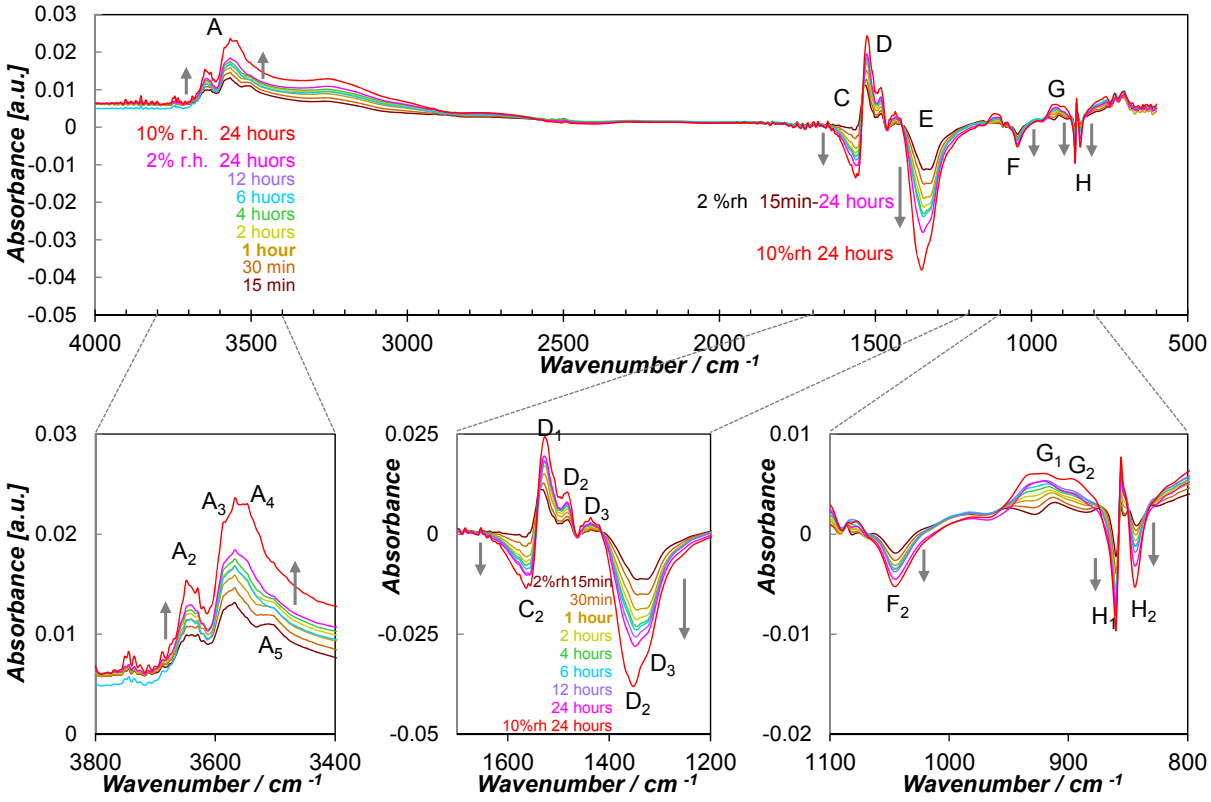

Figure 5.14 Time variations of absorbance spectra in dry and humid air.
[H_2O exposure]

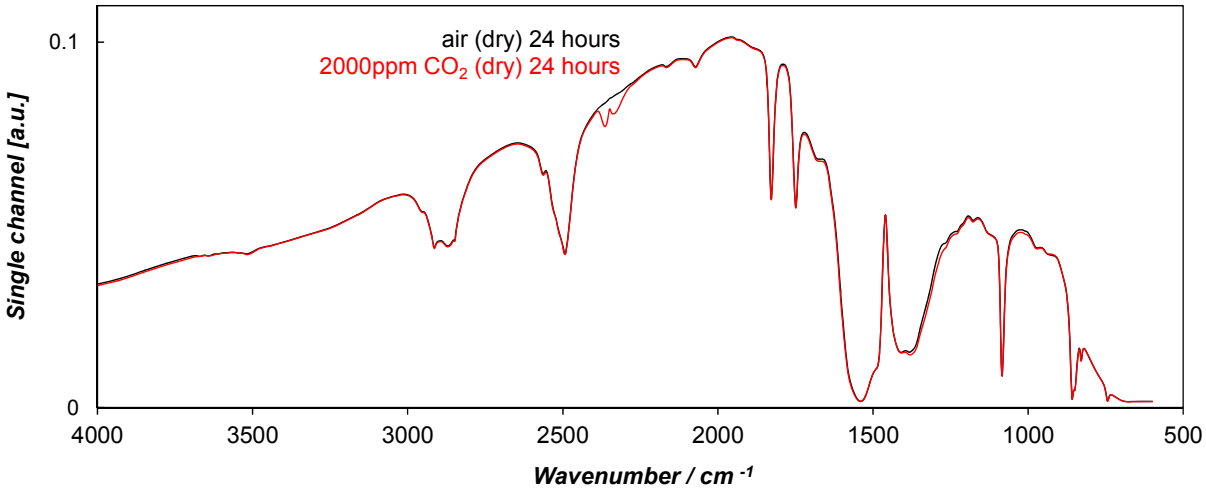

Figure 5.15 Single channel spectra at 0 and 2000ppm CO_2 in dry air.
[CO_2 exposure (dry)]

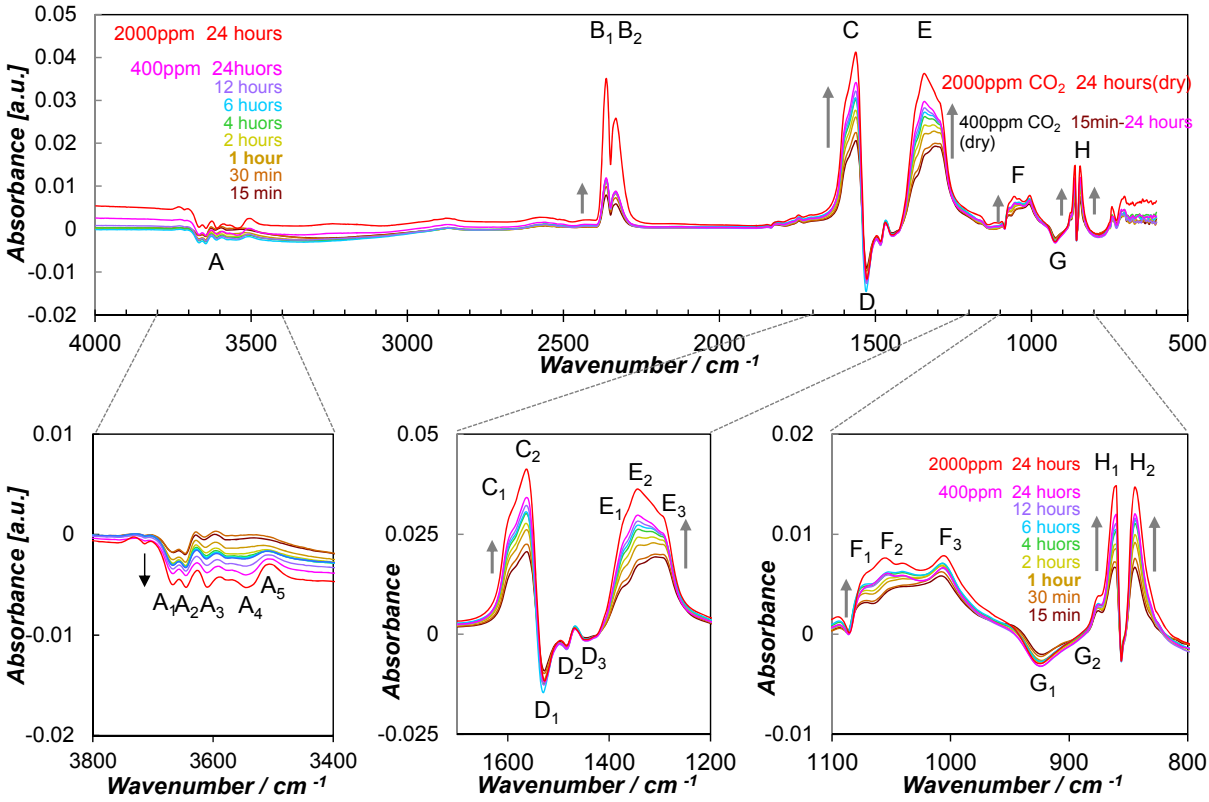

Figure 5.16 Time variations of absorbance spectra at 0 and 2000ppm CO_2 in dry air.
[CO_2 exposure (dry)]

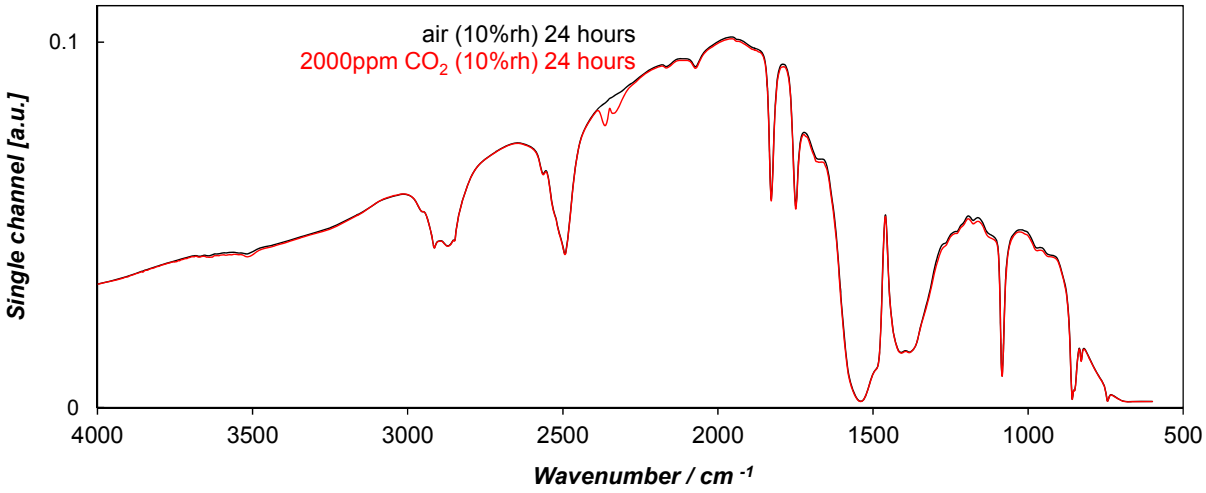

Figure 5.17 Single channel spectra at 0 and 2000ppm CO_2 in humid air.
[CO_2 exposure (wet)]

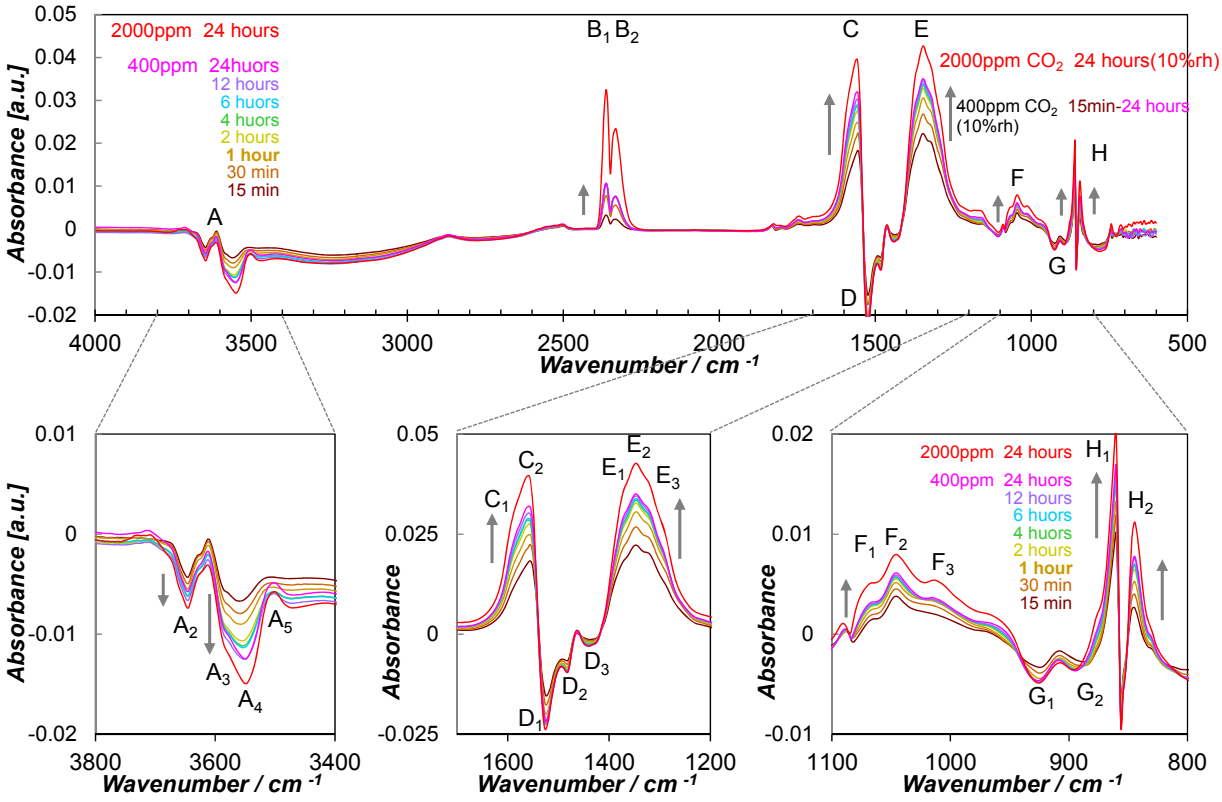

Figure 5.18 Time variations of absorbance spectra at 0 and 2000ppm CO_2 in humid air.
[CO_2 exposure (wet)]

5.5.1.2 Comparison among the three gas exposure conditions

The absorbance spectra for three gas exposure conditions are summarized in Figure 5.19 and Table 5.2. All peaks and dips are listed in there. The peaks can be categorized into three groups except for peak A_5. In the first group including peak A, D and G, the peaks increased with H_2O exposure and decreased with CO_2 exposure. In the second group including peak E, F and H, the peaks increased with CO_2 exposure and decreased with H_2O exposure. In the third group including peak B, the peaks increased with CO_2 exposure and remained unchanged with H_2O exposure. There seems to be a competitive relation between the first group and the second group.

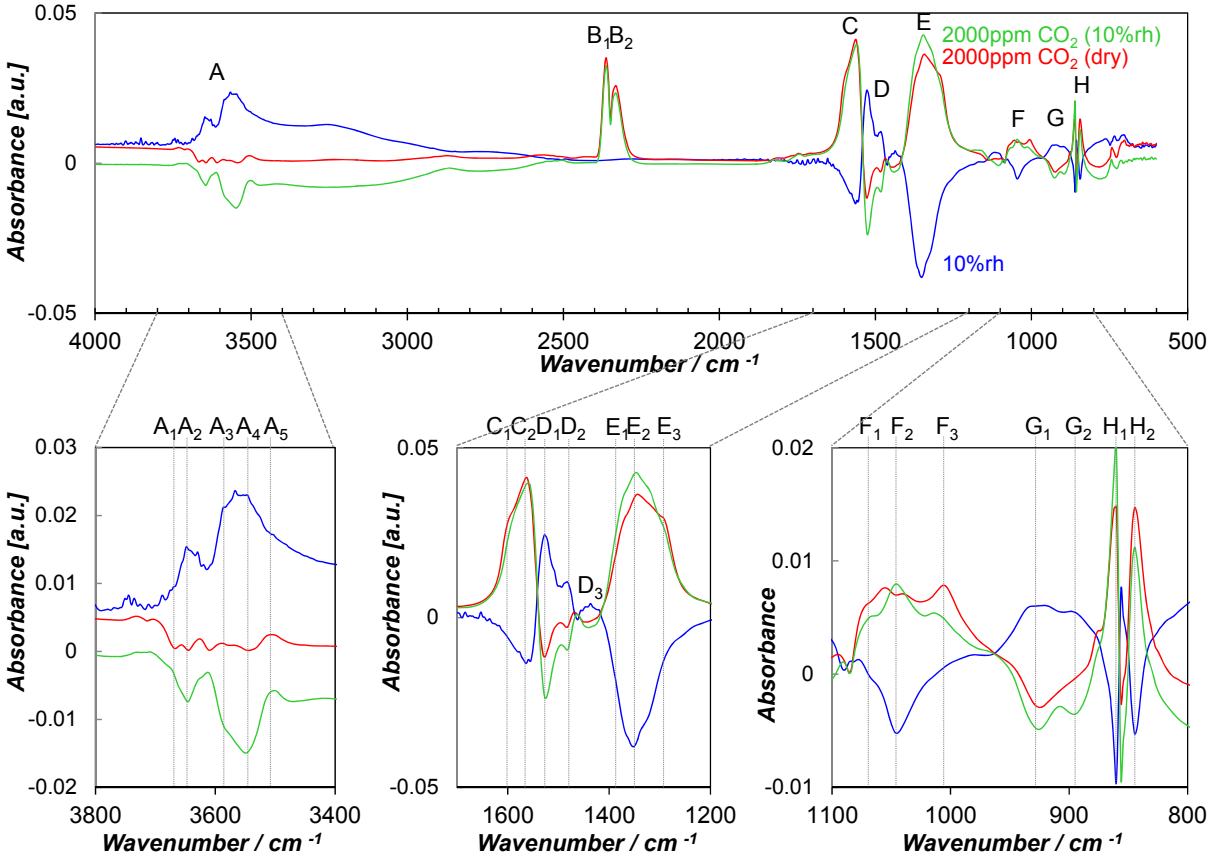

Figure 5.19 Comparison of absorbance spectra for three gas exposure conditions. (at time point 48 hour in each experiment)

Table 5.2 Summary of absorbance spectra for three gas exposure conditions. (Peak ↑ or dip ↓ positions and their relative strength.)

Peak or dip	H_2O exposure		CO_2 exposure (dry)		CO_2 exposure (wet)	
A_1			3668	↓		
A_2	3648	↑↑↑	3645	↓	3646	↓↓↓
A_3	3587	↑↑↑	3610	↓	3587	↓↓↓
A_4	3546	↑↑↑	3545	↓	3549	↓↓↓
A_5	3503	↑	3507	↑	3502	↑
B_1			2363	↑↑↑	2363	↑↑↑
B_2			2332	↑↑↑	2332	↑↑↑
C_1			1599	↑↑↑	1599	↑↑↑
C_2	1564	↓↓↓	1564	↑↑↑	1560	↑↑↑
D_1	1527	↑↑↑	1527	↓↓	1527	↓↓↓
D_2	1483	↑↑	1483	↓	1483	↓↓
D_3	1436	↑	1445	↓	1441	↓
E_1	.		1376	↑↑↑	1376	↑↑↑
E_2	1352	↓↓↓	1344	↑↑↑	1343	↑↑↑
E_3	1322	↓↓↓	1291	↑↑↑	1291	↑↑↑
F_1			1056	↑↑	1069	↑↑
F_2	1046	↓↓	1039	↑↑	1046	↑↑
F_3			1006	↑↑	1010	↑↑
G_1	923	↑↑	925	↓↓	925	↓↓
G_2	896	↑↑			896	↓↓
H_1	860	↓↓	860	↑↑	860	↑↑
H_2	844	↓↓	844	↑↑	844	↑↑

unit : cm^{-1}

The number of arrows represents the relative strength;
strong: ↑↑↑ > medium: ↑↑ > weak: ↑.

5.5.2 Isotopic gas exchange experiment and peak assignment for hexagonal $La_2O_2CO_3$

In order to eliminate the artifacts and assign the peaks, isotopic gas exchange experiments were performed using $^{13}CO_2$ and D_2O. The gas flow was shown in Figure 5.20 (a), (b). The carrier gas was clean dry air without CO_2. The operating temperature was 300 °C.

Figure 5.20 (c) shows the time variation of DC resistance indicating that the DC resistance decreased with increasing humidity and increased with increasing CO_2 concentration as the same as the preceding experiment, and was not influenced by the isotopic gas exchanges even though there was a small dip at time point 18 hours because of the lag time for changing the gas.

Figure 5.21 shows the comparison of absorbance spectra for three gas exposure conditions, (1) 400 ppm CO_2 in dry air, (2) 10 % r.h., (3) 400ppm in 10 % r.h. air. The spectra were measured just before time point 6 hours, 12 hours, and 18 hours, respectively. The reference spectrum for (1) and (2) was measured just before time point 0. The reference spectrum for (3) was measured just before time point 12 hours. The spectra were basically the same as Figure 5.19 in terms of peak pattern and position.

Figure 5.22 shows the absorbance spectrum for the condition (3) and difference spectra for isotopic gas exchanges, (4) $^{12}CO_2 \rightarrow {}^{13}CO_2$ and (5) $H_2O \rightarrow D_2O$. The difference spectra were derived from the following equations (5.1) and (5.2).

$$Difference\ (4) = -\log\left(\frac{SC\ {}^{13}CO_2}{SC\ {}^{12}CO_2}\right) \qquad (5.1)$$

$$Difference\ (5) = -\log\left(\frac{SC\ H_2O}{SC\ D_2O}\right) \qquad (5.2)$$

where every single channel spectra (*SC*) was measured during the last 15 minutes of each exposure. With respect to the isotopic gas exchange of CO_2, peak B, C, E, F, and H were shifted to a lower wavenumber adjacent to the initial position, and peak A, D, and G remained unchanged. With respect to the isotopic gas exchange of water, only peak A was shifted to the lower wavenumber around 2,600 cm^{-1}, and there were small peaks at the position of E and H, which are thought to be the continuous shifts owing to the isotopic gas exchange of CO_2. It is thought that peak D and G were artifacts because there was no change during the isotopic gas exchange.

The results of isotopic gas exchange experiment are summarized in Table 5.3, where the wavenumbers of all peaks and dips including shoulders, and the shift factor defined as the ratio of the wave numbers between before and after the isotopic exchange, are shown.

According to [50][51][52][53], the presence of isolated hydroxyl groups at the surface is indicated by the appearance of sharp bands between 3750 and 3450 cm^{-1}, while bridged (interacting) hydroxyls cause broad bands between 3600 and 2500 cm^{-1}. The shift factor of A_1 through A_4 were 0.733 -0.735, which are close to the theoretical value of O-H vibration, 0.728 [54][55]. The shift of A_5 was not clear. From these results, peak A is assignable to hydroxyl groups. The further research is needed to assign them in more detail so as to distinguish among the isolated, rooted, and interacting species.

Peak B is assignable to gaseous CO_2 according to [56][57]. The results that a peak emerged only during CO_2 exposure and the shift factor of B_1 and B_2 was the same as theoretical value of C=O vibration, 0.972 [54] [55], are supportable.

Regarding peak C, E, F, and H, the single channel spectra, the absorbance spectra, the difference spectra for the isotopic gas exchange of CO_2, and carbonate bands from

the literature [55][58][59][60][61] are shown in Figure 5.23. Schematic representation of different carbonate related species is shown in Figure 5.24. It is reasonable to assume that these peaks are assignable to a mixture of carbonate species with several vibration modes, most probably, unidentate carbonate, bidentate carbonate, and bridged carbonate. The shifts of E_2, F_1, F_2, and F_3 were small. It may be owing to the symmetry of the vibration as reported in [58].

In addition, it is noticeable that there were no peaks shifted twice with the both isotopic gas exchanges of CO_2 and water, indicating that there was no formation of such species including both OH and CO as bicarbonates.

5.5.3 Comparison with work function measurement

To compare with $\Delta\chi$ from the work function measurements, the absorbance spectra and the variations of electron affinity $\Delta\chi$ for three gas exposure conditions are summarized in Table 5.4 and Figure 5.25. In the case of humidity exposure, hydroxyl groups increased and carbonate decreased, and the $\Delta\chi$ is small. In the case of CO_2 exposure in the dry condition, hydroxyl groups decreased slightly and carbonate increased, and the $\Delta\chi$ is large. In the case of CO_2 exposure in the wet condition, hydroxyl groups decreased and carbonate increased, and the $\Delta\chi$ is smaller than in the 2nd case. There seem to be a good correlation between the absorbance spectra and $\Delta\chi$, indicating that sum of the surface adsorbates are responsible for the change of the concentration of dipoles.

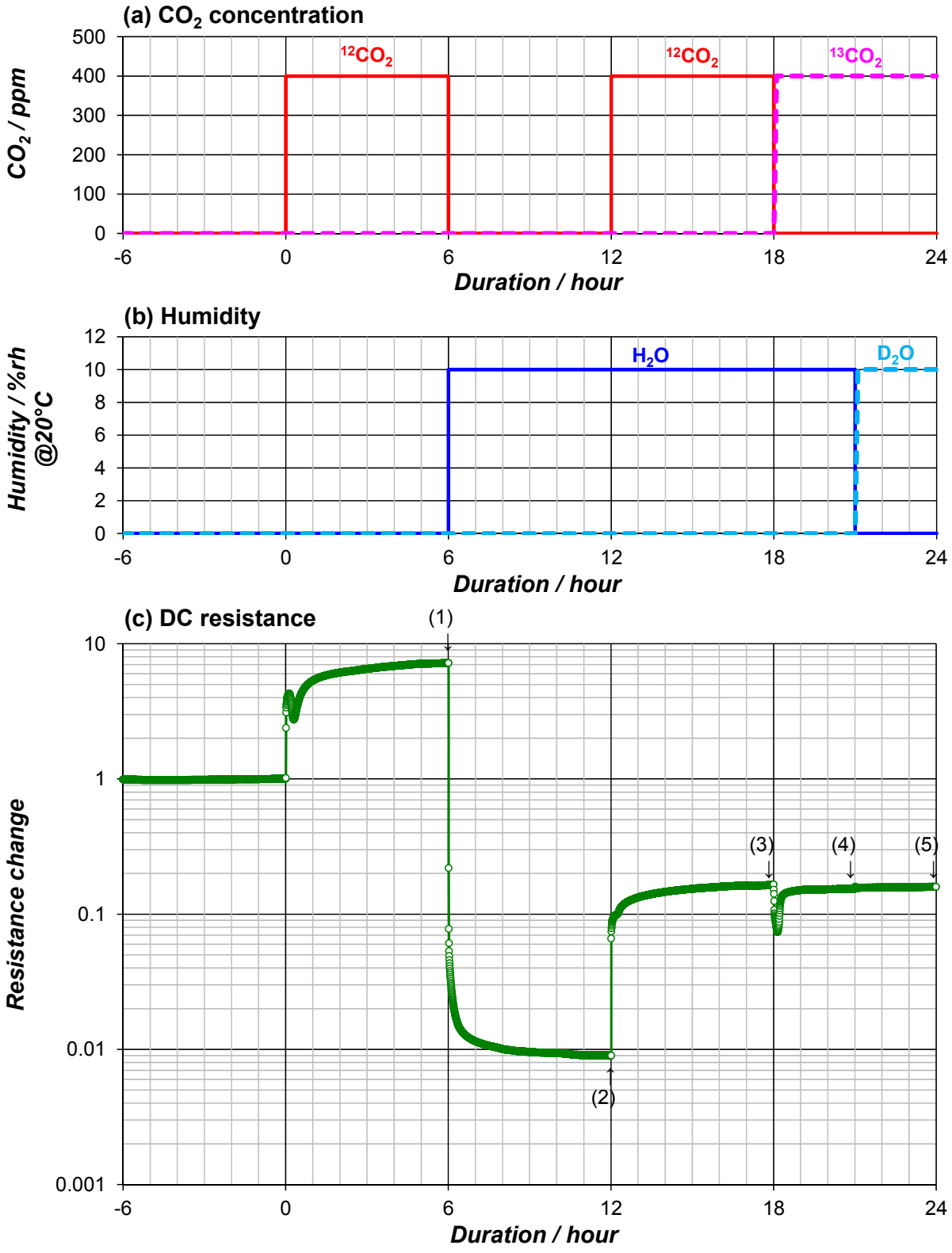

Figure 5.20 Time variations of gas flow and DC resistance.

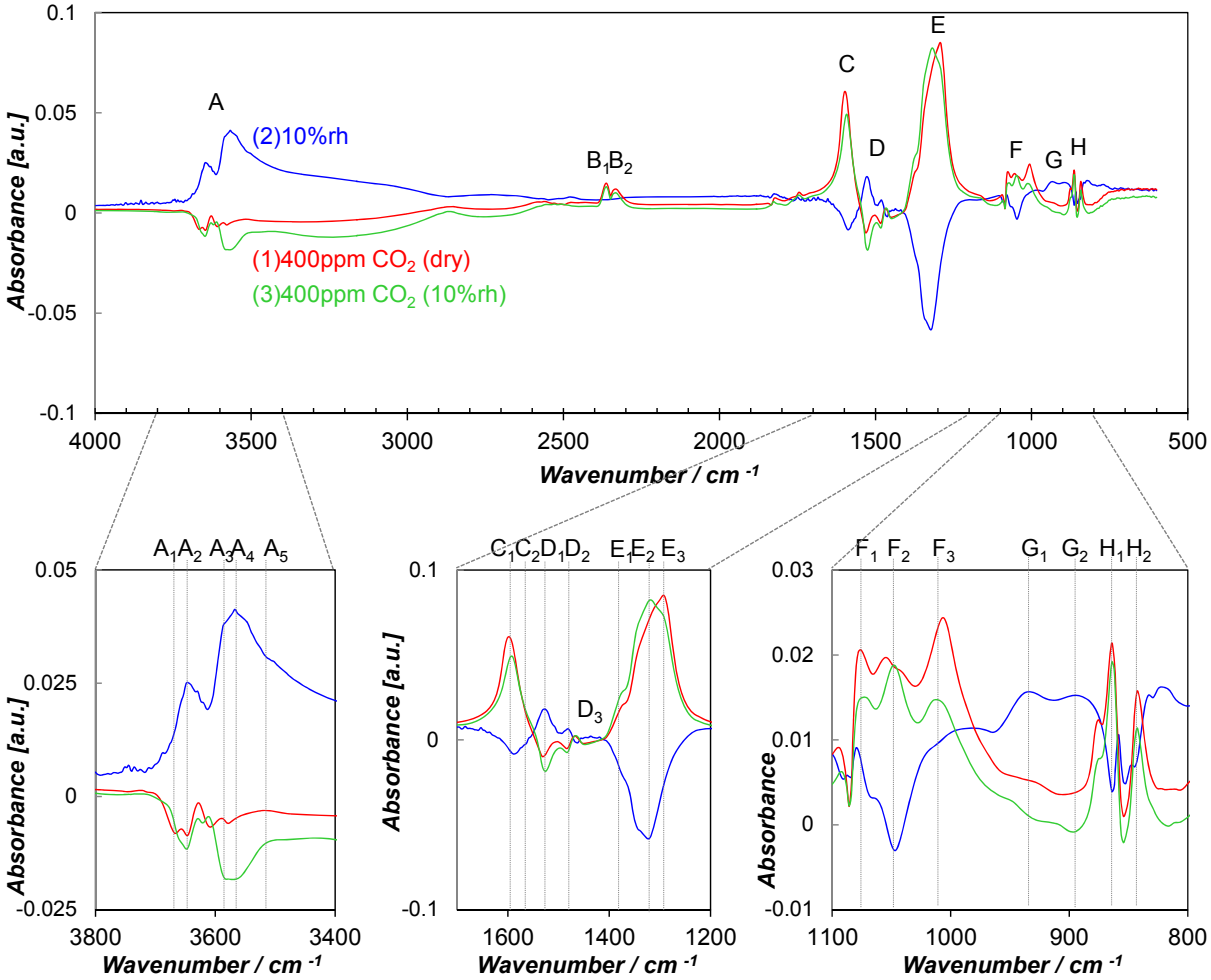

Figure 5.21 Comparison of absorbance spectra for three gas exposure conditions.

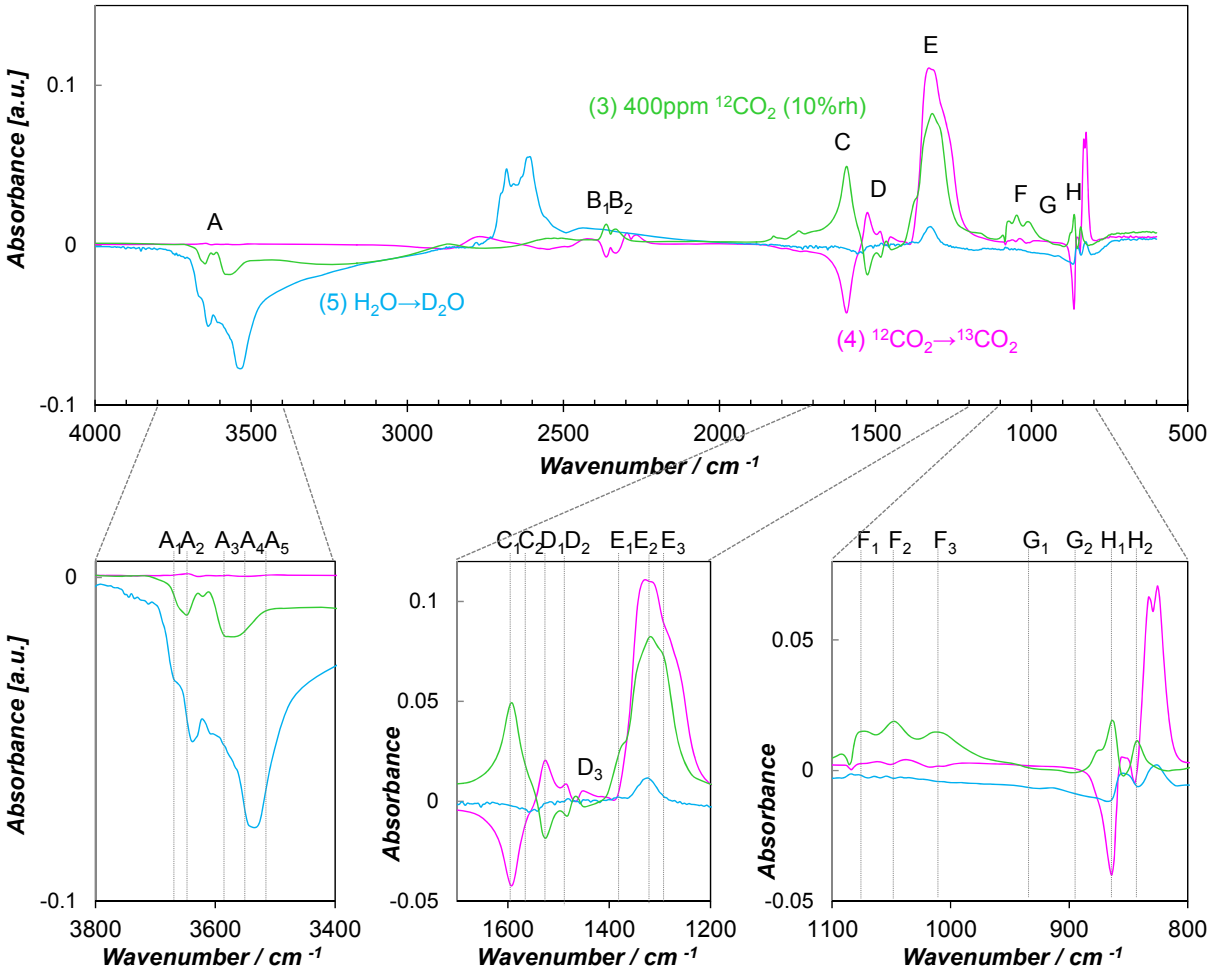

Figure 5.22 Difference spectra for isotopic gas exchanges.

Table 5.3 Summary of isotopic gas exchange experiment for $La_2O_2CO_3$.
(Peak ↑ or dip ↓ positions and their relative strength.)

Peak or dip	(1) 400ppm CO_2 (dry)		(2) 10 % r.h.		(3) 400ppm CO_2 (10 % r.h.)		(4) $^{12}CO_2 \rightarrow {}^{13}CO_2$		(5) $H_2O \rightarrow H_2O$		Assignment
								shift		shift	
A_1	3668	↓	3675	↑	3675	↓			2700	0.735	hydroxyl group
A_2	3647	↓	3647	↑↑	3647	↓↓			2682	0.735	
A_3	3610	↓	3585	↑↑↑	3585	↓↓↓			2636	0.735	
A_4	3578	↓	3567	↑↑↑	3567	↓↓↓			2615	0.733	
A_5	3507	↑	3505	↑	3505	↑					not clear
B_1	2363	↑↑↑			2363	↑↑↑	2296	0.972			gaseous CO_2
B_2	2332	↑↑↑			2332	↑↑↑	2267	0.972			
C_1	1598	↑↑↑	1588	↓↓	1593	↑↑↑	1526	0.958			carbonate
C_2	1560	↑↑	1560	↓↓	1560	↑↑	1485	0.952			
D_1	1531	↓↓	1528	↑↑	1526	↓↓					artifact
D_2	1483	↓	1481	↑	1483	↓					
D_3											
E_1	1376	↑↑	1375	↓↓	1376	↑↑	1332	0.968			carbonate
E_2	1322	↑↑↑	1322	↓↓↓	1318	↑↑↑	1313	0.996			
E_3	1292	↑↑↑			1292	↑↑↑	1261	0.976			
F_1	1076	↑↑	1066	↓↓	1076	↑↑	1062	0.987			
F_2	1055	↑↑	1047	↓↓	1047	↑↑	1038	0.991			
F_3	1006	↑↑	1011	↓↓	1010	↑↑	995	0.985			
G_1	935	↓↓	935	↑↑	935	↓↓					artifact
G_2	895	↓↓	895	↑↑	895	↓↓					
H_1	864	↑↑	864	↓↓	864	↑↑	833	0.964			carbonate
H_2	842	↑↑	842	↓↓	842	↑↑	825	0.980			

unit : cm^{-1}
The number of arrows represents the relative strength;
strong: ↑↑↑ > medium: ↑↑ > weak: ↑.

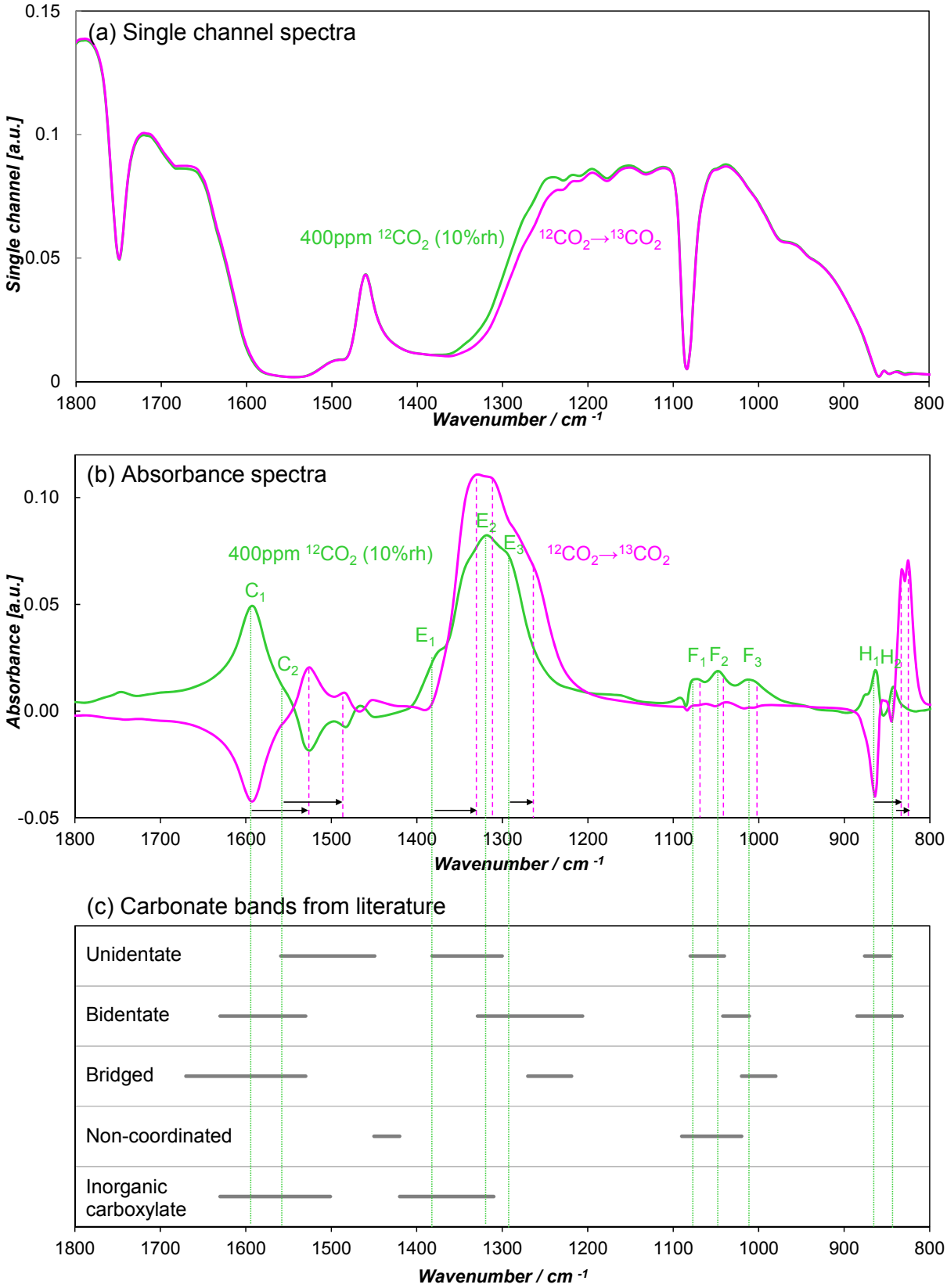

Figure 5.23 Assignment of peak C, E, F, and H.

Unidentate

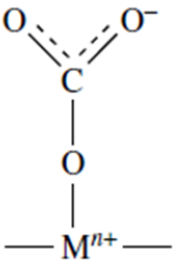

Bidentate

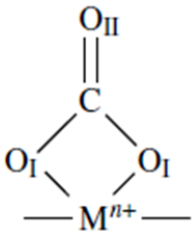

Bridged

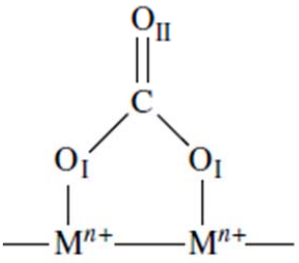

Non-coordinated

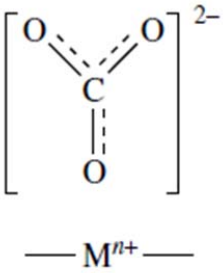

Carboxylate

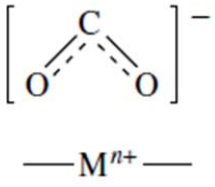

Figure 5.24 Schematic representation of different carbonate related species [55].

Table 5.4 Summary of absorbance spectra for three gas exposure conditions. (Peak ↑ or dip ↓ positions and their relative strength.)

(a)H_2O exposure 10 % r.h.		(b) CO_2 exposure in dry condition 400ppm CO_2		(c) CO_2 exposure in wet condition 10 % r.h. 400 ppm CO_2		assignment
3675	↑	3668	↓	3675	↓	hydroxyl group
3647	↑↑	3647	↓	3647	↓↓	
3585	↑↑↑	3610	↓	3585	↓↓↓	
3567	↑↑↑	3578	↓	3567	↓↓↓	
1588	↓↓	1598	↑↑↑	1593	↑↑↑	carbonate
1560	↓↓	1560	↑↑	1560	↑↑	
1375	↓↓	1376	↑↑	1376	↑↑	carbonate
1322	↓↓↓	1322	↑↑↑	1318	↑↑↑	
		1292	↑↑↑	1292	↑↑↑	
1066	↓↓	1076	↑↑	1076	↑↑	
1047	↓↓	1055	↑↑	1047	↑↑	
1011	↓↓	1006	↑↑	1010	↑↑	
864	↓↓	864	↑↑	864	↑↑	carbonate
842	↓↓	842	↑↑	842	↑↑	

unit : cm^{-1}

The number of arrows represents the relative strength;

strong: ↑↑↑ > medium: ↑↑ > weak: ↑.

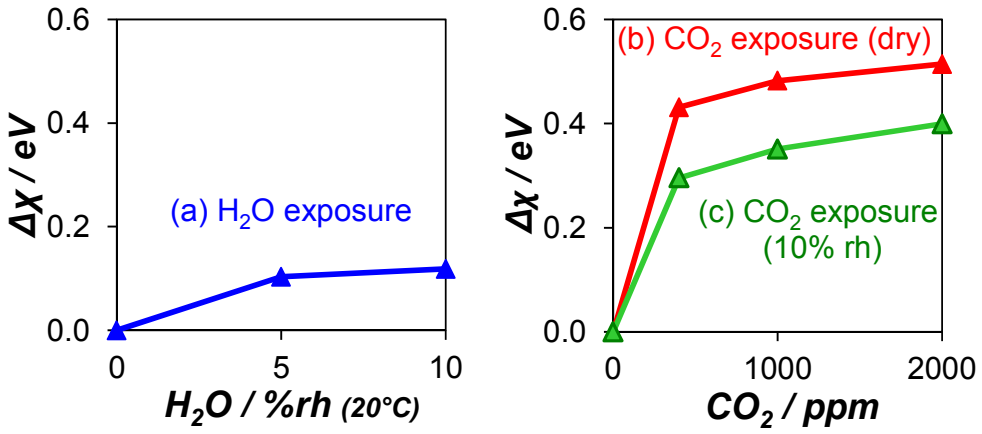

Figure 5.25 Variation of electron affinity $\Delta\chi$ for three gas exposure conditions.

5.5.4 DRIFTS for rare-earth oxides

DRIFTS's for rare-earth oxides, such as CeO_2, Nd_2O_3, Sm_2O_3, Gd_2O_3, Dy_2O_3, Er_2O_3, and Yb_2O_3, have been measured in the same manner presented in section 5.5.2. The absorbance spectra for three gas exposure conditions and the difference spectra for isotopic gas exchanges are shown in Figure 5.26 and Figure 5.27, with a comparison to hexagonal $La_2O_2CO_3$, which are identical to Figure 5.21 and Figure 5.22.

In Figure 5.26, the absorbance spectra for the rare-earth oxides were similar to those for hexagonal $La_2O_2CO_3$ and basically composed of 6 peaks, peak A due to hydroxyl groups, peak B due to gaseous CO_2, and peaks C through H due to carbonate species (unidentate or bidentate), where there seems to be competitive relations between the peak A and peaks C through H. It is thought that the formation of carbonates or hydroxyl groups on the surface is linked to the CO_2 sensing. The peaks C through H were simpler without any branches, which were found for hexagonal $La_2O_2CO_3$, indicating a single adsorbate specie. The peak pattern varied in the specific shape and position for the different the rare-earth elements. Especially for CeO_2, the peak patterns were different from the others to the extent that the peak A exhibited a sharp bump and the peak C and peak E were unified.

As shown in Figure 5.27, the difference spectra for the isotopic gas exchanges were also similar to those recorded for hexagonal $La_2O_2CO_3$ so that every peak A around 3,500 cm^{-1} was shifted to around 2,600 cm^{-1}, and every peak B through H were shifted to a lower wavenumber adjacent to the initial one, and every peak F exhibits very small or no shift.

As also observed for the sensor signal to CO_2, CeO_2 exhibited the most different spectral characteristics from the other oxides as mentioned above, which can lead to the

lower sensor signal. In the case of Nd_2O_3, the spectra were quite similar to the other oxides exhibiting a higher sensor signal so that the lower sensor signal of Nd_2O_3 cannot be explained by DRIFTS results.

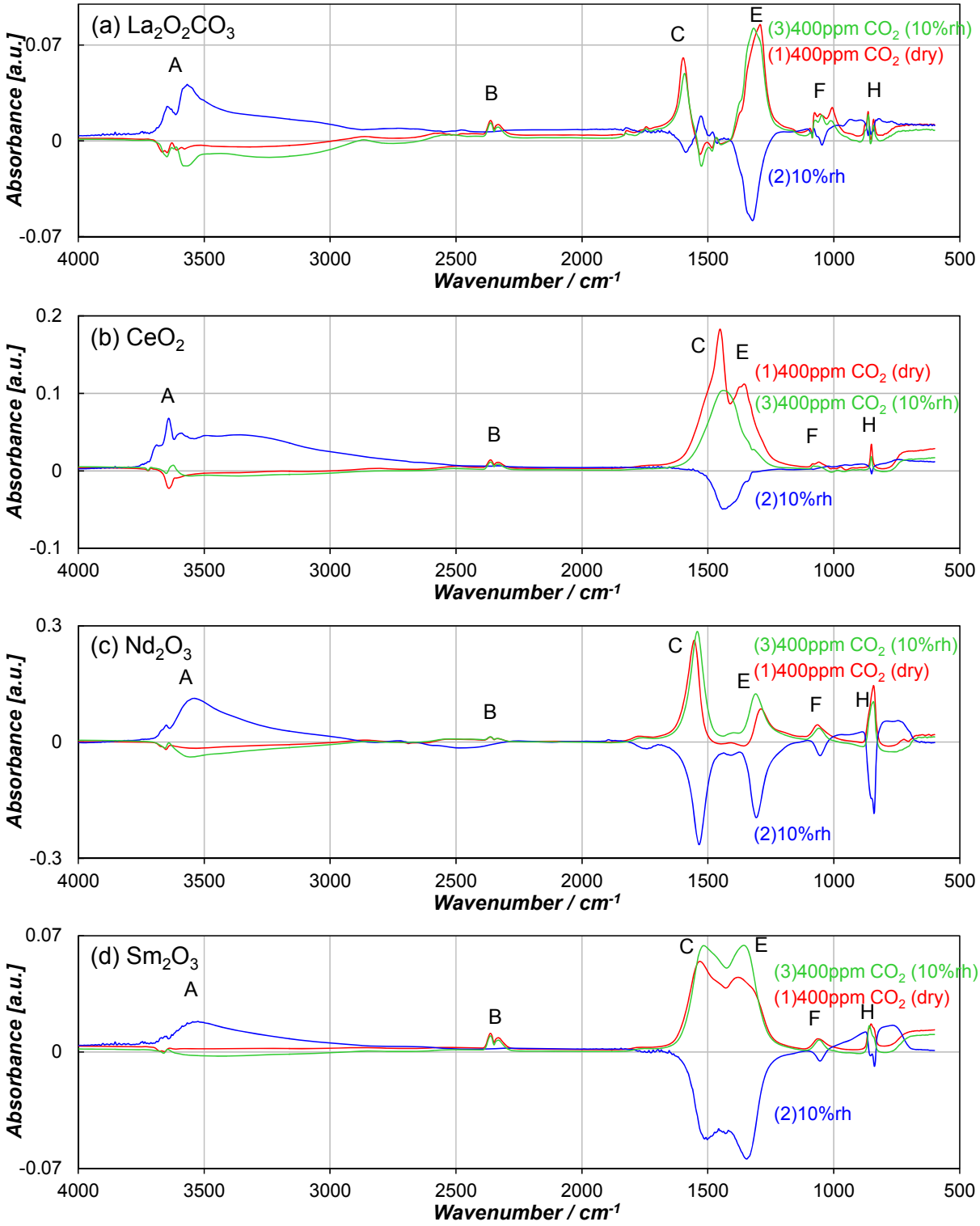

Figure 5.26.1 Absorbance spectra for three gas exposure conditions. (a)-(d)

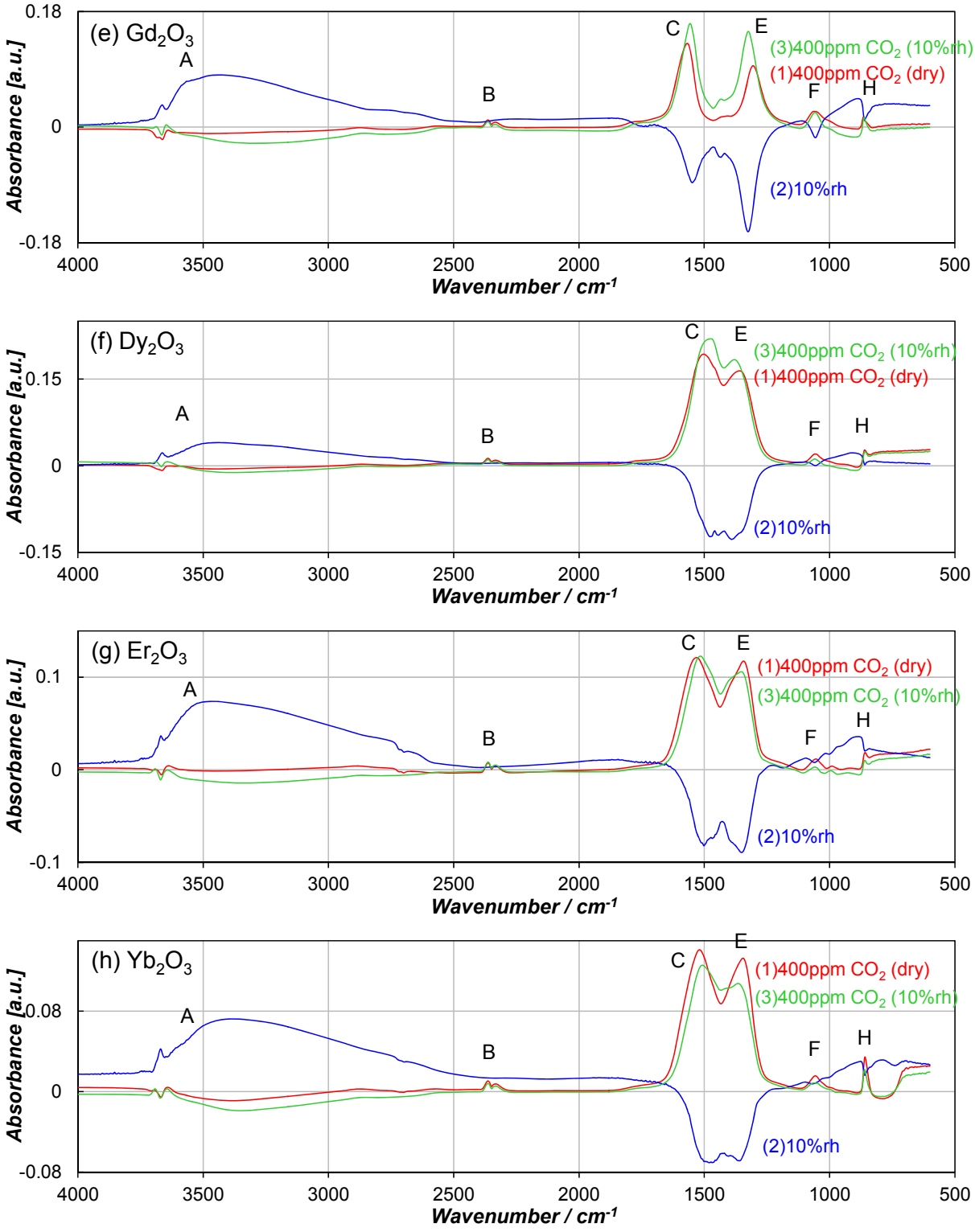

Figure 5.26.2 Absorbance spectra for three gas exposure conditions. (e)-(h)

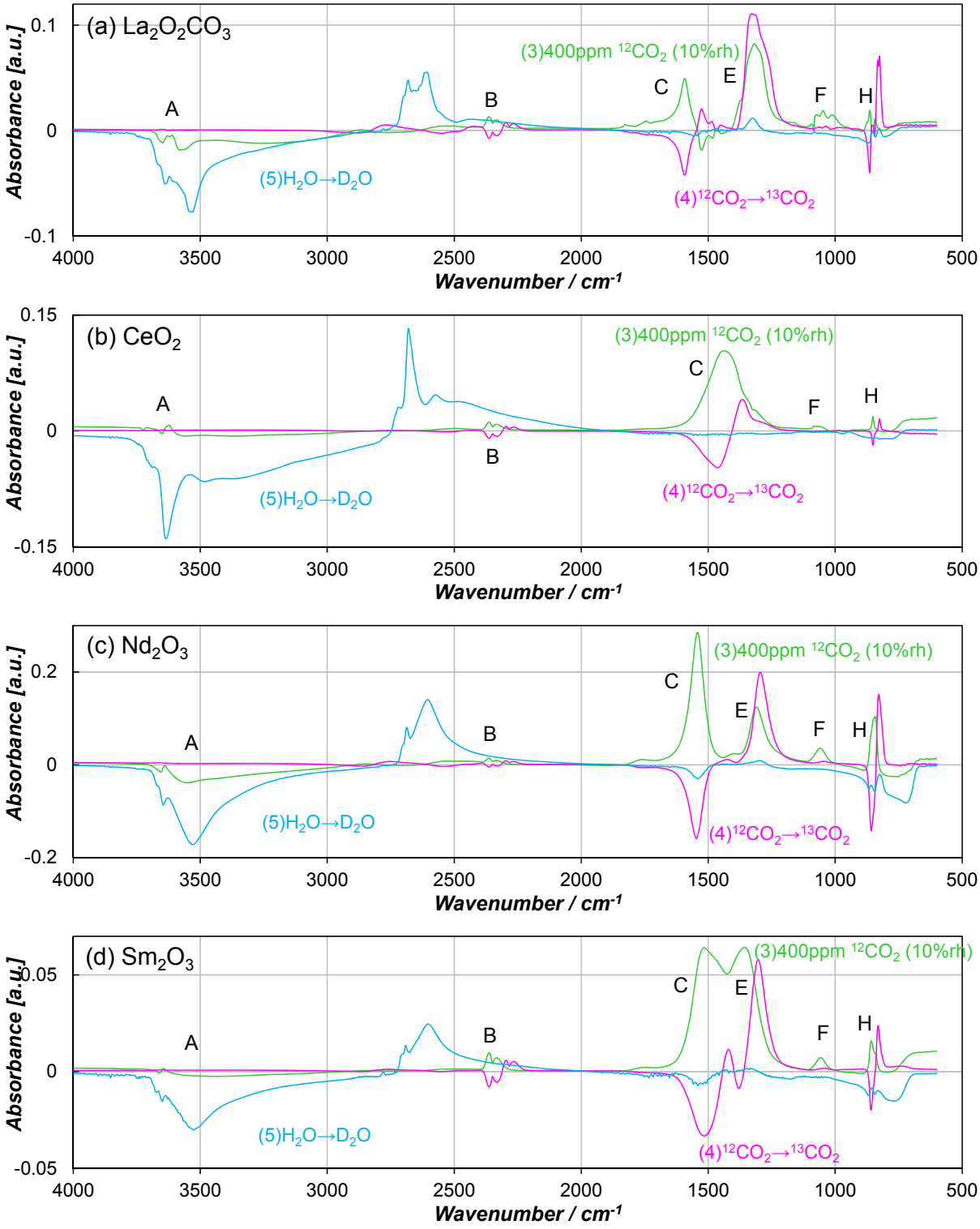

Figure 5.27.1 Difference spectra for isotopic gas exchanges of CO_2 and water. (a)-(d)

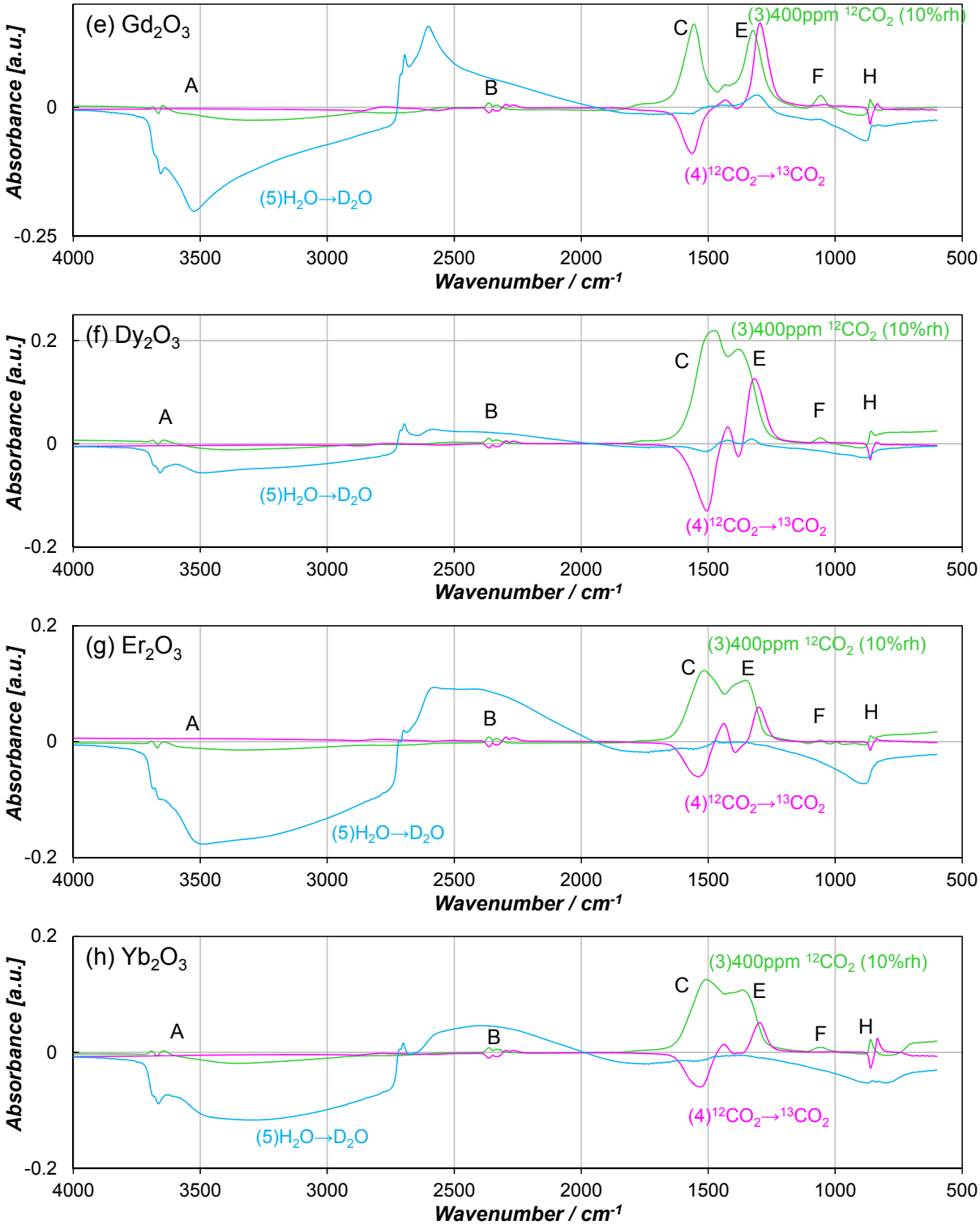

Figure 5.27.2 Difference spectra for isotopic gas exchanges of CO_2 and water. (e)-(h)

5.6 Summary and discussion on basic understanding of the sensing mechanism

For the first time a comprehensive and systematic operando characterization has been performed with the goal to understand the CO_2 the sensing mechanism of rare-earth based materials. The results from AC impedance spectroscopy, Work function, XRD, and DRIFTS obtained for the best performing material – hexagonal La oxycarbonate ($La_2O_2CO_3$) – in actual gas sensing conditions, allowed to clarify the mechanism of the electrical conduction and the CO_2 sensing. They were completed with results obtained on a selection of additional materials. In more detail:

The AC impedance spectroscopy for hexagonal $La_2O_2CO_3$ has revealed that electronic conduction was dominant in the sensor resistance and the variation of sensor resistance follows the power law owing to the band bending at grain-grain boundaries. No ionic conduction was identified and the electronic contribution from grain-electrode boundaries and grain bulk was much smaller than grain-grain boundaries.

The work function change up to approximately 0.6 eV and electron affinity change $\Delta\chi$ have been observed for hexagonal $La_2O_2CO_3$ with varying the CO_2 concentration or humidity, which indicates the existence of the dipoles from surface adsorbate species. Influence of CO_2 exposure on electron $\Delta\chi$ is much larger than that of H_2O, and CO_2 dependency of $\Delta\chi$ in dry condition was higher than that in wet condition.

The XRD for hexagonal $La_2O_2CO_3$ and Gd_2O_3 indicates that there was no change in the bulk such as the transformation and the change in lattice parameter when the sensor resistance changed with varying CO_2 concentration or humidity. These results were consistent with those from the AC impedance spectroscopy.

The DRIFTS results for hexagonal $La_2O_2CO_3$ and the rare-earth oxides (Sm_2O_3, Gd_2O_3, Dy_2O_3, Er_2O_3, and Yb_2O_3) demonstrate that the absorbance spectrum reflecting the competitive adsorption between carbonates and hydroxyl groups can be correlated with the variation of the sensor resistance, and that the formation of carbonates during CO_2 exposure was linked to the increase in resistance and the formation of hydroxyl groups was linked to the decrease in resistance. As for hexagonal $La_2O_2CO_3$, the correlation between DRIFTS and $\Delta\chi$ from the work function measurement was ascertained. Further studies are needed to identify the adsorbates in more detail and to clarify what causes the difference in sensitivity between the different materials.

Regarding the sensing mechanism, it seems reasonable to conclude that there is the competitive adsorption between carbonates and hydroxyl groups on the surface of rare-earth based CO_2 sensitive material, which changes the band bending at grain-grain boundaries of the material according to CO_2 concentration, resulting in the change in sensor resistance.

6 Summary and conclusion

6.1 Stabilizing the synthesis and sensing properties of $La_2O_2CO_3$

I have optimized the heat treatment conditions for stabilizing the synthesis and sensing properties of $La_2O_2CO_3$ by preparing and evaluating the sensors based on six types of material from the six different heat treatments. Three of them were hexagonal $La_2O_2CO_3$ from La hydroxide and La oxalate hydrate. The other three of them were monoclinic $La_2O_2CO_3$ from La oxalate hydrate.

From the results of the sensor evaluation, it has been confirmed that 300°C is suitable for the standard operating temperature and that the hexagonal structure possesses a higher sensitivity and stability than the monoclinic structure and No.6 (Starting material = La oxalate hydrate, Heat treatment conditions = 550°C for 72 hours) is the optimal conditions.

6.2 Material exploration for rare-earth based chemoresistive CO_2 sensors

I have synthesized rare-earth oxycarbonate $Ln_2O_2CO_3$ (Ln = La, Nd, and Sm) and rare-earth oxides Ln_2O_3 (Ln = Nd, Sm, Gd, Dy, Er, and Yb) and LnO_2 (Ln = Ce) by heat treatments in air from the oxalate hydrate or the acetate hydrate.

All the materials, with the exception of CeO_2 and Nd_2O_3, were sensitive to CO_2. It is remarkable that rare-earth oxides Ln_2O_3 (Ln = Sm, Gd, Dy, Er, and Yb) crystalizing in cubic structure exhibited a chemoresistive effect for CO_2. These results are new findings.

Among the CO_2 sensitive materials, only $Nd_2O_2CO_3$ was not stable. It is thought that $Nd_2O_2CO_3$ was transformed into the oxide. All others proved sufficient for practical use in terms of the stability, influence of humidity, selectivity, and the linearity of sensor signal up to 10,000 ppm. Hexagonal $La_2O_2CO_3$ is the best among them.

6.3 Basic understanding of the sensing mechanism

I have conducted comprehensive and systematic operando characterization to understand the CO_2 the sensing mechanism of rare-earth based materials for the first time. Specifically, the results from AC impedance spectroscopy, Work function, XRD, and DRIFTS have been obtained mainly for the best performing hexagonal $La_2O_2CO_3$ under actual gas sensing conditions.

The AC impedance spectroscopy for hexagonal $La_2O_2CO_3$ has revealed that electronic conduction was dominant in the sensor resistance and the variation of sensor resistance follows the power law owing to the band bending at grain-grain boundaries. No ionic conduction was identified in the experiments.

The work function measurements for hexagonal $La_2O_2CO_3$ indicate the existence of the dipoles from surface adsorbate species and that influence of CO_2 exposure on electron affinity change $\Delta\chi$ was much larger than that of H_2O, and CO_2 dependency of $\Delta\chi$ in dry condition was higher than that in wet condition.

The XRD for hexagonal $La_2O_2CO_3$ and Gd_2O_3 indicates that there was no change in the bulk such as the transformation and the change in lattice parameter when the sensor resistance changed with varying CO_2 concentration or humidity. These results were consistent with those from the AC impedance spectroscopy.

The DRIFTS for hexagonal $La_2O_2CO_3$ and the rare-earth oxides (Sm_2O_3, Gd_2O_3, Dy_2O_3, Er_2O_3, and Yb_2O_3) demonstrates that the absorbance spectrum reflecting the competitive adsorption between carbonates and hydroxyl groups was correlated with the variation of the sensor resistance.

Regarding the sensing mechanism, it seems reasonable to conclude that there is the competitive adsorption between carbonates and hydroxyl groups on the surface of rare-earth based CO_2 sensitive material, which varies the band bending at grain-grain boundaries of the material according to CO_2 concentration, resulting in the change in sensor resistance.

7 Bibliography

[1] Atmospheric CO2 at Maura Loa Observatory, (n.d.). https://www.esrl.noaa.gov/gmd/ccgg/trends/full.html.

[2] D.A. LASHOF, D.R. Ahuja, Relative contributions of greenhouse gas emissions to global warming, Nature. 344 (1990) 529–531.

[3] A.A. Lacis, G.S. A, D. Rind, R.A. Ruedy, Atmospheric CO2: Principal Control Knob Governing Earth's Temperature, Science (80-.). 330 (2010) 356–359. doi:10.1126/science.1190653.

[4] ASHRAE Standard 62-1989, 1989. https://www.osti.gov/servlets/purl/5209141.

[5] F. Caul, M. Dawkins, Indoor Air Quality an introduction by ASHRAE Ireland Section, 2016. http://www.energycork.ie/wp-content/uploads/2016/12/ASHRAE-IAQ.pdf.

[6] Z.S. Chalabi, A. Biro, B.J. Bailey, D.P. Aikman, K.E. Cockshull, Optimal Control Strategies for Carbon Dioxide Enrichment in Greenhouse Tomato Crops*Part 1: Using Pure Carbon Dioxide, Biosyst. Eng. 81 (2002) 421–431. doi:doi:10.1006/bioe.2001.0039.

[7] C. Becker, H.P. Kläring, CO2 enrichment can produce high red leaf lettuce yield while increasing most flavonoid glycoside and some caffeic acid derivative concentrations, Food Chem. 199 (2016) 736–745. doi:10.1016/j.foodchem.2015.12.059.

[8] European Comission, Science for Envionment Policy Issue 452, 2016. http://ec.europa.eu/environment/integration/research/newsalert/pdf/very_high_co2_levels_decrease_antioxidant_content_green_vegetables_452na5_en.pdf.

[9] Global Advanced CO2 Sensors Market Growth 2019-2024, LP Inf. Inc. (n.d.).

https://www.marketwatch.com/press-release/advanced-co2-sensors-market-size-to-surge-at-95-cagr-and-hit-usd-910-million-by-2024-2019-04-17-617588.

[10] T. Maekawa, Y. Kawabata, N. Yoshihiro, I. Hiroshi, T. Shinji, I. Nobuhito, A. Ginya, A Smart Carbon Dioxide Gas Sensor Based on Solid Electrolytes, Electrochemistry. 74 (2006) 118. doi:https://doi.org/10.5796/electrochemistry.74.118.

[11] L. Zhengzhou Winsen Electronics Technology Co., Low Power-Consumption CO2 Sensor (Model No.MG-812) Operating Manual, 2016.

[12] S.K. Pandey, K.-H. Kim, The Relative Performance of NDIR-based Sensors in the Near Real-time Analysis of CO2 in Air, Sensors. 7 (2007) 1683–1696. doi:10.3390/s7091683.

[13] J. Hodgkinson, R. Smith, W. On, J.R. Saffell, R.P. Tatam, Sensors and Actuators B : Chemical Non-dispersive infra-red (NDIR) measurement of carbon dioxide at 4 . 2 □ m in a compact and optically efficient sensor, Sensors Actuators B. Chem. 186 (2013) 580–588. doi:10.1016/j.snb.2013.06.006.

[14] I. Djerdj, A. Haensch, D. Koziej, S. Pokhrel, N. Barsan, U. Weimar, M. Niederberger, Neodymium dioxide carbonate as a sensing layer for chemoresistive CO 2 sensing, Chem. Mater. 21 (2009) 5375–5381. doi:10.1021/cm9013392.

[15] A. Haensch, D. Koziej, M. Niederberger, N. Barsan, U. Weimar, Rare earth oxycarbonates as a material class for chemoresistive CO 2 gas sensors, Procedia Eng. 5 (2010) 139–142. doi:10.1016/j.proeng.2010.09.067.

[16] O. Hirsch, K.O. Kvashnina, L. Luo, M.J. Süess, P. Glatzel, D. Koziej, High-energy resolution X-ray absorption and emission spectroscopy reveals insight into unique

selectivity of La-based nanoparticles for CO 2, Proc. Natl. Acad. Sci. 112 (2015) 201516192. doi:10.1073/pnas.1516192113.

[17] M. Kodu, T. Avarmaa, H. Mändar, R. Saar, R. Jaaniso, Structure-Dependent CO2 Gas Sensitivity of La2O2CO3 Thin Films, J. Sensors. 2017 (2017). doi:10.1155/2017/9591081.

[18] A. Haensch, CO 2 gas sensors based on rare earth oxycarbonates, PhD thesis, University of Tuebingen, 2016.

[19] T. Suzuki, Crystal Structure and CO 2 Sensing Properties of La oxycarbonate, Master thesis, University of Tuebingen, 2018.

[20] N. Mizuno, T. Yoshioka, K. Kato, M. Iwamoto, CO2-sensing characteristics of SnO2 element modified by La2O3, Sensors Actuators B. 13–14 (1993) 473–475.

[21] E.H.A. Diagne, M. Lumbreras, Elaboration and characterization of tin oxide-lanthanum oxide mixed layers prepared by the electrostatic spray pyrolysis technique, Sensors Actuators, B Chem. 78 (2001) 98–105. doi:10.1016/S0925-4005(01)00797-3.

[22] J.U.M. M.S. Lee, A new process for fabricating CO2 sensing layers based on BaTiO3 and additives, Sens. Actuators B. 68 (2000) 293–299.

[23] A. Marsal, G. Dezanneau, A. Cornet, J.R. Morante, A new CO2 gas sensing material, Sensors Actuators, B Chem. 95 (2003) 266–270. doi:10.1016/S0925-4005(03)00443-X.

[24] T. Suzuki, F. Lauxmann, A. Sackmann, A. Staerz, U. Weimar, C. Berthold, N. Barsan, Crystal Structure and CO2 Sensing Properties of Rare-earth oxycarbonates, in: Proc. 17th Int. Meet. Chem. Sensors 2018 Proc., Vienna, 2018: pp. 541–542. doi:10.5162/IMCS2018/P1GS.12.

[25] T. Suzuki, F. Lauxmann, A. Sackmann, A. Staerz, U. Weimar, C. Berthold, N. Barsan, Operando Investigations of Rare-Earth Oxycarbonate CO2 Sensors, in: Proc. EUROSENSORS 2018, Graz, 2018. doi:10.3390/proceedings2130801.

[26] A. Haensch, I. Djerj, M. Niederberger, N. Barsan, U. Weimar, CO2 sensing with chemoresistive Nd2O2CO3 sensors - Operando insights, Procedia Chem. 1 (2009) 650–653. doi:10.1016/j.proche.2009.07.162.

[27] A. Haensch, D. Borowski, N. Barsan, D. Koziej, M. Niederberger, U. Weimar, Faster response times of rare-earth oxycarbonate based CO2 sensors and another readout strategy for real-world applications, Procedia Eng. 25 (2011) 1429–1432. doi:10.1016/j.proeng.2011.12.353.

[28] N. Bârsan, U. Weimar, Understanding the fundamental principles of metal oxide based gas sensors ; the example of CO sensing with SnO 2 sensors in the presence of humidity, J. Phys. Condens. Matter. 15 (2003).

[29] N. Barsan, D. Koziej, U. Weimar, Metal oxide-based gas sensor research: How to?, Sensors Actuators, B Chem. 121 (2007) 18–35. doi:10.1016/j.snb.2006.09.047.

[30] N. Bârsan, U. Weimar, Understanding the fundamental principles of metal oxide based gas sensors; the example of CO sensing with SnO2sensors in the presence of humidity, J. Phys. Condens. Matter. 15 (2003). doi:10.1088/0953-8984/15/20/201.

[31] T. Sahm, A. Gurlo, N. Bârsan, U. Weimar, Basics of oxygen and SnO2interaction; work function change and conductivity measurements, Sensors Actuators, B Chem. 118 (2006) 78–83. doi:10.1016/j.snb.2006.04.004.

[32] G. Chen, B. Han, S. Deng, Y. Wang, Y. Wang, Lanthanum dioxide carbonate

La2O2CO3 nanorods as a sensing material for chemoresistive CO2 gas sensor, Electrochim. Acta. 127 (2014) 355–361. doi:10.1016/j.electacta.2014.02.075.

[33] Y.-H. Hou, W.-C. Han, W.-S. Xia, H.-L. Wan, Structure Sensitivity of La $_2$ O $_2$ CO $_3$ Catalysts in the Oxidative Coupling of Methane, ACS Catal. 5 (2015) 1663–1674. doi:10.1021/cs501733r.

[34] R.W.G. Wyckoff, Crystal Structures, New York : Interscience Publishers, 1963.

[35] H. Bommer, Die Gitterkonstanten der C-Formen der Oxyde der se ltenen Erdmetalle, Zeitschrift Für Anorg. Und Allg. Chemie. 241 (1939) 273.

[36] H. Mueller-Buschbaum, Zur Struktur der A-Form der Sesquioxide der Seltenen Erden. IIStrukturuntersuchung an Nd2 O3, Zeitschrift Für Anorg. Und Allg. Chemie. 343 (1966) 6.

[37] N. Hirosaki, S. Ogata, C. Kocer, A b initio calculation of the crystal structure of the lanthanide Ln 2 O 3 sesquioxides, 351 (2003) 31–34.

[38] A. Saiki, N. Ishizawa, N. Mizutani, M. Kato, Structural Change of C-Rare Earth Sesquioxides Yb2O3 and Er2O3 as a Fuction of Temperature, J. Ceram. Assoc. Japan. 93 (1985) 649.

[39] T. Suzuki, A. Sackmann, A. Oprea, U. Weimar, N. Barsan, RARE-EARTH BASED CHEMORESISTIVE CO2 SENSORS, in: Proc. TRANSDUCERS2019 EUROSENSORS XXXIII, Berlin, 2019. doi:10.1109/TRANSDUCERS.2019.8808245.

[40] T. Suzuki, A. Sackmann, A. Oprea, U. Weimar, N. Barsan, Rare-Earth Based Chemoresistive CO 2 Sensors and Their Operando Investigations, in: Proc. 8th Gospel Work. Gas Sensors Based Semicond. Met. Oxides Basic Underst. Appl. Fields), Ferrara, 2019. doi:10.3390/proceedings2019014017.

[41] I. Warshaw, R. Roy, B.I. Warshaw, R. Roy, POLYMORPHISM OF THE RARE EARTH SESQUIOXIDES1, 309 (1960) 2048–2051. doi:10.1021/j100828a030.

[42] H.R. Hoekstra, Phase Relationships in the Rare Earth Sesquioxides at High Pressure12, 5 (1965) 754–757. doi:10.1021/ic50039a013.

[43] G. Adachi, N. Imanaka, The Binary Rare Earth Oxides, 2665 (1998). doi:10.1021/cr940055h.

[44] G. Adachi, N. Imanaka, Z.C. Kang, Binary rare earth oxides, 2005.

[45] M.P. Rosynek, Catalytic Properties of Rare Earth Oxides Catalytic Properties of Rare Earth Oxides, 4940 (2007). doi:10.1080/03602457708079635.

[46] A.I. Shelykh, Periodicity in the band gap variation of Ln2X 3 (X = O , S , Se) in the lanthanide series, 242 (1996) 41–44.

[47] A. L. L., W. P. N, W. David, Rare Earths. IV. Dissociation Energies of the Gaseous Monoxides of the Rare Earths1, 71 (1967) 2707. doi:10.1021/j100867a049.

[48] A. Oxides, The thermodynamics of ionization of gaseous oxides ; the first ionization potentials of the lanthanide metals and monoxides, 1027 (2015).

[49] G.V.S. Rao, S. Ramdas, Electrical Transport in Rare-Earth Oxides *, 384 (1970) 377–384.

[50] D. Degler, S. Wicker, U. Weimar, N. Barsan, Identifying the Active Oxygen Species in SnO2 Based Gas Sensing Materials: An Operando IR Spectrsocopy Study, J. Phys. Chem. C. 119 (2015) 11792–11799. doi:10.1021/acs.jpcc.5b04082.

[51] D. Koziej, K. Thomas, N. Barsan, F. Thibault-Starzyk, U. Weimar, Influence of annealing temperature on the CO sensing mechanism for tin dioxide based sensors–Operando studies, Catal. Today. 126 (2007) 211–218.

doi:10.1016/j.cattod.2007.03.011.

[52] K. Grossmann, R.G. Pavelko, N. Barsan, U. Weimar, Interplay of H2 , water vapor and oxygenat the surface of SnO2 based gas sensors – An operando investigation utilizing deuterated gases, Sensors Actuators B. 166–167 (2012) 787–793. doi:10.1016/j.snb.2012.03.075.

[53] R.G. Pavelko, H. Daly, M. Hu, C. Hardacre, E. Llobet, Time-Resolved DRIFTS, MS, and Resistance Study of SnO 2 Materials: The Role of Surface Hydroxyl Groups in Formation of Donor States, J. Phys. Chem. C. 117 (2013) 4158. doi:10.1021/jp312532u.

[54] S. Wicker, Influence of humidity on the gas sensing characteristics of SnO2 - DRIFTS investigation of different base materials and dopants, PhD thesis, University of Tuebingen, 2016.

[55] A. Davydov, MOLECULAR SPECTROSCOPY OF OXIDE CATALYST, Copyright © 2003 John Wiley & Sons Ltd., 2003.

[56] H. Freund, P. Chemistry, R. Bochum, Surface chemistry of carbon dioxide, Surf. Sci. Rep. 25 (1996) 225–273. doi:10.1196/annals.1355.022.

[57] Y. Zro, E. Ko, M. Kogler, T. Bielz, B. Klo, S. Penner, In Situ FT-IR Spectroscopic Study of CO 2 and CO Adsorption on Y 2 O 3 , (2013). doi:10.1021/jp405625x.

[58] C. Li, Y. Sakata, T. Arai, K. Domen, K. Maruya, Carbon Monoxide and Carbon Dioxide Adsorption on Cerium Oxide studied by Fourier- transform Infrared Spectroscopy, 85 (1989) 929–943.

[59] C. Binet, M. Daturi, J. Lavalley, IR study of polycrystalline ceria properties in oxidised and reduced states, 50 (1999) 207–225.

[60] O. Seiferth, K. Wolter, B. Dillmann, G. Klivenyi, H. Freund, D. Scarano, A.

Zecchina, IR investigations of CO2 adsorption on chromia surfaces : Cr O (0001) / Cr (110) versus polycrystalline a -Cr O, Surf. Sci. 421 (1999) 176–190.

[61] B. Klingenberg, M.A. Vannice, Influence of Pretreatment on Lanthanum Nitrate , Carbonate , and Oxide Powders, 4756 (1996) 2755–2768. doi:10.1021/cm9602555.